Abstract

Title of Dissertation: THE HOST GALAXIES OF
ULTRA HARD X-RAY SELECTED AGN

Michael J. Koss, Doctor of Philosophy, 2011

Dissertation directed by: Professor Richard F. Mushotzky, Advisor
Department of Astronomy

One of the great mysteries surrounding active galactic nuclei (AGN) is their triggering mechanism. Since the discovery that almost all massive galaxies host nuclear supermassive black holes, it has become clear that a trigger mechanism is required to turn on and continue to fuel the central black hole. While it is established that accretion processes are responsible for the energy emitted, the source of the accreting material is still controversial. Furthermore, the energy input from phases of black hole growth is thought to be a key regulator in the formation of galaxies and the establishment of various scaling relations. Theorists often invoke galaxy mergers as the violent mechanism to drive gas into the central regions and ignite luminous quasars, but among more common moderate luminosity AGN, there has been great controversy whether secular processes or mergers dominate AGN fueling.

A survey in the ultra hard X-ray band (14–195 keV) is an important new way to answer the fundamental question of AGN fueling. This method is independent of selection effects such as dust extinction and obscuration that plague surveys at other wavelengths because of the ability of the primary continuum to easily pass through large columns of obscuring gas and dust ($<10^{24}$ cm^{-2}).

In this PhD, we have assembled the largest sample of ultra hard X-ray selected AGN with host galaxy optical data to date, with 185 nearby (z<0.05), moderate luminosity AGN from the *Swift* BAT sample. We find that these AGN show

much higher rates of both mergers and massive spirals suggesting both mergers and accretion of cold gas in late type systems are important in AGN fueling. We also find that the most common AGN survey technique, optical line diagnostics, is heavily biased against finding AGN in mergers or spirals. Finally, in agreement with the merger driven AGN link, we find that dual AGN systems may be more common than current observation suggest since some of them are only detected using high spatial resolution, hard X-ray (>2 keV) imaging.

THE HOST GALAXIES OF
ULTRA HARD X-RAY SELECTED AGN

by

Michael J. Koss

Dissertation submitted to the Faculty of the Graduate School of the
University of Maryland at College Park in partial fulfillment
of the requirements for the degree of
Doctor of Philosophy
2011

Advisory Committee:

Professor Richard F. Mushotzky, Advisor, Chair
Professor Sylvain Veilleux
Professor Chris Reynolds
Dr. Jack Tueller
Professor Greg Sullivan, Deans Representative

Preface

Other than the first chapter which serves as an introduction and largely draws on work in the literature, most of the research described in this work have been published elsewhere or presented at professional conferences. A summary of work was given in a thesis talk at the 2011 Winter American Astronomical Society Meeting in Seattle, Washington entitled *AGN Triggering: New Results From The Swift Sample Of Hard X-ray Selected AGN*.

Chapter 2 has been accepted for publication in an upcoming issue of the *Astrophysical Journal* as the *Host Galaxy Properties of the Swift BAT Ultra Hard X-ray Selected AGN*. Parts of this chapter were also published as a conference proceedings in *X-ray Astronomy 2009, Present Status, Multi-Wavelength Approach And Future Perspective 2009* in Bologna, Italy. Finally, material in this chapter was given as a poster presentation in the 2009 and 2010 Winter American Astronomical Society Meeting.

Chapter 3 was published in the June 2010 issue of *Astrophysical Journal Letters* as *Merging and Clustering of the Swift BAT AGN Sample* (Koss et al. 2010). Part of this chapter was also given as a poster presentation at the 2010 High Energy Astrophysics Division Conference in Kona, Hawaii in 2010. This work was featured as a NASA press conference as *Swift Survey Finds 'Smoking Gun' of Black Hole Activation*, an astronomy picture of the day, and received coverage online in CBS

news and Fox.

Chapter 4 was published in *Astrophysical Journal Letters* as *Chandra Discovery of a Binary Active Galactic Nucleus in Mrk 739* (Koss et al. 2011). This work was also featured as a NASA press release and featured online in U.S. News & World Report, Popular Science, and MSNBC.

In loving memory of my father, John Koss. Dad, I am sorry you didn't

get to see the end of this, but you remain always in my heart.

Acknowledgements

read the popular science article about the launch of $Swift$ in 2004 that got me excited about being at Maryland and working on the mission, I had no idea how far this road could lead! I can never thank you enough for supporting me through six years of research. I lived the life of freedom to study whatever I wanted with $Swift$ that is every researchers dream. Without your support I would never have been able to go to Japan to work on instrumentation or spend my last year with my wife working in Hawaii. Thank you for trusting me and giving me the incredible opportunity to work on $Swift$.

And to my co-adviser Sylvain. Thank you for your expert advice since the journey began with your help at the Kitt Peak summer school in 2007. I sometimes wondered if you would just stop replying to all the emails I sent you asking suggestions on this paper or that telescope proposal. But you never did. You taught me an incredible amount about being an effective, focused, and pragmatic scientist, and a clear writer. You have helped me so much that when I struggle to improve my writing I often think, "How would Sylvain say this?".

I would also like to thank my adviser, Rich. I am amazed at the depth of your knowledge and the ease with which you explain difficult concepts in an easy way. Thanks for explaining things a first, second, third, and as many times as needed. I am also appreciative that no matter when I walk into your office or give you a call you always drop everything and talk about what is exciting in my research. I am continually surprised with how much you have done to promote my work. I would have certainly never had the excitement of going to NASA headquarters or doing a press release without your help. I also appreciate your keen sense for

great research projects. One researcher aptly put it, "Rich has so many great ideas, they are like fleas, you hang around him a bit and you are bound to come up with something great." I hope I can mentor students with the same open door policy, energy, and passion that you had for all of my work.

To my family, my brothers, and in particular, my mother, a special thanks. I am so lucky to have a parent who is always supportive and excited about my research as well as someone who is a great writer. I wish I had listened as a kid when you were trying to teach to me to write effectively.

And finally, I am deeply grateful to my loving wife. You read my papers and listened to me practice my presentations. Sorry for subjecting you to that. Thanks for always listening patiently and providing me the stability to reach my dreams.

Contents

List of Tables

List of Figures

Chapter 1

Introduction

1.1 Motivation

The launch of the $Swift$ satellite a year before I entered graduate school in 2004
provided an exceptional research opportunity. The Burst Alert Telescope (BAT)
instrument on the satellite offered the chance to study nearby sources of ultra
hard X-rays over the entire sky with unprecedented sensitivity. This wavelength
is uniquely useful in the study of Active Galactic Nuclei (AGN) since the ultra hard
X-rays can easily penetrate much of the surrounding dust and gas to directly im-
age the black hole emission and overcome many of the biases in studying AGN at
other wavelengths. The goal of this PhD is to use this ultra hard X-ray survey of
AGN to understand the environmental factors that activate and continue to fuel
AGN, through an understanding of the conditions of the host galaxies in which
they are found. We begin with an introduction to AGN, their survey methods, and
the unified model, as well as the $Swift$ satellite and BAT instrument, and finally
an introduction to optical imaging and spectroscopy, the Sloan Digital Sky Survey
(SDSS), and the sample of host galaxies used in this study.

1.2 Active Galactic Nuclei

An AGN is a compact region at the center of a galaxy that emits a large amount of radiation, sometimes producing more energy than the entire rest of the host galaxy. The study of AGN began with Carl Seyfert recognizing in 1942 that a very small fraction of galaxies had bright stellar-appearing cores with many high ionization lines in their spectra. He also noticed lines in optical spectra were much broader than in normal galaxies.

Galaxies hosting an AGN, called active galaxies, have several unique features that make them different from normal galaxies. Their AGN emission region is very compact, and has not been resolved even in the nearest known AGN in the galaxy NGC 4395. Imaging studies with the Hubble Space Telescopes (HST) show that the AGN remains unresolved at spatial resolutions of $0.05''$ giving an upper limit on the size of the emitting region of only ≈ 1 pc (Filippenko et al. 1993). Active galaxies also show extra nonthermal radiation in wavelengths outside of the typical UV, optical, and infrared blackbody radiation generated from stars that dominate the emission in normal galaxies. They can be observed from radio frequencies of <100 MHz to extreme gamma rays at frequencies of 10^{22} Hz. Besides nonthermal emission, AGN often show expulsion of energy in two oppositely directed beams called jets.

Because of their tremendous energies, AGN are thought to be powered by gravitational accretion onto a central massive source, which is extremely efficient at turning rest mass into energy (Lynden-Bell 1969). Supermassive black holes with typical masses of 10^6 to 10^{10} $M_\odot$ are thought to be the central source in AGN since bright nuclear star clusters of the required mass and small size are difficult to construct and maintain. Studies of nearby galaxies have also shown that nearly

all massive galaxies with bulges harbor a supermassive black hole in their center (Magorrian et al. 1998).

As matter falls into the black hole an accretion disk on a scale of ≈ 0.01 pc is expected to form because matter traveling on different orbits typically collide and mix to form a single disk. In order for matter to fall into the black hole it must lose its angular momentum through dissipation in the accretion disk. This process gives rise to intense frictional heating and makes the accretion disk hottest near the black hole and cooler farther away. The accretion disc of a black hole is hot enough to emit soft X-rays just outside of the event horizon as well as UV and optical emission at larger radii in the accretion disk.

For most AGN, the majority of hard X-ray (>2 keV) and gamma ray emission comes from inverse Compton scattering of the photons emitted by the accretion disk. In normal Compton scattering, photons scatter off stationary electrons and lose some energy in the recoil process. In inverse Compton scattering, the energy of the photons is increased by scattering off relativistic electrons.

1.3   Initial Survey Techniques and AGN Unification

The study of AGN has historically been complicated by the many ways they are found. The most basic selection mechanism of AGN, first used by Carl Seyfert, is a bright central source with a very small point like angular size, that has broad and strong emission lines (Seyfert 1943). However, this method depends on the contrast between the host galaxy and the point like nucleus that varies with wavelength and with the brightness of the host galaxy. Early surveys to find AGN also used radio techniques (Baade & Minkowski 1954) or irregular galaxy color in imaging (Sandage

1971).

AGN have been classified as quasars or Seyfert galaxies depending on the luminosity of the AGN. AGN typically have total bolometric luminosities of 10^{42} all the way up to 10^{48} erg s^{-1}. The characteristic luminosity of a field galaxy is $\approx 10^{44}$ erg s^{-1}, so the ratio of the AGN to host galaxy light is between 1% up to 1000 times greater. The most luminous AGN are classified as quasars with bolometric luminosities typically greater than 10^{45} erg s^{-1}. In quasars, it is difficult to identify the host galaxy because of the AGN brightness and because they are more often found at high redshifts. In Seyfert AGN, such as were originally found in spiral galaxies by Carl Seyfert, the AGN luminosity does not overwhelm the host galaxy light. The presence of broad optical emission lines further separates Seyfert type 1 galaxies from Seyfert type 2 galaxies with only narrow permitted and forbidden line emission.

Optical emission line diagnostics using ground based telescopes is one of the easiest and most common modern ways to select AGN. In addition to broad emission lines discussed previously to select Seyfert 1, optical emission line diagnostics identify narrow line Seyfert 2 galaxies because the hard ionizing continuum from the AGN is different from star-formation in the host galaxy. The ionizing spectra of all but the hottest O stars cut off near the He II edge at 54.4 eV (Dopita & Sutherland 1995), whereas the AGN contains a large fraction of higher energy photons. The traditional AGN line diagnostics (Baldwin et al. 1981; Veilleux & Osterbrock 1987) and more modern ones (Kewley et al. 2006) use ratios of high to low energy ionization lines to separate AGN galaxies from star forming ones. These lines are selected to be nearby in wavelength to minimize the effects of reddening on the line ratios.

The AGN unified model attempts to explain all types of observed properties of AGN as only differences in viewing angle (Antonucci 1993). In this model (Fig-

ure 1.1), the essential parts of an AGN are a supermassive black hole (SMBH) with an accretion disk, obscuring torus, and broad and narrow-line region gas. The dusty or molecular torus is considered to be a region of 1-100 pc around the central SMBH with extremely high column densities of $>10^{25}$ cm^{-2} that absorbs much of the radiation from the central engine and reemits in the infrared. The broad line region (BLR) is composed of clumpy, high density, high column density gas within $\approx$1 pc of the SMBH with typical velocities of $\approx$3000 km/s. Such high velocities cannot be due to thermal motions of the ions, but must be from the Doppler motions in moving gas. The narrow line region gas is composed of lower density and column gas that extends to much large areas of about kpc scales in AGN. Unlike the BLR, the narrow line region gas has been resolved spatially.

In the unified model, orientation determines the type of AGN observed. When the obscuring torus is blocking the line of site, soft X-ray to optical emission from the accretion disk is absorbed as well as emission from the BLR and only a narrow line AGN is detected. Even if the line of sight is blocked by the obscuring torus, some direct ultra hard X-ray emission ($>$10 keV) may still be visible because of its high penetration ability as well as the torus re-emission in the infrared. When the obscuring torus is not in the line of site, a broad line AGN is observed. Thus, type 1 and type 2 Seyferts are thought to be the same objects, but seen from different orientations (Osterbrock 1978). Support for the unification model has come from the fact that narrow line AGN have been found to have a BLR in polarized light that is hidden by obscuration but visible in polarized light (Antonucci & Miller 1985). Finally, sources with beamed radio emission, such as blazars, are thought to be viewed along a synchrotron-emitting jet component (Blandford & Rees 1978).

While the narrow line region provides a way to observe obscured AGN, one large problem is the presence of dust in this region. Dust is thought to be destroyed in the
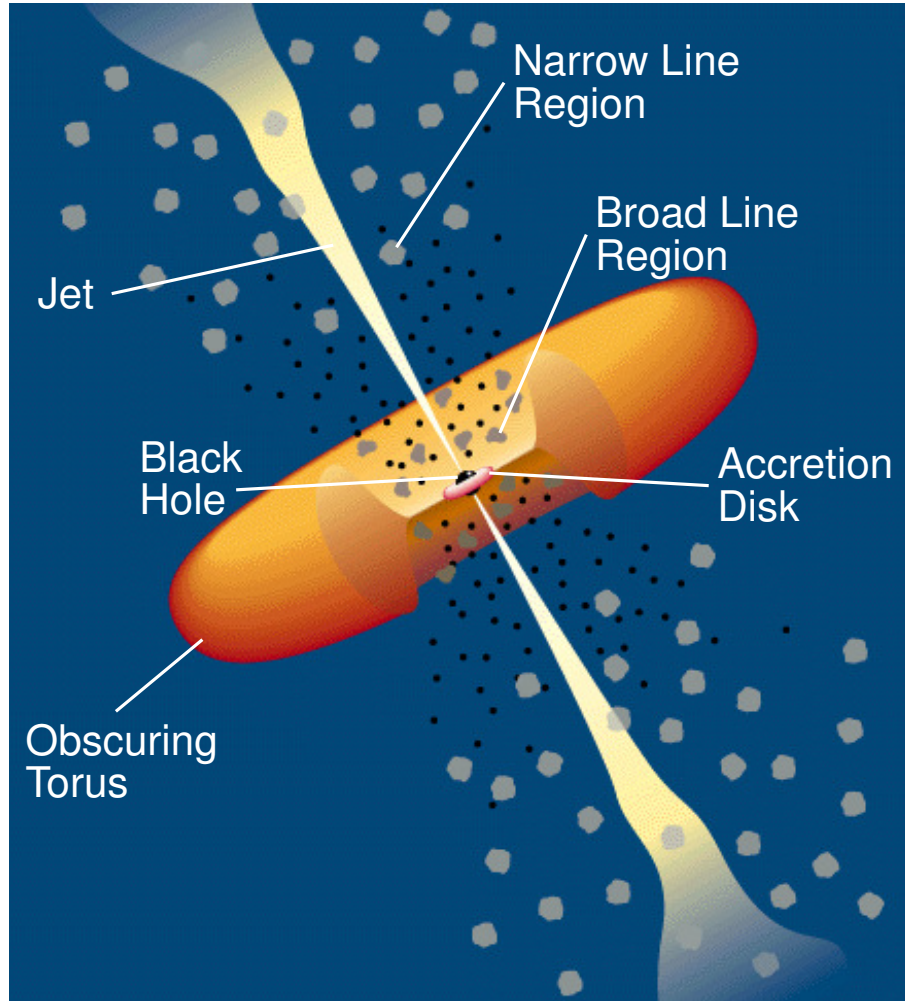
Figure 1.1: Schematic of AGN unification model from Urry & Padovani (1995).

BLR, but extend throughout the narrow line region. This dust will scatter and and absorb radiation and can substantially change the level of ionization, complicating AGN identification. An additional complication is that in some AGN, bursts of star formation can overwhelm the AGN photoionization signature in the narrow line region. This is particularly important for the next section since one of the advantages of using the ultra hard X-rays for surveying AGN is that this wavelength is not affected by dust and such energetic photons are only emitted in large amounts from AGN.

1.4 The $Swift$ Satellite and the BAT Ultra Hard X-ray Survey

The $Swift$ satellite (Gehrels et al. 2004) was launched into a low-Earth orbit on a Delta 7320 rocket November 20, 2004. $Swift$ has three co-aligned instruments, the Burst Alert Telescope (BAT) observing in the ultra hard X-rays, the X-ray Telescope (XRT), and the Ultraviolet/Optical Telescope (UVOT) (Figure 1.2). Its three instruments were designed to observe gamma ray bursts (GRBs) and afterglows in the gamma-ray, X-ray, optical, and ultraviolet wavebands. Its main mission was to detect GRBs in order to determine their origin, how they evolve with redshift, and to use them to study the early universe. Because of the very large field of view (FOV) of the BAT instrument instrument ($120° \times 90°$) the final goal, particularly important for this thesis, was to perform the most sensitive all sky survey in the ultra hard X-rays to date.

The $Swift$ BAT followed a long line of instruments developed to study the X-rays and gamma rays. The study of cosmic X-rays and gamma rays began with rocket borne X-ray counters (Giacconi et al. 1962) and gamma-rays counter on the Ranger III lunar probe (Metzger 1964). There were a variety of rocket, balloon, and space instruments during the subsequent decades, but the High Energy Astronomical Observatory (HEAO-1), launched 1977 August 12 (Marshall et al. 1980), performed the most sensitive all sky ultra hard X-ray survey (13-180 keV) before the launch of $Swift$. The HEAO-1 instruments covered the entire sky 3 times during its operating period that went until 1979 January 13.

Because of the difficulty of focusing energetic ultra hard X-rays, $Swift$ BAT uses a coded aperture mask to detect sources (Figure 1.3). In BAT, the mask contains 54,000 lead tiles that form a unique shadow pattern that can be reconstructed to
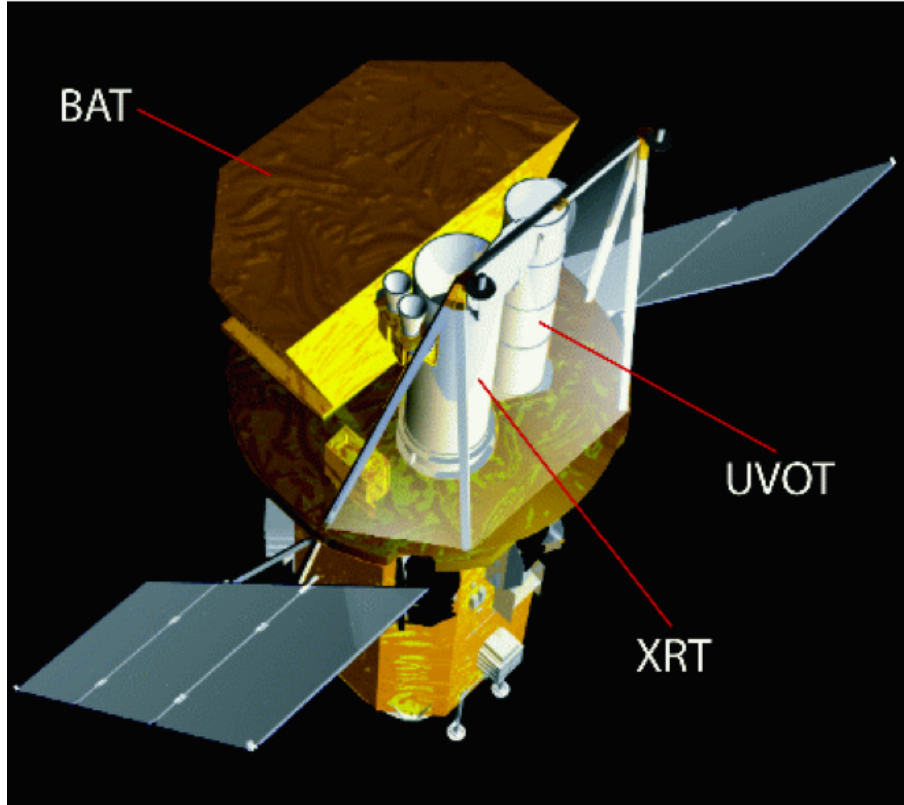
Figure 1.2: The *Swift* satellite and its three instruments.

determine the positions and fluxes in sources. Making reflecting materials in the ultra hard X-rays (>10 keV) has been impractical until only recently (see Chapter 5), since the typical atomic spacings in solids are ≈1 Å, which corresponds to an energy of ≈10 keV. Thus, traditional soft X-ray mirrors rapidly lose effective reflecting area above several keV. While BAT has a poor angular resolution of only a few arcminutes and lower sensitivity compared to instruments using focusing optics, BAT has a much larger FOV than possible using focusing optics and can image 1/10 of the entire sky.

Since GRBs are distributed throughout the sky, the BAT instrument has observed the entire sky repeatedly since the satellites launch in 2004. As of 22 months, the BAT survey had identified 461 objects of which 262 are AGN (Figure 1.4) and had an average survey exposure time for the entire sky of 4 Ms or 47 days (Tueller
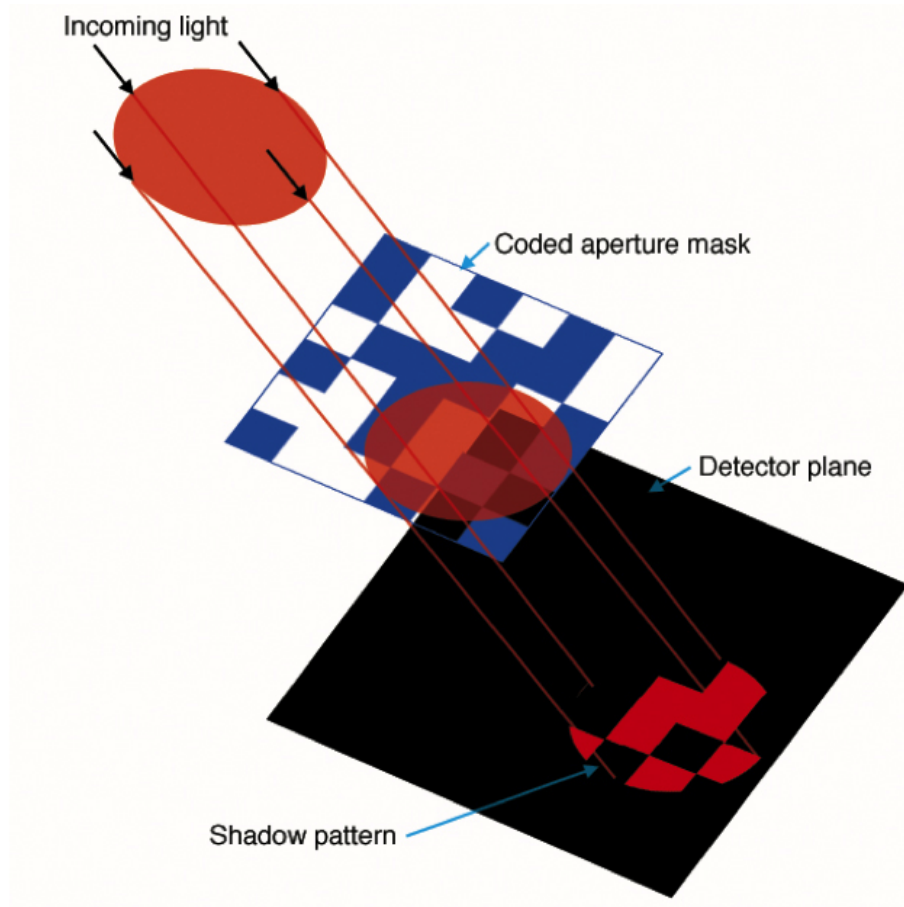
Figure 1.3: The coded aperture mask technique for detecting sources using the shadow pattern on the detector.

et al. 2010). Because of the large positional error of BAT ($\approx 2'$), higher angular resolution X-ray data for every source from Swift-XRT or archival data have been obtained allowing associations with 97% of BAT sources (Figure 1.5) . At 22 months[1], the BAT survey has a sensitivity of approximately 2.2×10^{-11} erg cm^{-2} s^{-1}. With this sensitivity, the BAT survey is about 10 times more sensitive than the previous all-sky ultra hard X-ray survey, HEAO-1 (Levine et al. 1984). In addition, the HEAO-1 survey detected only 85 sources, including only 22 AGN (Remillard et al. 1993). About 15% of BAT AGN in the 22 month catalog, or 30 of the AGN, have never before been detected as AGN at other wavelengths.

---

[1]http://heasarc.gsfc.nasa.gov/docs/swift/results/bs22mon/
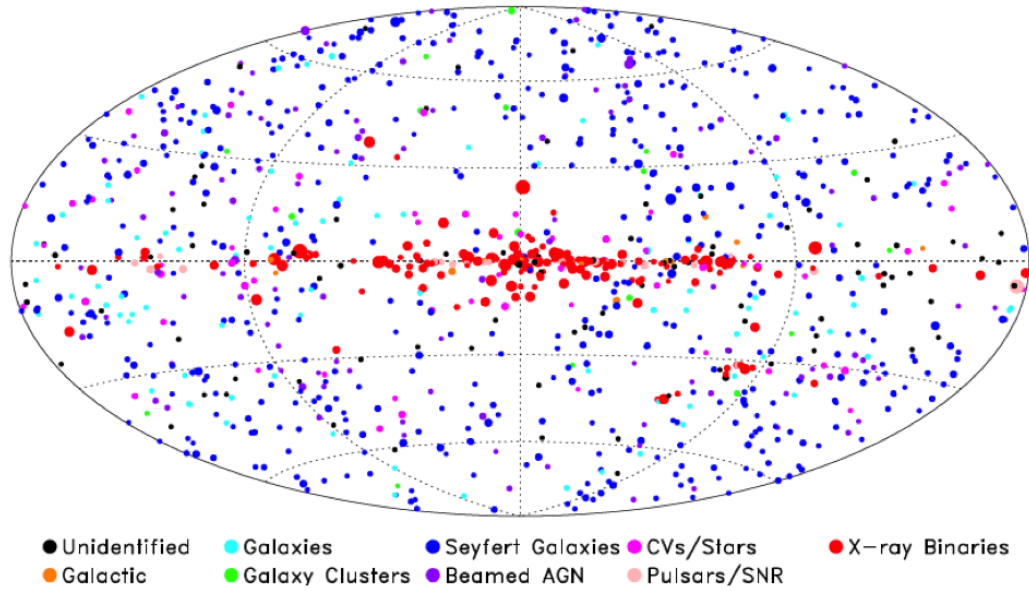
Figure 1.4: All sky map of ultra hard X-ray sources detected with $Swift$ BAT. Above the galactic plane the dominant sources are Seyfert AGN.
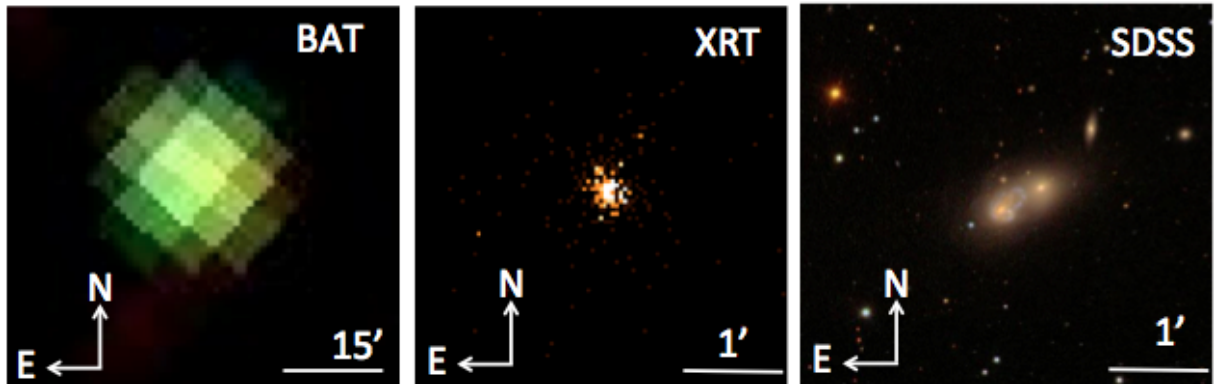
Figure 1.5: Example of XRT followup of BAT detections to determine the ultra hard X-ray source. Left: BAT flux map showing a detection of a source. Middle: XRT followup image of BAT detection in the 2-10 keV range showing a source within the galaxy NGC 1142. Right: Optical gri image from the SDSS showing the galaxy NGC 1142. Note the BAT flux image scale is 15 times larger than XRT or SDSS image.
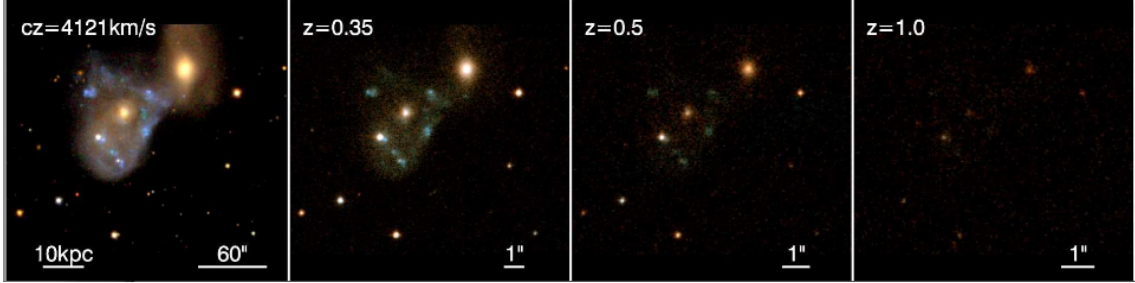
Figure 1.6: SDSS *gri*-color composite image of a galaxy merger in NGC 2445 at z=0.013 similar to the median redshift of the BAT AGN galaxies. The additional 3 panels on right show simulated images of this galaxy at higher redshifts. The simulated images were created using the FERENGI software from Barden et al. (2008) and show HST GEMS F606W–F814W images at z=0.35, z=0.5, and z=1.0 showing the severe effects of surface brightness dimming.

The BAT AGN are very nearby with a median redshift of 0.03 and provide an excellent opportunity to answer the controversial question of AGN fueling and its relationship to the host galaxy. Since it has imaged the entire sky it has a large number of these galaxies to answer these questions. Other X-ray AGN host galaxy surveys using focusing optics with *Chandra* or *XMM* at lower energies of 2-10 keV have been completed such as in the GOODS or COSMOS fields. While these surveys have much higher sensitivities than *Swift* BAT at 14-195 keV, they cover a very small area of the sky and must probe objects at moderate redshift (out to z≈1) to have a large sample size. More nearby (z<0.05) AGN offer the best opportunity to study the host in detail since high spatial resolution data are easily obtainable. In Figure 1.6, we show a simulation of the difficulty of studying the host galaxies of high redshift AGN in mergers because of the dramatic problem of surface brightness dimming. Even with the capabilities of HST, this is a major problem for higher redshift X-ray surveys studying merging galaxies or morphology (z>0.5). Additionally, studies at high redshift are forced to use rest frame UV images, where we know much less about the appearance of the normal galaxy population (Abraham 1997).

Finally, AGN emission in the ultra hard X-ray band has the unique advantage that it suffers very little from confusion from other sources. In the optical, stellar light is a major contributor, in the UV, light from young massive stars often dominates, and in the IR, dust reradiation from massive stars dominates, and finally in the radio, there is emission from HII regions, young supernovae, and other indicators of rapid star formation (Mushotzky 2004). In addition, these surveys may miss an important population of obscured narrow line AGN only visible in the ultra hard X-ray and mid-IR wavelengths (Ueda et al. 2007). While the mid-IR wavelength is less obscured, this wavelength range is problematic because of confusion with emission from star formation, sensitivity to the amount of obscuring material, and the lack of a unique way to select AGN from other luminous IR galaxies (Hickox et al. 2009; Stern et al. 2005). Therefore, the ultra hard X-ray, >15 keV range offers an important new way to select AGN for a less biased survey.

1.5 The Sloan Digital Sky Survey

Any study of the host galaxies of AGN relies heavily on an understanding of how they are different from normal galaxies. Since the emission from stars in these galaxies is predominantly emitted in the optical and NIR, one of the best way to study the host galaxies in these wavelengths. Until the advent of massive sky surveys, studies of host galaxies using morphology and color were limited to smaller samples of bright nearby galaxies in a few filters. In the past decade the Sloan Digital Sky Survey (SDSS), provided high resolution imaging and spectroscopy, and was used for the study of the host galaxies of hard X-ray selected AGN and how they are different from normal galaxies.

The SDSS survey (Abazajian et al. 2003) operated between 2000-2008, and was

a critical resource in studying the host galaxies of AGN for this PhD. The survey mapped over 35% of the sky, with photometric observations of ≈500 million objects and spectra for over 1 million objects. The survey used a 2.5-m wide-angle optical telescope at Apache Point Observatory in New Mexico. The survey used five filters (u, g, r, i, and z) covering 3000–10000 Å, roughly the limited UV available from the ground, all of the optical, and a limited part of the NIR. The SDSS telescope used the drift scanning technique for imaging which keeps the telescope fixed to avoid tracking errors and an array of thirty CCDs covering 1.5 square degrees of sky at a time. The SDSS SkyServer enabled easy public access to both spectra and images, as well as large catalogs of photometry and morphology, with the final release in January 2011.

The massive SDSS survey was also capable of recording 640 optical spectra at once and provided a large database of optical spectroscopy for over 100,000 galaxies. This database provided a sample of well matched inactive galaxies to use as a control sample for comparison to the host galaxies of BAT AGN. Additionally, a sample of ≈600 emission line selected Seyferts in the same redshift range as the BAT sample was used to provide a better understanding of how ultra hard X-ray AGN are different from AGN selected using emission line diagnostics.

In the study of BAT AGN detailed in this PhD, we used a combination of SDSS data and our own data from the Kitt Peak 2.1m telescope to study the properties of ultra hard X-ray selected AGN. We used publicly available SDSS imaging complemented with 17 nights of optical imaging data from the Kitt Peak to cover a large sample of ≈185 BAT AGN in Northern declinations (>-25°). The Kitt Peak sample was obtained in February 2008 and November 2008 using the t1ka, t2ka, and t2kb CCDs. At Kitt Peak, we used the same filters (u, g, r, i, and z) as the SDSS. Each galaxy was imaged so that a high level of signal-to-noise ratio could be achieved,

Figure 1.7: Random sample of 18 *gri* composite images of galaxies in the BAT AGN sample taken at Kitt Peak. An arcsinh stretch was used with flux scaled by magnitudes (Lupton et al. 2004).

similar to the SDSS, to capture faint features and low surface brightness emission with 12 minute exposures in *u* and 6 minute exposures in *griz*. The *u* images were obtained at twice the imaging time because of the higher sky brightness and lower signal-to-noise ratio in this band. Limiting magnitudes and observing conditions can be found in Table 1.1. A random sample of *gri* tricolor images that have been flux calibrated using the procedure of Lupton et al. (2004) can be found in Fig. 1.7. This large sample size was critical to finding statistically significant differences between the BAT AGN host galaxies and normal galaxies or AGN selected at other wavelengths.

Table 1.1.   Observing Summary–SDSS and Kitt Peak

	u	g	r	i	z
SDSS $[mag]^1$	22.3	23.3	22.9	22.3	20.7
Kitt Peak $[mag]$	24.2	24.8	24.4	23.7	22.0
SDSS $('')^2$	1.36±0.22	1.30±0.19	1.17±0.17	1.14±0.18	1.15±0.18
Kitt Peak $('')$	1.67±0.76	1.56±0.47	1.46±0.41	1.44±0.59	1.42±0.48

[1]Detection based on overlapping fields in SDSS and Kitt Peak sample with at least 5 pixels above signal-to-noise ratio>3.

[2]PSF function was calculated using the FWHM of a single gaussian fit to the 10 brightest unsaturated stars.

1.6   Thesis Outline

This thesis is comprised of six chapters focusing on understanding the host galaxies of ultra hard X-ray selected AGN with a final chapter on development of focusing optics for this wavelength. Using the relatively unbiased nature of this selection mechanism along with the largest sample of ultra hard X-ray selected AGN with host galaxy optical data to date we have found important host galaxy characteristics that are linked to the AGN fueling.

The thesis is structured in the following way. Chapter 2 focuses on the link between the AGN and the host galaxy. We examine the colors of host galaxies and address whether the AGN quenches star formation or is linked to star formation. We also discuss whether certain galaxy morphologies are linked to AGN. In addition, we investigate how galaxy stellar mass is linked to ultra hard X-ray emission. Finally, we test the unified model of Seyferts using ultra hard X-ray selected AGN and investigate how BAT AGN are different from AGN selected using optical emission line diagnostics. Chapter 3 and 4 study the AGN merger connection of the BAT sample and also provide a case study of a single BAT AGN galaxy that hosts a rare

dual AGN only detected in the hard X-rays. Chapter 5 is a discussion of continuing instrumentation development in the ultra hard X-rays and work on the InFOCμS balloon project. Finally, Chapter 6 provides a summary of the results of this PhD as well as a discussion of exciting future projects using the $Swift$ BAT ultra hard X-ray selected AGN.

Chapter 2

Host Galaxy Properties

2.1 Introduction

We begin with a study of the host galaxies properties of ultra hard X-ray selected AGN. The goal is an understanding of what environmental factors trigger the AGN to begin emitting so much energy and what continues to fuel this process. While most galaxies with bulges harbor a supermassive black hole in their center (Magorrian et al. 1998), only a small fraction exhibit the powerful radiative or kinetic output associated with AGN. While it is well established that matter falling onto the supermassive black hole is emitted as energy, the source of this material remains highly controversial. To understand what activates and continues to fuel AGN, we must better characterize the conditions of the host galaxies in which they are found.

Numerical simulations suggest that quasars ($L_{bol}>10^{45}$ erg s^{-1}) are the end product of mergers between gas-rich disk galaxies, and that supermassive black hole accretion heats the interstellar material and quenches star formation leading to passive elliptical galaxies (di Matteo et al. 2005). Alternatively, other simulations suggest sources other than mergers may fuel lower luminosity AGN, such as gas streaming down galactic bars or steady cold gas streams (Dekel et al. 2009; Hopkins &

Hernquist 2006; Mulchaey & Regan 1997).

A number of observational studies have provided interesting yet contradictory results about the relationship between the host galaxy and the AGN. A study of the host galaxies of X-ray selected AGN from the Extended Chandra Deep Field-South found that AGN are in the most luminous galaxies, with intermediate optical colors, and bulge dominated morphologies (Silverman et al. 2008). Another study of narrow emission line (NL) AGN in the Sloan Digital Sky Survey (SDSS) found the hosts were predominantly massive early-type galaxies and the most luminous AGN galaxies had significant star formation (Kauffmann et al. 2003a). An additional survey of the SDSS NL AGN host galaxies found, compared to a sample of nearby inactive galaxies, most AGN occur along the red sequence (Westoby et al. 2007). Even though these studies draw their conclusions from large optical surveys or soft X-ray surveys, their results may be biased by missing an important population of obscured AGN.

The BAT AGN sample have already provided several interesting results about their host galaxies. A study of the morphologies based on NED classifications and DSS imaging found a majority to be in spirals or peculiars (Winter et al. 2009). Other studies found that BAT AGN have been shown to have additional reddening of the narrow line region not accounted for in optical studies and be misclassified as star forming or composite regions (Meléndez et al. 2008; Winter et al. 2010). In the case of host galaxy colors, two studies using <20 BAT AGN reached different conclusions: Schawinski et al. (2009b) found that the AGN tend to be in intermediate or red galaxies and possibly suppress star formation, while Vasudevan et al. (2009) found BAT AGN in blue, starforming galaxies. This contradiction highlights a major problem in current AGN host galaxy studies: the paucity of large, uniform samples with high quality data. To make progress on this issue, we have assembled the

largest sample of ultra hard X-ray selected AGN with host galaxy optical data to date, with 185 AGN in total. The BAT AGN and comparison samples are discussed in §2.2; data reduction and analysis in §2.3 with additional discussion of removal of AGN light, the comparison sample, and selection effects in Appendix §A; the results in §2.4; and the summary and discussion in §2.5.

2.2 Samples

2.2.1 BAT AGN Sample

We selected our sample to focus on Seyfert AGN in the BAT sample which contribute the large majority, 87% of the total sample, and 99% of the nearby, z<0.05 sample. We use the classifications of Tueller et al. (2010) to exclude beamed sources such as blazars. We also restrict the sample to nearby AGN (z<0.05) which includes 80% of the BAT sample. These AGN can be further classified on the basis of broad or narrow emission lines. We define NL AGN as having Hα<2000 km/sec using spectroscopic data from Winter et al. (2010), Ho et al. (1997b), and the SDSS. For those BAT galaxies without spectra, we use available data from NED to separate NL and broad-line objects. The BAT sample has 50% (93/185) NL and 50% (92/185) broad-line sources. In addition to including the entire range from unobscured to highly obscured, the AGN have moderate luminosities, and therefore accretion rates, typical of the local universe (log L$_{2-10\,\mathrm{keV}}\approx$43, Sazonov & Revnivtsev 2004).

By imposing an upper redshift limit (z<0.05) to the sample, we focus on galaxies that are close enough to have good spatial resolution (700 pc) from ground-based optical imaging. We further restrict our survey to Northern declinations (>-25°). We also exclude six nearby galaxies with bright foreground Galactic stars where photometry is difficult and three nearby bright galaxies with saturated pixels. This

survey covers 125 nearby AGN or 50% of the entire BAT AGN sample from the 22 month survey. We also included an additional 60 AGN galaxies detected in the 58 month BAT sample catalog (Baumgartner et al. 2010, submitted) with X-ray followup with the $Swift$ XRT telescope that showed a coincident source to the 14–195 keV BAT source in the 2–10 keV band.

The optical imaging data for these galaxies include 17 nights at the Kitt Peak 2.1m telescope in the $ugriz$ SDSS bands (Table A.1) and data from the SDSS (Table A.2). The final Kitt Peak and SDSS sample includes a total of 185 galaxies, 79 BAT AGN host galaxies observed at Kitt Peak, 92 from the SDSS, and 14 galaxies observed by both the SDSS and at Kitt Peak.

2.2.2   Comparison Samples

To better understand the host galaxy properties of BAT AGN, we used a comparison sample of inactive galaxies and a sample of emission line selected AGN from the SDSS. We will henceforth refer to the three samples as the $BAT\ AGN,\ inactive\ galaxies$, and $SDSS\ AGN$, respectively.

The inactive galaxies were selected from the SDSS to have high quality photometry and similar redshifts as the BAT AGN. We selected all non-QSO galaxies from the SDSS DR7 with spectra and imaging data with redshift confidence, z_{conf}>0.9 and a redshift interval similar to the BAT AGN (0.01<z<0.07). We chose this slightly higher redshift interval because many of the SDSS galaxies with z<0.01 are too bright to be targeted in spectroscopy. We also removed NL Seyfert or LINER AGN from this sample using emission line diagnostics (Kewley et al. 2006) and the Garching catalog of reduced spectra of narrow line AGN (Kauffmann et al. 2003a). Galaxies totaled 68,275. We will refer to this sample as the $inactive\ galaxy\ sample$.

Finally, we used a sample of emission line selected AGN in the SDSS for com-

parison, which we refer to as the *SDSS AGN*. Winter et al. (2010) found that the majority (75%) of a sample of 64 BAT AGNs were Seyferts. Only 3/64 (<5%) of BAT AGN were classified as LINERS, so we excluded this type of AGN from the comparison sample. We chose narrow-line AGN since the nucleus is invisible in the optical band and thus does not have to be modeled to determine the host galaxy properties. We therefore chose a sample of all type 2 Seyferts in the SDSS DR7 with 0.01<z<0.07. We used 1282 Seyferts in this redshift range.

To ensure that the BAT AGN were not more intrinsically luminous than the SDSS AGN sample of Seyferts, we compared the [O III] of the BAT AGN with available spectra to the SDSS AGN (Figure 2.1). When measuring [O III], we used the narrow Balmer line ratio ($H\alpha/H\beta$) to correct for extinction assuming an intrinsic ratio of 3.1 and the Cardelli et al. (1989) reddening curve. For reference we also included LINERS in the SDSS. For the BAT AGN we used spectroscopic data from Winter et al. (2010), Ho et al. (1997b), and the Garching Catalog of SDSS spectra Kauffmann et al. (2003a). We find that the BAT AGN have similar [O III] luminosities as the SDSS NL Seyferts, suggesting that they also have similar intrinsic luminosities (although there may still be differences, see §2.5). We find a similar relation when only including sources with SDSS spectroscopy and excluding spectroscopic data from Winter et al. (2010) and Ho et al. (1997b).

2.3   Data Calibration, Reduction, and Analysis

Throughout this work, we adopt the following cosmological parameters to determine distances: $\Omega_m = 0.27$, $\Omega_\Lambda = 0.73$, and $H_0 = 71$ km s^{-1} Mpc^{-1}. For galaxies with z<0.01, we use the mean value of redshift independent distant measurements from NASA Extragalactic Database (NED) when available. Unless otherwise noted, error
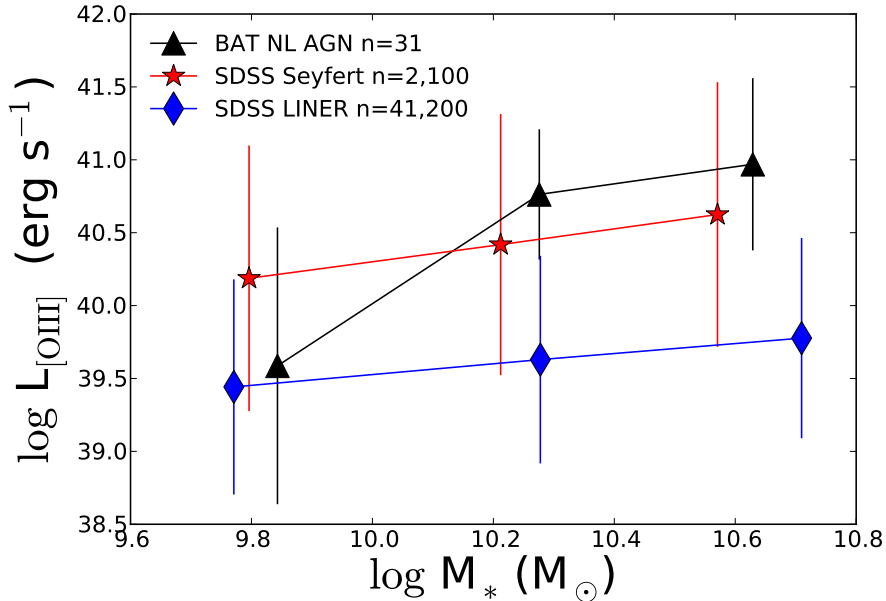
Figure 2.1: Average [O III] luminosities for the NL AGN in the BAT sample compared to the SDSS sample of narrow-line Seyferts and LINERS. The error bars indicate standard deviations in each bin. We find that the distributions of [O III] from the NL BAT AGN and NL SDSS Seyferts used in this study are from the same parent population (P(K-S)=82%). The [O III] luminosity is a measure of AGN power and suggests the NL BAT AGN have similar AGN power as SDSS NL Seyferts.

bars correspond to 1σ standard deviation of the sample.

2.3.1   Initial Calibration

The initial imaging analysis involved calibration of zero point magnitudes, coadding SDSS plates for larger galaxies, and removing extraneous sources (e.g. foreground stars, other galaxies). For calibration of the Kitt Peak data, we used the primary standard star network of 158 stars used by the SDSS for calibration (Smith et al. 2002). A calibration star was imaged before and after each galaxy at similar airmass. Extinction coefficients were determined using standard stars on a nightly basis. Standard IRAF routines were used to remove bias, dark current, and CCD non-
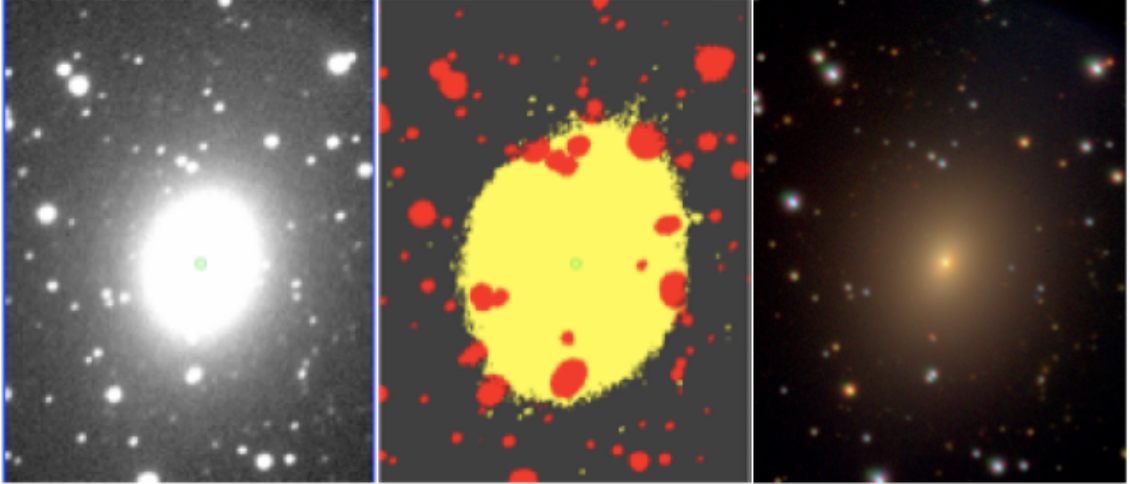
Figure 2.2: Example of the removal of foreground stars to perform photometry on the galaxy using SExtractor. On left, r band image of NGC 2110 in linear scale. In the middle, detection of objects above 1.5σ; the galaxy is shown in yellow and foreground stars are shown in red. On the right, gri composite image to check source separation in arcsinh stretch scale. Foreground stars in front of the galaxy are replaced using the IRAF FIXPIX routine. Stars outside of the galaxy are replaced with average sky values.

linearity. Galactic extinction corrections were made based on data from *IRAS* and *COBE/DIRBE* (Schlegel et al. 1998). For 8 SDSS galaxies extending across multiple SDSS plates, the MONTAGE software was used to reproject the images, rectify background and coadd plates. WCSTools was used to register Kitt Peak images from USNO stars (Mink 1996). Nearby foreground stars and galaxies were identified using segmentation maps produced by SExtractor (Figure 2.2, Bertin & Arnouts 1996). The segmentation map identified object pixels using a threshold of 3σ and a minimum of 5 pixels in $griz$. In the u band, the detection threshold was set to 1σ to ensure that faint star forming regions were detected. The segmentation map was visually compared to three color gri images to ensure proper star and galaxy separation. Stellar or foreground galaxy objects were masked with the IRAF FIXPIX routine.

2.3.2 Host Galaxy Photometry

The residual host galaxy colors were measured after removing the AGN light contribution using GALFIT. To ensure that the AGN emission was properly removed we performed simulations of AGN galaxies to test GALFIT and also checked the subtraction for BAT AGN (see Appendix §A for a discussion). A modified form of the Petrosian system, the same as is used in the SDSS automated pipeline, was used for photometry (Blanton et al. 2001) for both the SDSS and Kitt Peak observed BAT AGN galaxies. The Petrosian aperture is determined to be large enough to enclose almost all of the flux for typical galaxy profiles, but small enough that the sky noise is not significant. For consistency, the Petrosian aperture is determined from the r band and applied to the other bands. A galaxy with a bright stellar nucleus, such as a broad-line Seyfert galaxy, can have a Petrosian radius set by the nucleus alone; in this case, the Petrosian flux misses most of the extended light. Therefore the Petrosian radius in the r band was determined after the AGN model from GALFIT was subtracted. We then used the software KCORRECT (Blanton & Roweis 2007) with the *ugriz* photometry to calculate the stellar masses. This code uses the stellar population models of Bruzual & Charlot (2003) and photoionization models of Kewley et al. (2001). We used the same software to calculate the stellar mass for the inactive galaxy and SDSS AGN control samples.

We also made a comparison of the overlapping galaxy data from the SDSS and Kitt Peak to ensure there were no systematic differences in photometry. In some cases, the automated SDSS pipeline's photometry shreds bright galaxies into many smaller galaxies which leads to incorrect photometry estimates for bright, nearby galaxies (see Appendix §A). For cases where shredding wasn't a problem, the colors of overlapping galaxies observed at Kitt Peak and in the SDSS showed good agree-

ment in *griz* with mean color differences less than 0.02 mag and sample standard deviation less than 0.05 mag. The u band is more uncertain with mean $(u - g)=$ 0.05±0.16 mag brighter for the Kitt Peak measurements. This difference is expected because the u band measurements in the SDSS have a lower signal-to-noise ratio and also suffer from a red leak[1].

There were also ten nearby galaxies or 5% of the sample with pixel saturation in the SDSS images because of a bright nucleus. For these galaxies we masked the saturated pixels and fit the remaining image with a point source (PS) and floating Sérsic Index. We then used the model fit to recover the saturated pixels. We restricted using this method to those galaxies with saturation in a single imaging band with <25 pixels saturated. This excluded three very nearby galaxies (z<0.005; NGC 1068, NGC 4151, NGC 3998) with saturated pixels in multiple filters from the study. For five images of nearby galaxies taken at Kitt Peak, the estimated Petrosian radius extended beyond the edge of the CCD. In these cases we used the maximum part of the image available to determine the photometry. In addition, 16 galaxies or 9% had very low signal-to-noise ratio measurements in the u band and were not included in the photometry.

We have also provided a detailed discussion of the selection effects in the X-ray selected BAT sample of AGN, and the optically selected SDSS AGN and inactive galaxies (see Appendix §A). These selection effects are also included to enable comparison with AGN surveys at other wavelengths and for comparison with high-z studies.

---

[1]http://www.sdss.org/dr7/algorithms/fluxcal.html
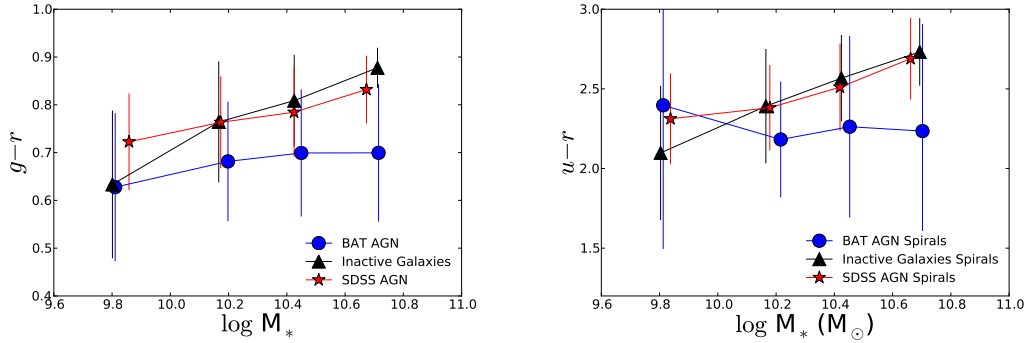
Figure 2.3: Plot of average Petrosian $g - r$ and $u - r$ for BAT AGN, inactive galaxies, and SDSS AGN. We find that the BAT AGN have bluer average colors than inactive galaxies or SDSS AGN in all but the lowest stellar mass bin. The error bars indicate standard deviations in each bin.

2.4   Results

2.4.1   Colors, Internal Extinction, and FIR emission

Since host galaxy color traces star formation, a comparison of BAT AGN host galaxy colors to a sample of inactive galaxies should show whether the AGN is linked to enhanced or suppressed star formation. A full listing of the photometry measurements of the different samples can be found in Table A.4. A plot of $g - r$ and $u - r$ for BAT AGN, inactive galaxies, and optical AGN can be found in Figure 2.3. We find that the BAT AGN are bluer in both $g - r$ and $u - r$ than the sample of inactive galaxies and SDSS AGN in all but the lowest stellar mass bin (Table A.5). A Kolmogorov-Smirnov (K-S) test indicates a <1% probability that the distribution of host galaxy colors for the BAT AGN are from the same parent distribution as the inactive galaxies or SDSS AGN.

Host galaxy colors can be reddened in galaxies with high inclinations and large amounts of dust, so we measure whether these corrections change our result that the BAT AGN tend to be bluer than inactive galaxies or SDSS AGN. Because of the

relative uncertainty in these measurements, we do not apply individual reddening corrections on any plots, but estimate how reddening corrections effect the average colors of the samples. In Figure 2.4, we show tricolor images of the 6 reddest and bluest BAT AGN host galaxies in $g - r$. The predominance of face-on spirals in the bluest sample and edge-on spirals in the reddest sample indicates the need for reddening correction based on inclination. Masters et al. (2010) studied internal extinction of galaxies identified as spirals in Galaxy Zoo and provided corrections based on the measured inclination from the SDSS photometry. For the three samples, we find that the average extinction for spiral galaxies is similar (0.04±0.03 in $g - r$), but because of the higher number of spirals in the BAT AGN sample compared to SDSS AGN or SDSS inactive galaxies (see next section), there is a larger extinction correction for the BAT AGN sample (Figure 2.5).

There are galaxies that have high levels of star formation, but are reddened in the optical wavelengths because of the presence of dust. For example, in the BAT AGN sample, the reddest galaxy in $g - r$ is NGC 6240, a luminous infrared galaxy (LIRG) in a major merger, which shows a large amount of star formation in the far-IR. This indicates that dust can play a significant role in reddening the optical light and hiding increased levels of star formation. Therefore, we estimate the total dust extinction (A_V) for each galaxy by fitting the host $ugriz$ SEDs using FAST (Kriek et al. 2009) with single-burst stellar population models. We use stellar templates from Bruzual & Charlot (2003) with the Chabrier (2003) initial mass function and solar metallicity. We fit a Calzetti et al. (2000) dust extinction reddening law (A_V= 0–3). We assume that R_V=3.1, and therefore E(B-V)=A_V/3.1. We find that the reddening determined using fits to the optical SED of BAT AGN (0.34±0.26 in $g - r$) are on average larger than for comparable inactive galaxies (0.20±0.14) or SDSS AGN (0.21±0.13). Therefore, we do not find evidence that the bluer measured
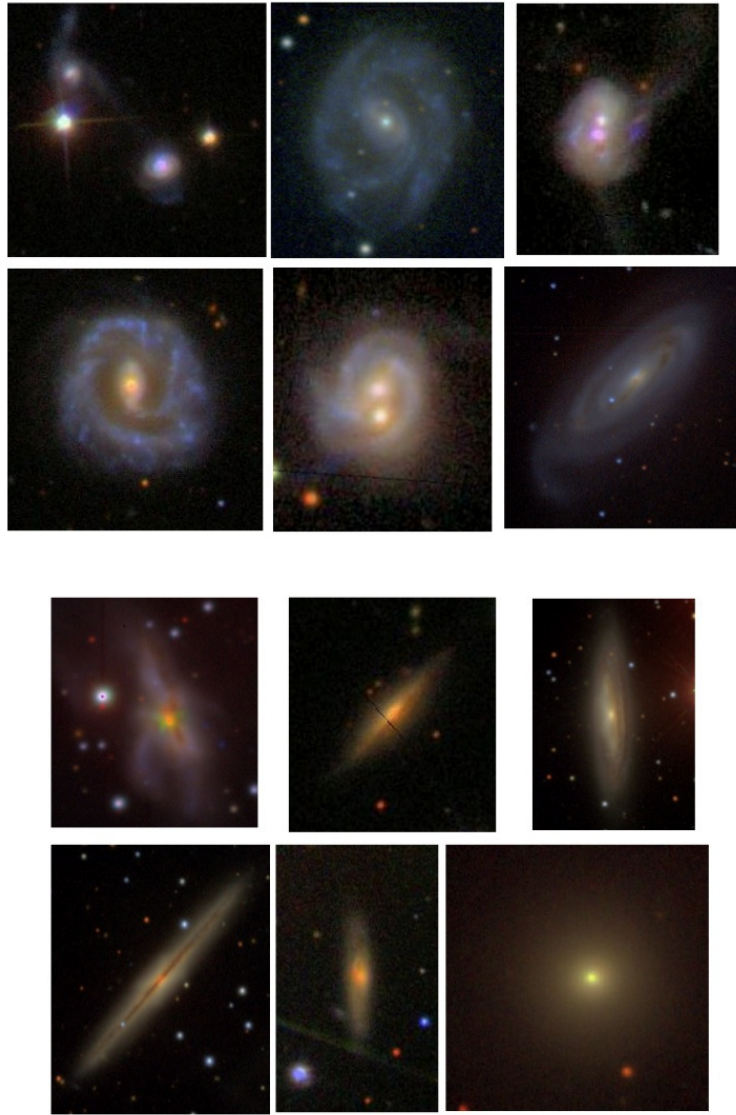
Figure 2.4: *Upper*: Tricolor images of six bluest BAT AGN host galaxies in $g - r$. We find that these BAT AGN are predominantly in mergers and face on spirals. *Lower*: Tricolor images of six reddest BAT AGN host galaxies in $g - r$. We find that 4/6 of these BAT AGN are in edge-on spirals that are reddened by internal extinction. The predominance of face on spirals in the bluest galaxies and edge-on spirals in the reddest galaxies indicate the need for a reddening correction based on inclination.
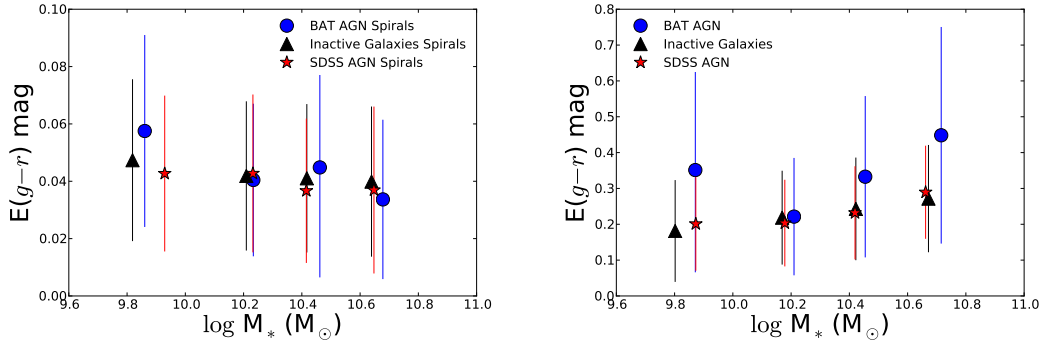
Figure 2.5: *Left*: A plot of the average inclination color correction for BAT AGN, inactive galaxies, and SDSS AGN in spirals based on the corrections in Masters et al. (2010). The average extinction for spiral galaxies is similar between the three samples. However, because of the higher number of spirals in the BAT AGN sample (see Figure 2.8), there is a larger extinction correction for the BAT AGN sample. *Right*: Plot of average dust reddening based on fitting the AGN host $ugriz$ SEDs using FAST (Kriek et al. 2009) with single-burst stellar population models. We use stellar templates from Bruzual & Charlot (2003) with the Chabrier (2003) initial mass function and solar metallicity. We fit a Calzetti et al. (2000) dust extinction reddening law ($A_V = 0$–3). We assume that R_V=3.1, and therefore E(B-V)=A_V/3.1. The extinction in the $g-r$ band is very similar (E(B-V)=1.06*E($g-r$)). The extinction in the u-r band is E($u-r$)=2.30*E($g-r$).

colors of BAT AGN, compared with those of inactive galaxies and SDSS AGN, can be explained as smaller dust reddening. In fact, reddening corrections make the BAT AGN even bluer than comparable SDSS AGN or inactive galaxies. We also find that the reddening corrections for host galaxy inclination are on average much smaller than dust reddening (0.04±0.03 vs. 0.34±0.26 in $g-r$).

The far-IR provides an additional tracer of star formation that is less sensitive to reddening than shorter wavelengths. The 90 μm emission is a useful tracer of strong bursts of recent star formation and is less affected by AGN emission (Mullaney et al. 2011; Netzer et al. 2007). We first looked at the rate of detection in $AKARI$ in each of the samples in the same redshift range (0.01<z<0.05). In this redshift range, 54±5% (86/185) of BAT AGN are detected by $AKARI$ at 90 μm, compared to only 4±1% of SDSS AGN, and 5±1% of inactive galaxies. The error bars represent 1σ

Poisson statistics.

To ensure this difference was not an effect of the differences in the distribution of stellar mass and redshift of the samples, we matched each BAT AGN to one inactive galaxy and one SDSS AGN based on redshift and stellar mass. We find a similar percentage for both inactive galaxies $7\pm3\%$ (11/158) and SDSS AGN $3\pm2\%$ (5/158) detected by *AKARI*. The error bars represent 1σ Poisson statistics.

While there is a possibility of AGN contamination in the 90 μm emission, the similar levels of *AKARI* detections for the inactive galaxies and SDSS AGN indicate that this level of contamination is limited. In addition, the AGN contamination to the FIR should be similar for BAT and SDSS AGN since the [O III] luminosities are similar and [O III] is an indicator of bolometric luminosity. All of these results indicate that the BAT AGN are more luminous at 90 μm, which suggests enhanced star formation among BAT AGN when compared to SDSS AGN and inactive galaxies.

2.4.2 Host Galaxy Morphology

We investigated galaxy morphology to find which environments are most conducive to hosting an AGN and how ultra hard X-ray selected AGN are different than the SDSS AGN or inactive galaxies. A full listing of the morphological measurements can be found in Table A.6. While we have limited our results to NL AGN because of the difficulty of subtracting the light distribution to make morphological measurements (Pierce et al. 2010), we provide morphological measurements of broad-line AGN after AGN light subtraction with GALFIT in this table as well.

The first measure we compared was concentration. To enable comparison with the SDSS, the concentration index is defined as the ratio of the radii containing 90 and 50 per cent of the Petrosian r-band galaxy light $C = R_{90}/R_{50}$. A galaxy with a steep concentration profile, such as an elliptical, will show a relatively large
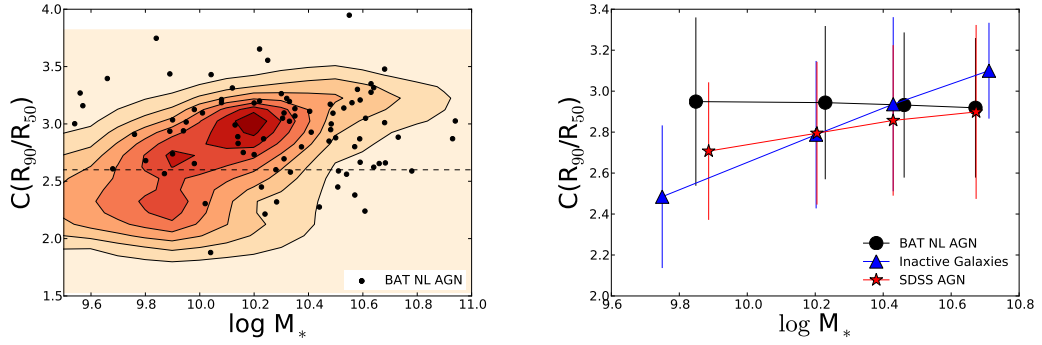
Figure 2.6: *Left*: Plot of concentration vs. stellar mass with contours showing inactive galaxies and points for the BAT AGN. The contour levels are plotted on a linear scale with each level representing 10% of the data (6875 inactive galaxies). A dashed line is shown at C=2.6 at the separation between early and late types. *Right*: Plot of average concentration index by stellar mass. We find that at low stellar mass (log $M_* < 10$), BAT AGN tend to have higher concentrations than inactive galaxies or SDSS AGN. The error bars indicate standard deviations in each bin.

value for the C, while galaxies with a more shallow light profile, such as spiral and irregular galaxies, will have a lower C. In addition, the concentration index is strongly correlated with the galaxy's bulge to total luminosity ratio as well as the supermassive black hole mass. A plot of concentration vs. stellar mass is shown in Figure 2.6 for BAT AGN compared to inactive galaxies and SDSS AGN. We find that at low stellar mass (log $M_* < 10$), BAT AGN tend to have higher concentrations than inactive galaxies or SDSS AGN indicative of stronger bulges or a larger fraction of elliptical galaxies. However, as shown below, the BAT AGN sample has a very low elliptical galaxy fraction.

While C measurements are useful, they have been shown to be more closely related to luminosity than morphology (Gavazzi et al. 2000). Since the human eye has consistently proven better than computational techniques at identifying faint spiral structure in images (Lintott et al. 2008), we used a catalog of visual classifications from the Galaxy Zoo project DR1 (Lintott et al. 2008). Before morphological classi-

fication, we matched each NL BAT AGN to one inactive galaxy and one SDSS AGN by redshift and stellar mass. We then used the visual classifications of morphology to divide host galaxies into elliptical, spiral, intermediate, and peculiar/merger (Figure 2.7). Each galaxy had on average 37 independent classifications for a total of over 15,000 classifications for the 3 samples. Elliptical or spiral galaxies were defined as galaxies in which on average >80% people selected this type. We define the peculiar/merger category following Patton & Atfield (2008) by requiring a projected separation of <30 kpc and a radial velocity differences of less than 500 km/s between the sample galaxy and its possible companion. The remainder of galaxies we classify as intermediate.

A comparison between the Galaxy Zoo classifications of the samples can be found in Figure 2.8. We find that BAT AGN are more likely to be found in spiral morphologies at a rate (41%) roughly twice that of inactive galaxies (22%) or SDSS AGN (21%). We also find fewer BAT AGN in elliptical or intermediate types. We find that BAT AGN are more likely to be found in merging systems (see Chapter 3 for a detailed discussion). We see no statistically significant differences in the morphologies of inactive galaxies or SDSS AGN.

In addition, we looked at the Hubble Types of the BAT AGN sample compared to the Third Reference Catalog of Bright Galaxies (RC3) to confirm our results with Galaxy Zoo (Figure 2.9). We used all galaxies in the RC3 in the same redshift range as the BAT AGN. The RC3 is composed of bright galaxies with optical B mag<15.5 and size larger than 1′. This restriction excludes many faint galaxies or about 98% of the SDSS sample in the same redshift range. The BAT AGN sample has slightly higher optical luminosities than the RC3 (mean $M_B = -20.33 \pm 0.82$ vs. $M_B = -20.03 \pm 1.03$) and is at similar distances (mean z=0.025±0.01 vs. z=0.019±0.01 for the RC3). We find more BAT AGN in early type Sa-Sb spirals (40%) compared
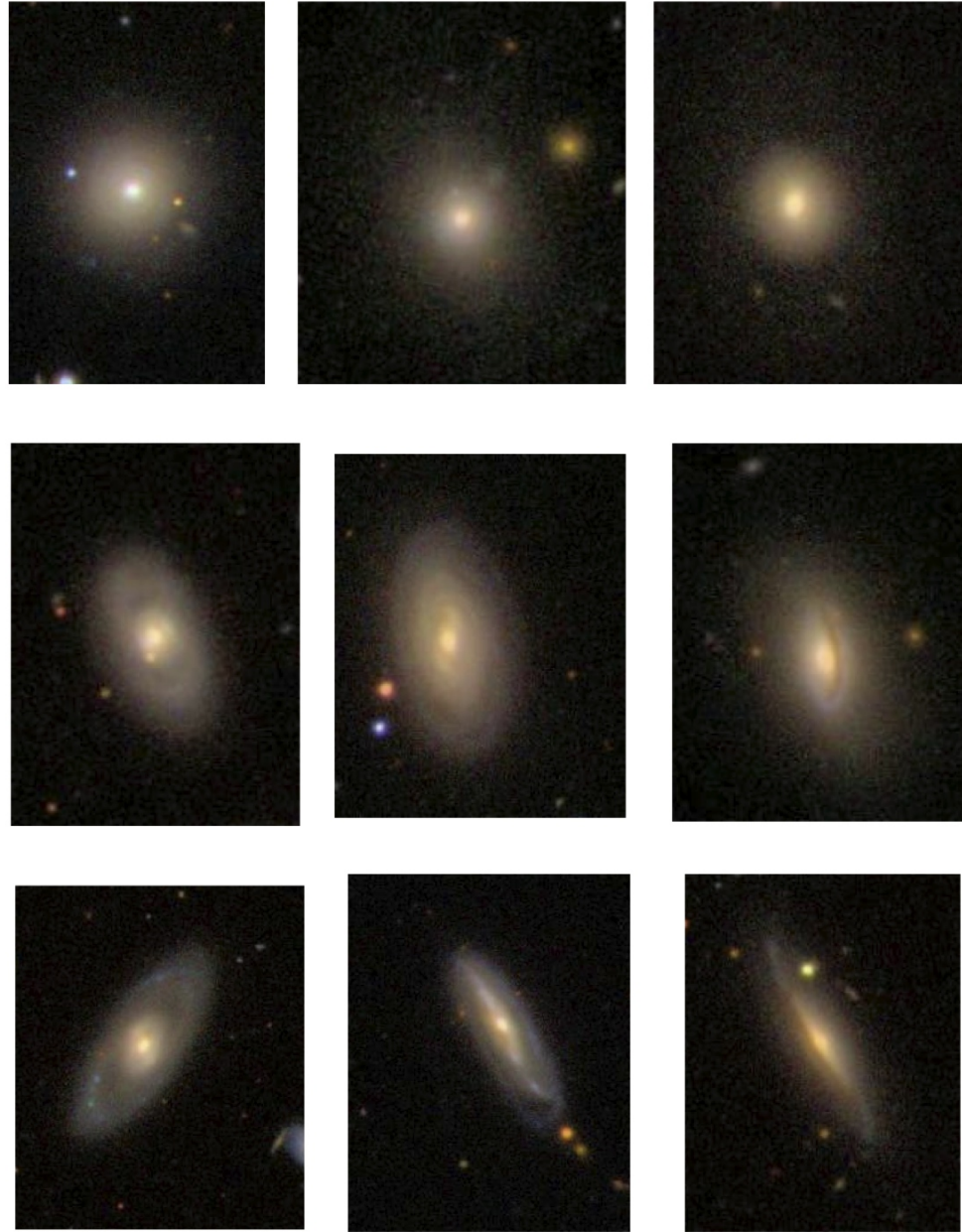
Figure 2.7: Random sample of *gri* composite images of BAT AGN galaxy hosts classified as elliptical (top row), intermediate (second row), spiral (third row), or peculiar/merger (bottom row) from Galaxy Zoo DR1.
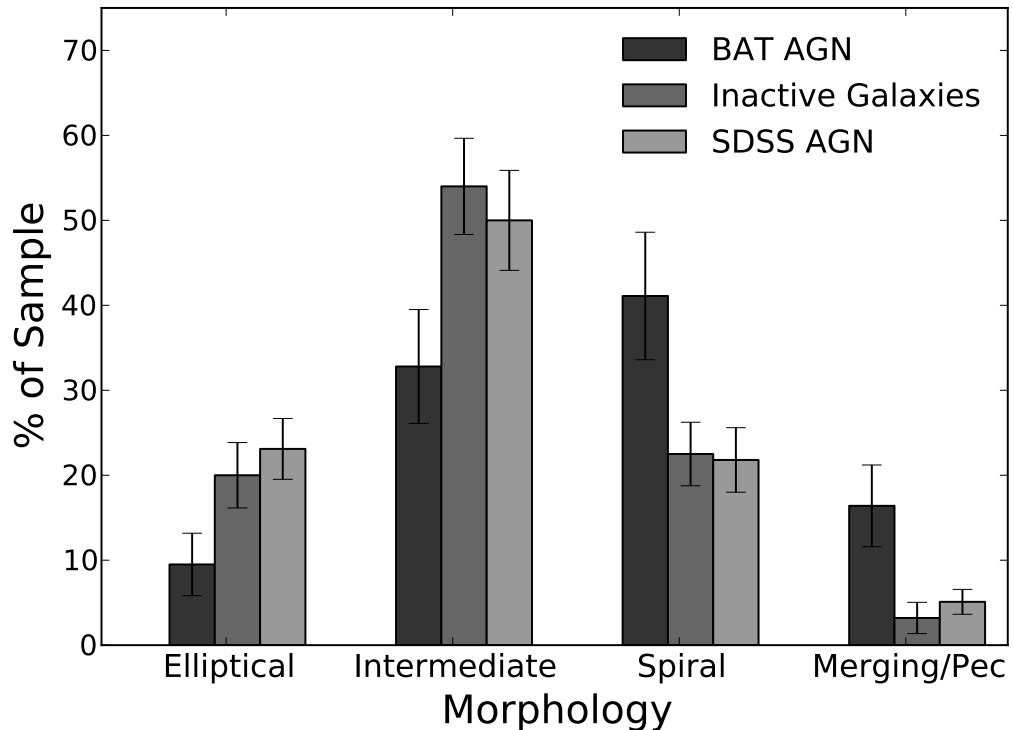
Figure 2.8: Histogram of morphologies from the BAT AGN, inactive galaxies, and SDSS AGN. The morphologies were taken from measurements in the Galaxy Zoo DR1. The error bars represent 1σ Poisson statistics. We find a higher incidence of spirals in the BAT AGN sample and less ellipticals and intermediates. We also find more merging/peculiar types in the BAT AGN sample.

to the RC3 catalog (26%). We see fewer BAT AGN in ellipticals (3%) compared the RC3 catalog (16%). The larger number of spiral morphologies in the BAT AGN sample is consistent with our analysis of morphologies using Galaxy Zoo.

Since spiral galaxies tend to be found in less massive systems than elliptical galaxies, we examined the relationship between morphology and stellar mass. For the BAT AGN in spirals, we find a higher average stellar mass (log M_*=10.34±0.27) than in ellipticals and intermediates (log M_*=10.07±0.42). A K-S test indicates that the probability is <4% that the populations are the same. This finding is in agreement with Schawinski et al. (2010) who found that optical AGN in elliptical systems
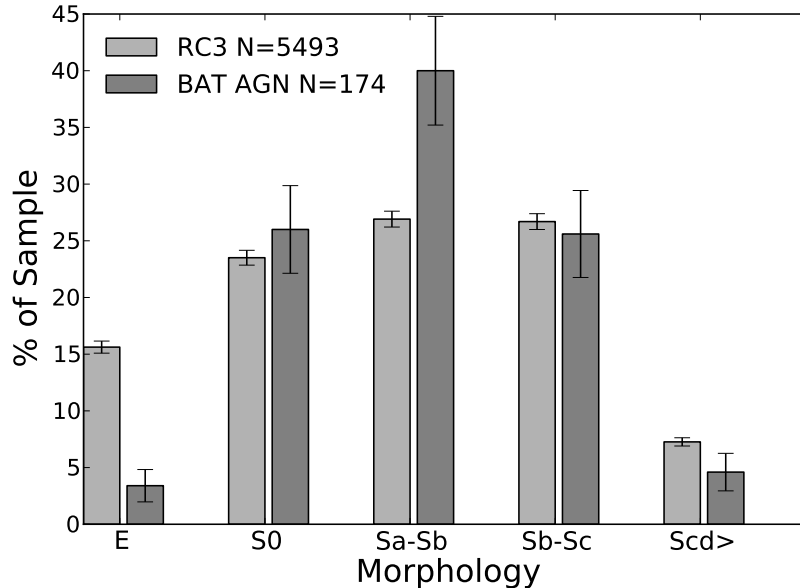
Figure 2.9: Hubble types of 174 BAT AGN host galaxies from HyperLeda. The RC3 catalog includes all galaxies in the same redshift range as the BAT AGN. In this system, T = -6 to -4 correspond to ellipticals (E), T = -3 to 0 to lenticulars (S0), T = 1 to 3 to early type spirals (Sa-Sb), T = 4 to 6 to spirals (Sb-Sc), and T>6 to late type spirals (Scd>). Poisson statistics are assumed in the error bars. We find more BAT AGN in early type Sa-Sb spirals (40%) compared to the RC3 catalog (26%). We see fewer BAT AGN in ellipticals (3%) as compared the RC3 catalog (16%).

tend to be in less massive systems. We further investigated the predominance of massive spirals amongst BAT AGN by plotting the ratio of the number of spiral to elliptical galaxies by stellar mass (Figure 2.10). For massive systems (log M_* >10.5), we find that BAT AGN are found in spirals at a rate that is 5 to 10 times higher than optical AGN or inactive galaxies.

We also examined the galaxy inclination. A study of SDSS galaxies by Maller et al. (2009) found that elliptical galaxies rarely have small axis ratios, and galaxies with b/a<0.55 are 90% disk galaxies. Therefore the axis ratio can be a reliable quantitative tracer of morphology. To enable comparison with the SDSS catalog, we used the galaxy axis ratio in the g band (b/a). The axis ratio (b/a) is determined
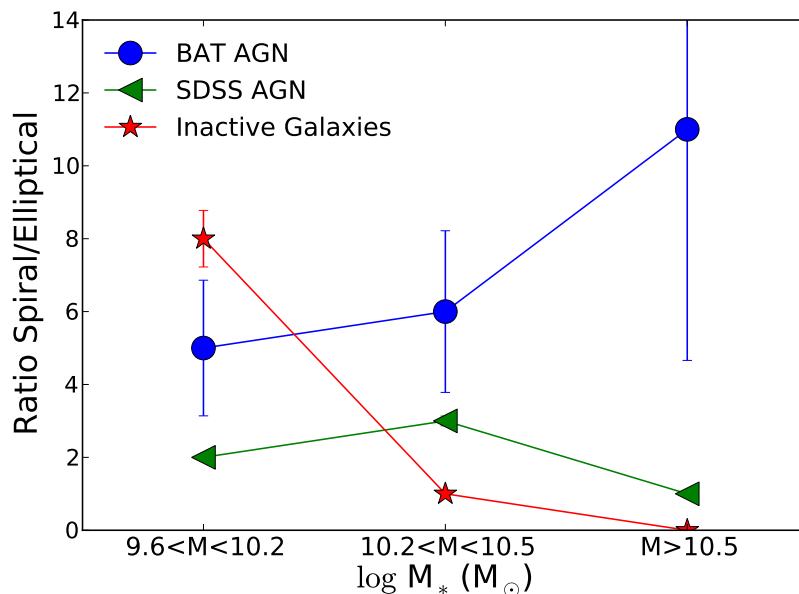
Figure 2.10: Ratio of the number of spiral to elliptical galaxy morphologies as a function of stellar mass (M_*). Galaxy morphologies are taken from Galaxy Zoo. The error bars represent 1σ Poisson statistics. We find that the BAT AGN have a much larger number of massive spirals (log $M_* > 10.5$) and very few ellipticals compared to inactive galaxies or optical AGN.

from the major and minor axes derived from SDSS isophotal photometry. A plot of axis ratios of the samples can be found in Figure 2.11. For the axis ratios, we find a larger percentage of NL BAT AGN have b/a<0.55 which is where Maller et al. (2009) found almost 90% disk-like systems. This result is consistent with the increased incidence of spirals found by Galaxy Zoo for the BAT AGN. We find no difference between the axis ratios of the inactive galaxies or SDSS AGN.

Previous studies have suggested that optical emission line classification of Seyfert galaxies may be missing a population of edge on galaxies (Kirhakos & Steiner 1990; Simcoe et al. 1997). Since the NL BAT AGN are more likely to be in disk galaxies which have lower axis ratios, we separated the samples by morphology in Galaxy Zoo and then did a comparison of axis ratio. In this case we do not see any statistically
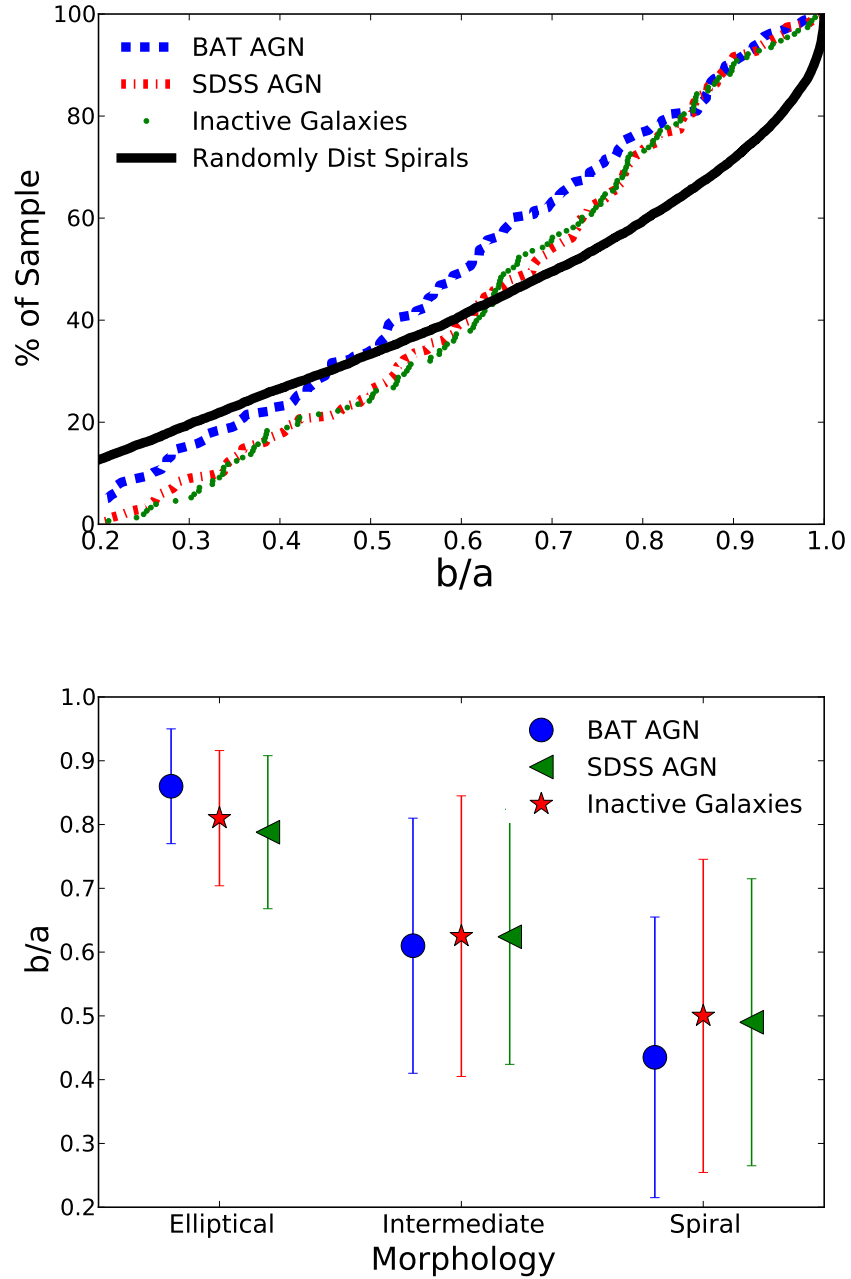
Figure 2.11: *Upper panel*: cumulative distribution of galaxy axis ratios in the r band (b/a) for the NL BAT AGN, inactive galaxies, and SDSS AGN. The axis ratio (b/a) is determined from the major and minor axes derived from SDSS isophotal photometry. Randomly distributed spirals with a $\cos\theta$ distribution of axis ratios is shown for reference. We find that more NL BAT AGN have b/a<0.55 than inactive galaxies and SDSS AGN. This limit is where Maller et al. (2009) found almost 90% disk-like systems, and is consistent with increased incidence of spirals in NL BAT AGN compared to inactive galaxies and SDSS AGN. *Lower panel*: comparison of axis ratios by morphology type within each sample. We do not find evidence that BAT AGN are preferentially in inclined systems when compared by morphology type.

37

significant difference in axis ratios between NL BAT AGN spirals compared to spirals in inactive galaxies or SDSS AGN.

Finally, the SDSS catalog provides independent measurements of the fraction of early type galaxies from the photometry and spectroscopy. The SDSS spectroscopic parameter eClass classifies the spectral type of the galaxy using the principal component analysis technique, and the photometric parameter fracDev_r measures the fraction of galaxy light that is fitted by a de Vaucouleurs law. Following Bernardi et al. (2003) we define as early type galaxies those objects with eClass<0 from spectroscopy and $\text{fracDev}_r > 0.8$ from photometry. In this comparison we only use NL BAT AGN with spectroscopy in the SDSS (185). We find a statistically smaller number of NL BAT AGN in early type galaxies (39%±8), compared to inactive galaxies (61%±6) or SDSS AGN (56%±6). The error bars represent 1σ Poisson statistics. These results are consistent with a spectroscopic study of 64 BAT AGN which found that the majority of NL BAT AGN have spectra consistent with late type galaxies based on measurements of the stellar absorption indices (Winter et al. 2010). The percentage of BAT AGN galaxies classified as early type galaxies (39%±8) using SDSS spectroscopy is significantly larger than that based on morphological measurements from the RC3 or galaxy zoo (3% and 10% respectively). This is likely because the SDSS spectroscopy uses a 3″aperture and is measuring only the central bulge portion of the galaxy.

2.4.3   Colors, Morphology, and Ultra Hard X-ray Emission

Since we found BAT AGN host galaxies have a greater number of merger and spiral morphologies, an additional question is how this is related to host galaxy colors. To test this we used a sample of BAT AGN in the process of mergers (see chapter 3) and did a comparison of their host galaxy colors compared to those BAT AGN not in
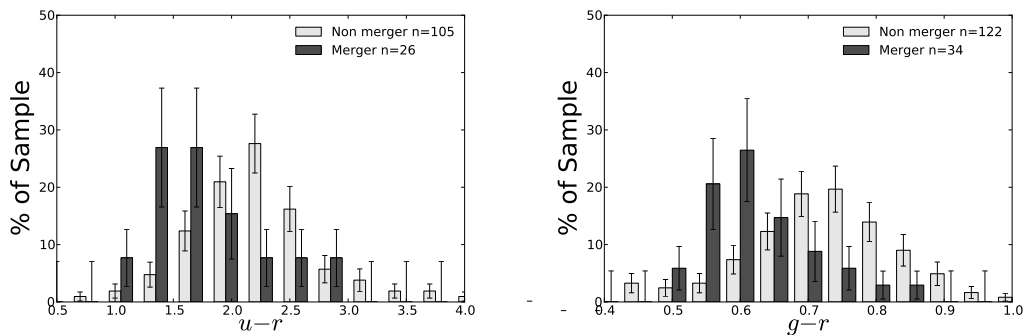
Figure 2.12: Histogram of $u - r$ and $g - r$ colors of BAT AGN in major mergers vs. BAT AGN that are not in major mergers. The error bars represent 1σ Poisson statistics. The merging galaxies show a bluer distribution of colors than non-mergers.

mergers. A histogram of the merger and non-merger sample is shown in Figure 2.12. When separated by color, we find that the merging population has bluer colors and hence is likely to have an increased level of star formation. We also find that spiral morphologies have bluer average colors than elliptical or intermediate morphologies (Figure 2.13).

Since galaxies of different morphologies tend to have different colors, we examined the colors of spirals in the BAT AGN, inactive galaxy, and SDSS AGN samples to look for differences. In Figure 2.14, we show a plot of the colors of galaxies classified as spirals in Galaxy Zoo. We find a much smaller difference in colors of the three samples when we compare only galaxies with spiral morphologies. This suggests that the higher incidence of spirals in the BAT AGN sample may largely account for the bluer host galaxy colors when compared to SDSS AGN or inactive galaxies.

A plot showing the color of each BAT AGN and its morphology can be found in Figure 2.15. We also show the inactive galaxy colors with contours. We find that the BAT AGN occupy a unique space in color, morphology, and stellar mass by tending to be in massive spirals and mergers that are bluer than massive ellipticals.

In terms of ultra hard X-ray luminosity, we do not find a significant difference
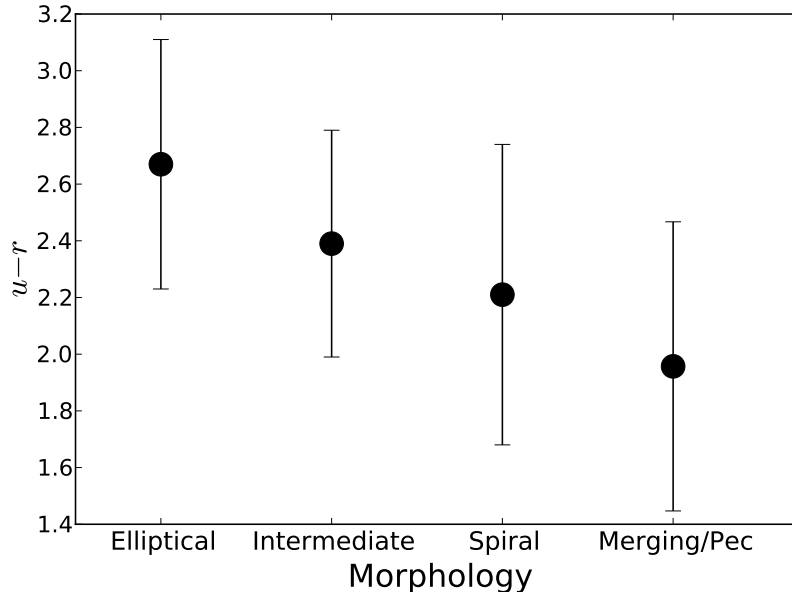
Figure 2.13: Average $u - r$ color for different morphologies of BAT AGN. The error bars indicate standard deviations in color for each morphology. Galaxy morphologies were taken from Galaxy Zoo. We find spiral and merger morphologies are on average bluer than elliptical or intermediate morphologies. We find a similar trend in $g - r$.

between ellipticals, intermediates, or spirals. However, we do find a larger mean ultra hard X-ray emission from BAT AGN in mergers (log $L_{14-195\,\mathrm{keV}}$ =43.64±0.48) when compared to the non-merger sample (log $L_{14-195\,\mathrm{keV}}$ =43.32±0.61). A K-S test indicates a <5% probability that the ultra hard X-ray emission from AGN in mergers is from the same population as the non-merger sample.

2.4.4 Stellar Masses and Ultra Hard X-ray Emission

We find that the BAT AGN host galaxies are predominantly in the most luminous and massive of galaxies. The mean optical luminosity is higher for BAT AGN (M_r of -21.41±0.82) compared to inactive galaxies (-19.84±1.03), and SDSS AGN (-20.95±0.69). The BAT AGN also have higher mean stellar mass (log M_*=10.28±0.4)
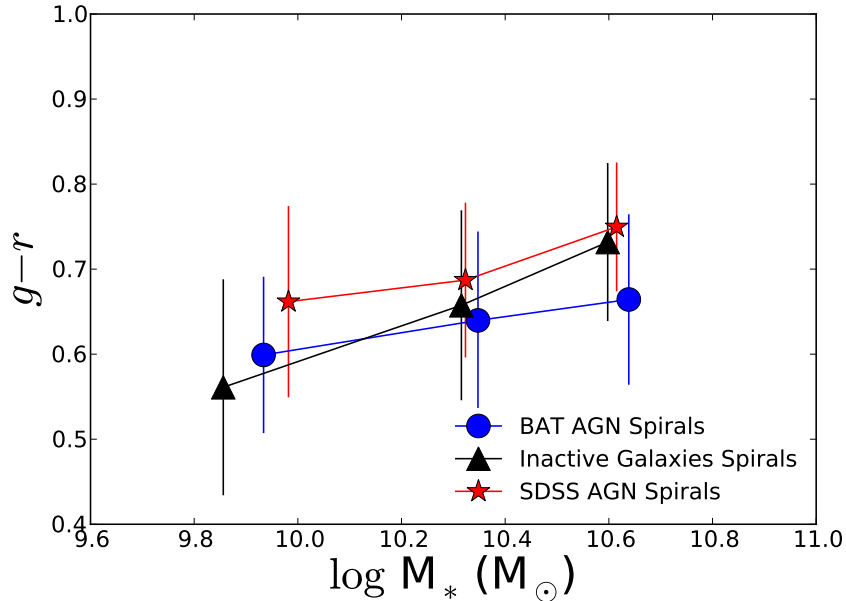
Figure 2.14: Plot of Petrosian $g-r$ for BAT AGN spirals, inactive galaxy spirals, and SDSS AGN spirals. The error bars indicate standard deviations in each bin. We find a much smaller difference in colors of the three samples when we compare only galaxies with spiral morphologies. We find a similar trend in the $u-r$ colors. This suggests that the higher incidence of spirals in the BAT AGN contributes to the bluer colors found when compared to the SDSS AGN or inactive galaxies.

compared to inactive galaxies (9.46±0.58) and SDSS AGN (10.18±0.28). This suggests that the BAT AGN tend to be in more massive galaxies than the SDSS AGN or inactive galaxies. See Figure 2.16 for a histogram of the stellar masses of the populations. A K-S test has <0.01% probability that the BAT AGN stellar masses are from the same population as the inactive galaxies or SDSS AGN. We also confirm that SDSS AGN are in more massive galaxies than inactive galaxies (Kauffmann et al. 2003a). We also fit a Schechter function (Figure 2.17) and find that the logarithm of the characteristic stellar mass (M^*) from the best fit is 10.28, 10.02, and 9.89 for the BAT AGN, SDSS AGN, and inactive galaxies in agreement with our findings that BAT AGN are more massive than inactive galaxies or SDSS AGN.

We also find that the average hard X-ray luminosity increases with stellar mass
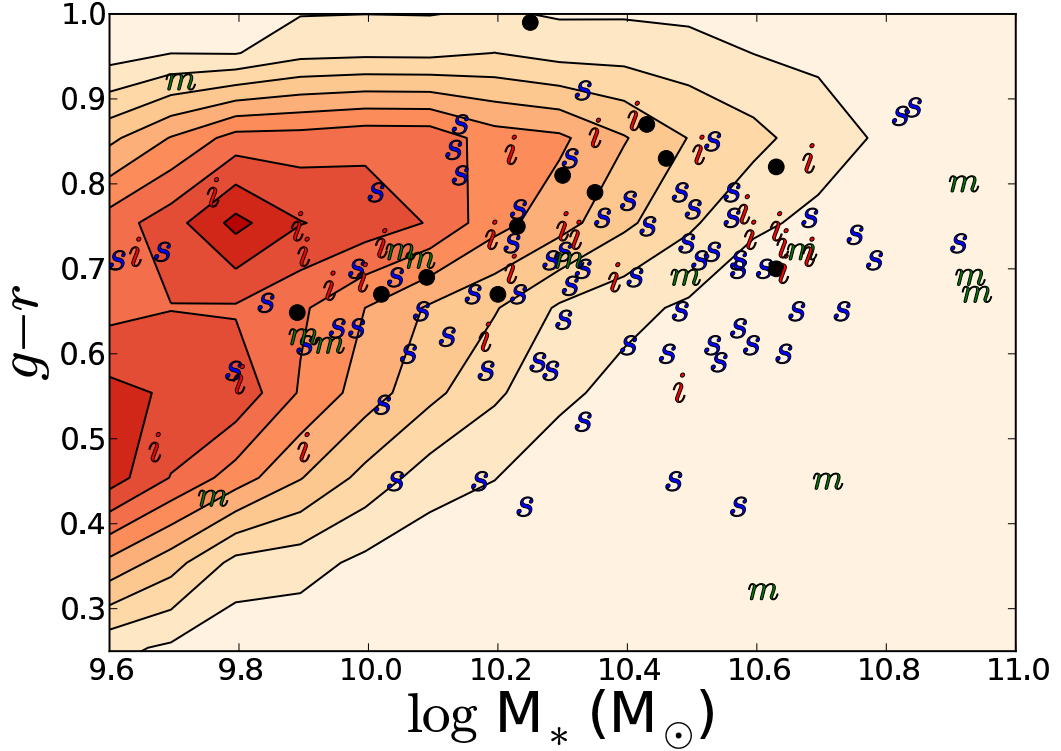
Figure 2.15: Petrosian $g - r$ of BAT AGN (black dots and letters) and inactive galaxies (contours) plotted as a function of logarithm of the stellar mass (M_*). The contour levels are plotted on a linear scale with each level representing 10% of the data (6875 inactive galaxies). In the BAT AGN sample, m, denotes a galaxy in a merger, s, a spiral morphology, i an intermediate morphology, and black dots denote ellipticals. We find a predominance of BAT AGN in blue, massive spirals and mergers in the regions outside of where most inactive galaxies lie. We find a similar trend in the $u - r$ colors.

(Figure 2.18). The lowest quartile stellar mass has log $L_{14-195\,keV} = 43.07 \pm 0.88$ and the highest quartile stellar mass has log $L_{14-195\,keV} = 43.72 \pm 0.36$. In the lowest stellar mass quartile 34% of sources have log $L_{14-195\,keV} < 43$ while in the highest stellar mass quartile none of the sources have log $L_{14-195\,keV} < 43$. A K-S test has $< 0.2\%$ probability that the distributions of ultra hard X-ray luminosities are the same for the lowest quartile and highest quartile of stellar mass. In addition, for the average stellar masses, we find a linear correlation between log $L_{14-195\,keV}$ and
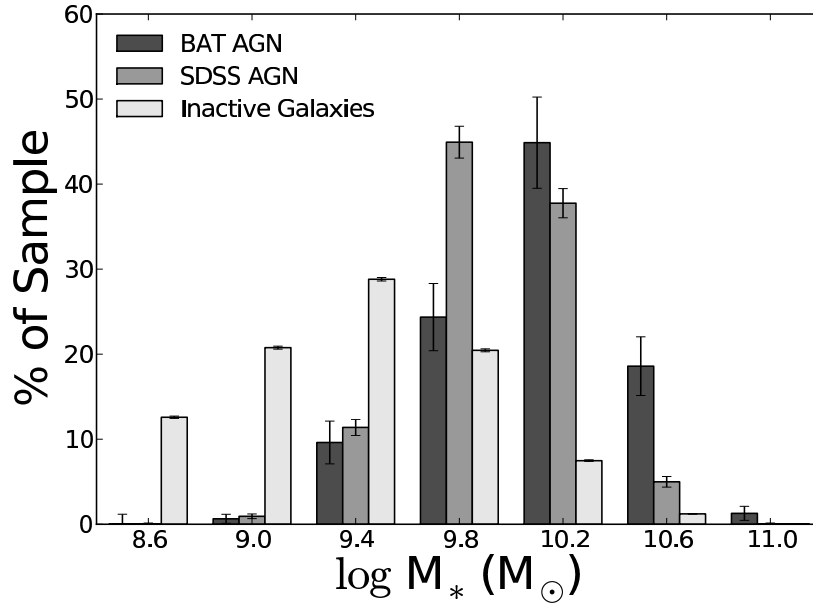
Figure 2.16: Histogram of stellar masses (M_*) of the BAT AGN sample compared to inactive galaxies and SDSS AGN. The error bars represent 1σ Poisson statistics. The BAT AGN have significantly higher average stellar masses (mean log M_*=10.27±0.4) than inactive galaxies (9.45±0.58) and slightly higher stellar average stellar masses than SDSS AGN (10.18±0.28).

log M_* with a slope of 0.62±0.14 and a less than 2% probability that the values are uncorrelated.

2.4.5   Tests of Unification Model

We also tested the Unified Model of Seyferts using the BAT sample. In this model, it is assumed that all AGN are the same types of objects so host galaxy properties such as color, star formation, and morphology should be independent of the Seyfert type or level of obscuration toward the central engine.

We find that the host galaxy colors of narrow and broad-line AGN are the same in agreement with the unification model. Both the $g-r$ and $u-r$ colors of broad-line AGN and NL AGN after GALFIT subtraction for AGN emission are very similar
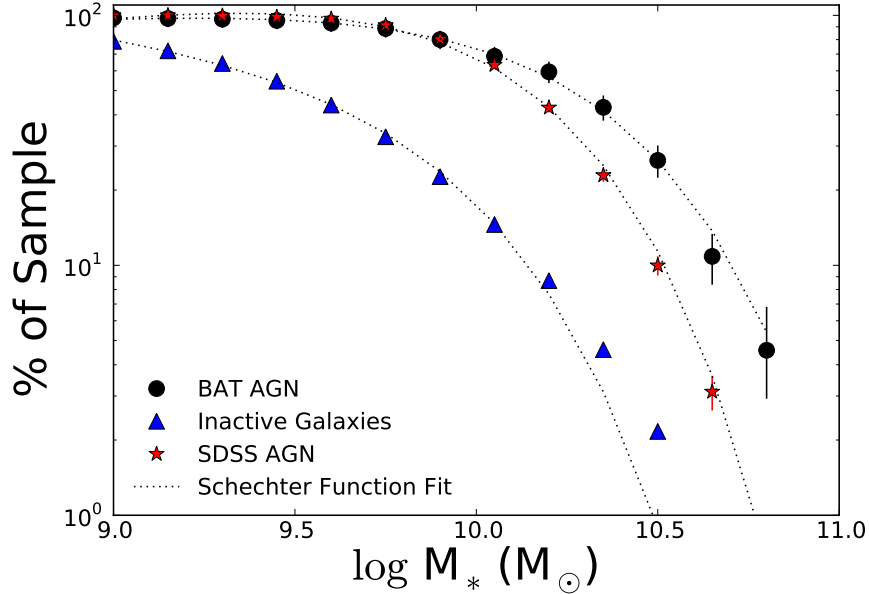
Figure 2.17: Plot of binned cumulative galaxy stellar mass function for the BAT AGN, SDSS AGN, and inactive galaxy sample. A single Schechter function has been fit to each sample (dotted line). We find that the logarithm of the characteristic stellar mass (M^*) from the best fit Schechter function is 10.28, 10.02, and 9.89 for the BAT AGN, SDSS AGN, and inactive galaxies respectively. This suggests that the BAT AGN tend to be in more massive galaxies than the SDSS AGN or inactive galaxies. The faint end slope (α, where M< M^*), is 0.09, 0.21, and -0.15 for the BAT AGN, SDSS AGN, and inactive galaxies respectively.

(Figure 2.19). For broad-line AGN, the mean $g - r$ is 0.66±0.15 and for NL, the mean $g - r$ is 0.68±0.12 with P(K-S)=43% that the populations are the same. In $u - r$, the color for broad-line AGN is 2.16±0.55 and NL AGN is 2.18±0.61 with P(K-S)=99% that the populations are the same.

An additional test of the Unified Model can be done by checking whether there is any correlation between color and column density in the BAT sample. Column densities were obtained from the literature (Bassani et al. 1999; Noguchi et al. 2010; Winter et al. 2008, 2009) and the Tartarus database. We see no correlation between column density and host galaxy color (Figure 2.20). Since host galaxy color measures the relative amount of star formation, this suggest that there is no relation between
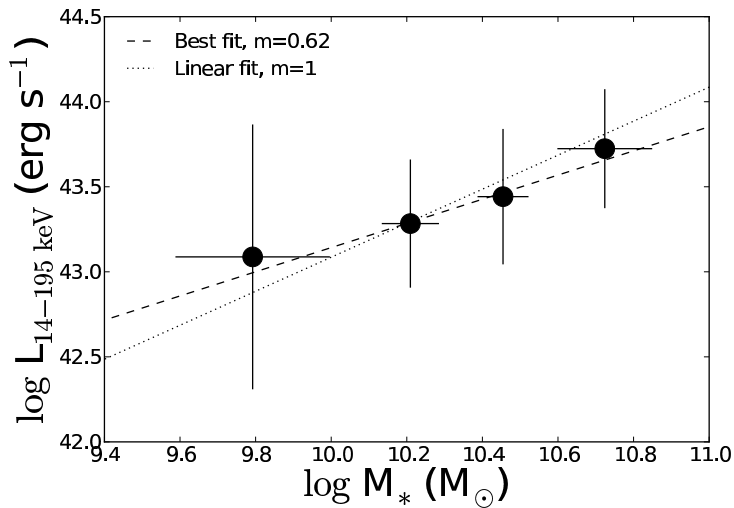
Figure 2.18: Plot of average ultra hard X-ray luminosity vs. stellar mass. Error bars represent the standard deviations in each bin. We find greater ultra hard X-ray emission for galaxies with larger stellar mass. A K-S test has <0.2% probability that the distributions of ultra hard X-ray luminosities are the same for the lowest quartile and highest quartile of stellar mass. In addition, for the average stellar masse, we find a correlation between $\log L_{14-195\,keV}$ and $\log M_*$ with a slope of 0.62 ± 0.17 and a less than 2% probability that the values are uncorrelated. We have also plotted a line with a linear fit between stellar mass and ultra hard X-ray emission.

X-ray column density (N_H) and star formation.

We also investigated whether the NL and broad-line AGN have different rates of star formation in the far-IR. We define a proxy for specific star formation rate as the logarithm of the ratio of 90 μm emission from *AKARI* to stellar mass. The mean value for this parameter for the narrow-line AGN is 33.6 ± 0.4 erg s$^{-1}M_\odot^{-1}$ and for broad-line AGN is 33.4 ± 0.4 erg s$^{-1}M_\odot^{-1}$. A K-S test indicates a 35% probability that the rates of specific star formation for the narrow and broad-line AGN are the same in agreement with the Unified Model of AGN.

In addition, we compared the morphologies of broad and narrow-line AGN. Because of the difficulty of determining morphology class for galaxies with very bright AGN, we limited our sample to galaxies where AGN PS component contributes less
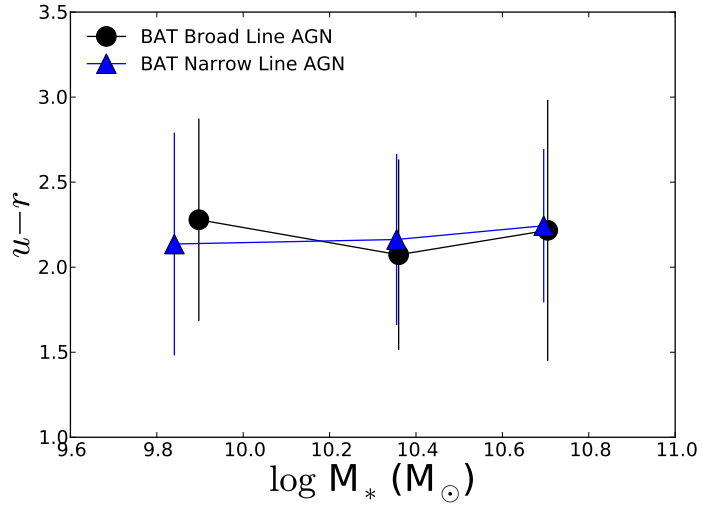
Figure 2.19: Comparison of average BAT AGN host galaxy colors separated by broad-line and narrow-line. The error bars indicate standard deviations in each bin. Petrosian $u - r$ by stellar mass (M_*) for broad-line and narrow-line AGN in the BAT sample. Both narrow-line and broad-line AGN show similar host galaxy colors in agreement with AGN unification with P(K-S)= 99% and 36% for $u - r$ and $g - r$ respectively.
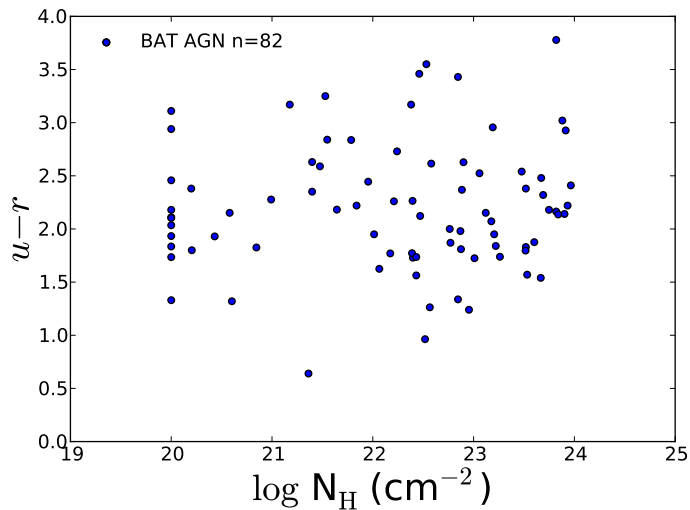
Figure 2.20: Scatter plot of X-ray column density vs. host galaxy $u - r$. We see no correlation of X-ray column density with host galaxy color in agreement with AGN unification. We also find no correlation in $g - r$.
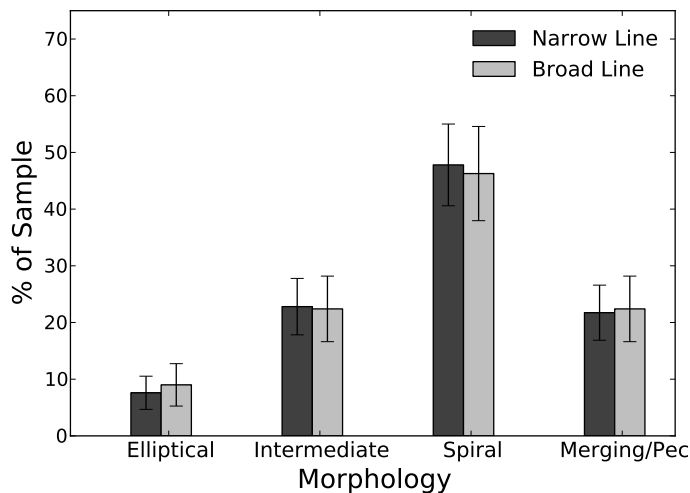
Figure 2.21: Comparison of BAT AGN host galaxy morphologies separated by broad and narrow-line AGN. The error bars represent 1σ Poisson statistics. We see no difference in the morphologies of the two samples in agreement with AGN unification.

than 35% of the total light in the r band ($\%PS_r < 35$). A plot of the percentage in each sample of different types of morphology can be found in Figure 2.21. We see no difference in the morphologies of broad and narrow-line AGN.

Finally, we compared the axis ratios of BAT AGN with different optical classifications and obscuring column densities. In the unified model of Seyferts, the observed X-ray spectra of Seyfert 2s are expected to have higher absorbing column density than Seyfert 1s due to an edge-on view of the obscuring torus. However, edge-on spirals have been shown to have a geometrically thick layer of obscuring material in the host-galaxy planes that can also increase the absorbing column density (Simcoe et al. 1997). We confirm this by finding more NL AGN in highly inclined systems with smaller axis ratios (b/a<0.4; Figure 2.22, left). We also compared X-ray column density vs. host galaxy inclination and found more inclined systems tend to have higher average X-ray column densities (Figure 2.22, right). This finding confirms an earlier result from the smaller 9-month sample of BAT AGN (Winter
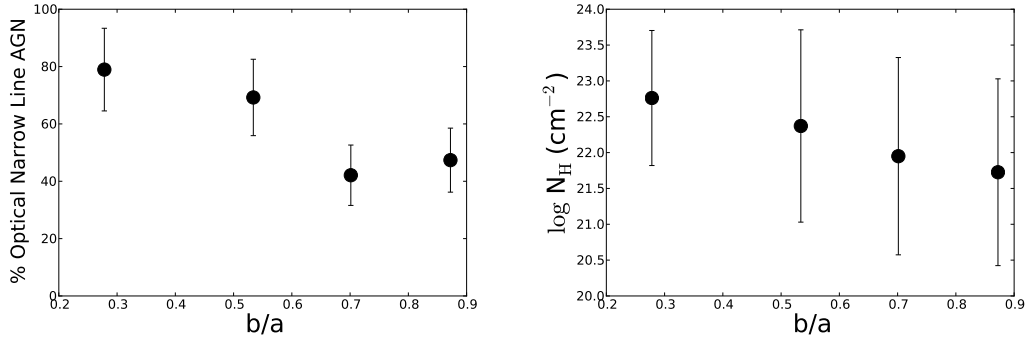
Figure 2.22: *Left*: Percent of narrow-line AGN vs. host galaxy inclination as measured by the axis ratio (b/a). The error bars indicate standard deviations in each bin. Galaxies with lower axis ratios tend to be more edge on. We find more NL AGN in highly inclined systems with smaller axis ratios. *Right*: X-ray column density vs. host galaxy inclination as measured by the axis ratio (b/a). The error bars indicate standard deviations in each bin. Galaxies with higher inclinations have a higher mean X-ray column density. A K-S test indicates a <5% probability that the X-ray column densities from the lowest and highest distributions of axis ratios are from the same parent population.

et al. 2009).

2.5   Summary and Discussion

We have assembled the largest sample of ultra hard X-ray selected AGN with host galaxy optical data to date, with 185 AGN in total. We have performed extensive modeling with GALFIT to effectively remove the AGN light from the optical images. Using optical photometry, morphology, and spectroscopy, along with FIR emission we found:

(i) The BAT AGN galaxies are bluer in optical color than inactive galaxies or SDSS Seyferts of the same stellar mass.

(ii) We find a much higher incidence of spiral morphologies in BAT AGN compared to SDSS AGN or inactive galaxies. Amongst massive galaxies ($\log M_* > 10.5$),

the BAT AGN show a preference for spiral morphologies that is 5 to 10 times higher than SDSS AGN or inactive galaxies. We also find that the bluer colors of BAT AGN can be accounted for by a higher fraction of mergers and spirals.

(iii) The BAT AGN have greatly enhanced 90 μm emission compared to inactive galaxies or SDSS Seyferts matched in redshift and stellar mass.

(iv) The BAT NL AGN have similar intrinsic [O III] λ5007 luminosities as NL SDSS Seyferts of the same redshift range.

 (v) The BAT AGN are found in the most massive host galaxies with high concentration indexes indicative of large bulge-to-disk ratios and large supermassive black holes.

(vi) We also find that the average ultra hard X-ray luminosity increases with stellar mass and that BAT AGN in mergers have greater ultra hard X-ray emission than those in other morphological types. This suggests a link between supermassive black hole growth and the mass of the host galaxy.

(vii) In agreement with the Unified Model of AGN, we find the host galaxy colors and morphology are independent of X-ray column density and optical Seyfert classification.

These results indicate that host galaxy morphology is related to the activation and fueling of local AGN. Ultra hard X-ray selected AGN are particularly associated with massive spiral galaxies and galaxy mergers. These types of objects are generally associated with bluer colors, compared to the red massive early-type galaxies at similar stellar masses. These observational results provide some evidence for an association between AGN activity and galaxy mergers (e.g., di Matteo et al. 2005), and also provide examples of AGN activity driven by the stochastic accretion of cold

gas that should be more prominent among late-type systems (Hopkins & Hernquist 2006).

Recent simulations have also suggested a transition between the fueling mechanisms of AGN with nonmerger events predominantly powering lower luminosity AGN and merger-induced fueling dominant in more luminous quasars (Hopkins & Hernquist 2009). We may be seeing evidence of this transition in our sample of BAT AGN that is powered both through merger events and less powerful nonmergers such as accretion of cold gas in late type systems. In support of this, we find that BAT AGN in mergers have a greater ultra hard X-ray emission than those in other morphological types. However, only a very small fraction (5/185) of BAT AGN in this sample are above the minimum bolometric luminosity associated with quasars ($L_{bol} > 10^{45}$ erg s^{-1}). These results suggest that the process of merging may be important for powering more moderate luminosity AGN as well (see also Chapter 3).

In interpreting the results of an X-ray flux limited survey, it is useful to remember that the observed flux is a product of the black hole mass and accretion rate. On average, more massive galaxies will tend to have higher mass black holes that will produce a larger average X-ray flux than smaller galaxies with on average smaller black holes. However, among massive galaxies, elliptical morphologies are much more common than spirals, yet we find the most luminous hard X-ray AGN almost exclusively in spiral morphologies. This suggests that spiral morphologies must have higher accretion rates than elliptical morphologies. This finding is in agreement with recent theoretical predictions that suggest that only spirals typically have enough gas to trigger higher levels of radiatively efficient accretion in a geometrically thin disk (Fanidakis et al. 2011). In order to understand this further, we are in the process of accurately measuring black hole masses to study the accretion rates for

this sample.

Previous optical surveys have found that AGN tend to be in massive galaxies (Kauffmann et al. 2003a), occur along the red sequence (Westoby et al. 2007), and tend to have similar numbers of galaxy mergers as inactive galaxies (Li et al. 2006). However, in an ultra hard X-ray survey of AGN, we find that AGN host galaxies are bluer than inactive galaxies with higher numbers of massive spirals and galaxy mergers. We do not find observational evidence that the AGN suppresses star formation.

It is surprising that the optical morphologies and colors of ultra hard X-ray selected AGN are so different than emission line selected Type 2 Seyferts given their similar bolometric luminosity as measured in [O III]. However, these results are consistent with recent Spitzer surveys that have found that the AGN detection rate in late-type galaxies and mergers is much larger than what optical spectroscopic observations suggest (Goulding & Alexander 2009; Satyapal et al. 2008; Veilleux et al. 2009b). Finally, studies of X-ray selected AGN at higher redshifts, have also found a significant population of AGN classified as star forming using emission line diagnostics (Yan et al. 2011, accepted).

In the BAT AGN sample, there are several results that suggest optical emission line classification may be biased against late-type galaxies and mergers. In this study, we found that the axis ratios of BAT AGN are in general more inclined and have greater levels of internal extinction than comparable SDSS AGN. This extinction could obscure or dilute the narrow-line region and cause AGN galaxies to be misclassified as star forming regions. This finding is also in agreement with a previous analysis of BAT AGN that found optical emission line diagnostics preferentially misclassify merging AGN because of optical extinction and dilution by star formation (see also Chapter 3).

Another possibility is that the BAT AGN may be much more intrinsically luminous than their [O III] emission suggests. Since the majority of BAT AGN either have broad lines or are NL AGN that are correctly classified as Seyferts, yet are found to have much greater hard X-ray luminosities, this must be an important factor. In support of this, two studies of BAT AGN have found a very weak correlation between the [O III] and hard X-ray luminosity and that BAT AGN have additional reddening of the narrow line region not accounted for in optical studies (Meléndez et al. 2008; Winter et al. 2010). This is also supported by the much greater number of narrow-line SDSS Seyferts compared to hard X-ray selected AGN. In the SDSS survey area, there are 24 optical emission line selected narrow-line Seyferts detected for each hard X-ray AGN at the same redshift. Some of these undetected sources may be heavily absorbed Compton-Thick AGN missed in the hard X-rays, but even the highest estimates expect only $\approx 50\%$ of local narrow-line AGN are Compton Thick (Risaliti et al. 1999). If the BAT AGN are intrinsically more luminous than [O III] emission line selected AGN, this may explain their higher rates of mergers and enhanced FIR emission. We are currently in the process of assembling a larger survey of optical spectra of BAT AGN to better understand optical and X-ray measures of intrinsic luminosity.

Chapter 3

Merging and Clustering

of BAT AGN

3.1   Introduction

The $Swift$ BAT all sky hard X-ray sample of AGN is uniquely suited to test whether
local AGN are found in mergers or with close companions that may be driving their
AGN activity because it is conducted in the 14–195 keV energy band. This band
is optically thin to much of the dust and gas obscuring the AGN and thus does
not suffer from many of the biases of optical emission line classification of AGN. In
our study of the host galaxies of BAT AGN in the last chapter, we found more in
mergers based on morphological classification. Because of the current controversy
as to whether moderate luminosity AGN like those in $Swift$ BAT are triggered in
mergers, we focus an additional chapter on their merging and clustering of ultra
hard X-ray selected AGN using a sample of 181 BAT-detected AGN.

   Simulations of the growth of black holes suggest that mergers of galaxies trigger
the AGN phenomenon (di Matteo et al. 2005). Tidal torques produced during

the galaxy interaction send gas into the nuclear region to feed the black hole and enhance AGN activity (Domingue et al. 2005). Later in the merger phase the two supermassive black holes coalesce and a rapid accretion phase is entered with a burst of star formation before settling into a relaxed state.

The observational evidence for mergers driving AGN activity has been contradictory and seems to depend on the luminosity of the AGN. Clear evidence for higher incidence of mergers is seen among QSOs (Serber et al. 2006; Veilleux et al. 2009a). Early studies of the environment of Seyfert galaxies also appeared to show an excess of close companions (Petrosian 1982), but recent studies of typical AGN have found no evidence for higher rates of mergers or close companions (Miller et al. 2003). For instance, X-ray studies of AGN at intermediate redshifts did not find increased levels of mergers or close neighbors (Grogin et al. 2005). Host galaxies of AGN in the COSMOS survey do not have greater numbers of nearest neighbor galaxies or disturbed morphologies compared to normal galaxies (Gabor et al. 2009). Finally, Li et al. (2006) analyzed 90,000 local (z <0.1) optically selected narrow-line AGN from the Sloan Digital Sky Survey (SDSS) and found that only 1 in 100 AGN has an extra neighbor within 70 kpc when compared to a control sample. At larger scales between 100 kpc and a Mpc, AGN were clustered more weakly than normal galaxies.

Recent studies of the BAT AGN sample have indicated that it may have increased rates of mergers. For instance, Schawinski et al. (2009b) found an excess of residuals in the images after galaxy model subtraction with GALFIT for 16 BAT AGN. Winter et al. (2009) also found 33% of BAT galaxies as peculiar or disturbed galaxies based on visual inspection of the 9 month survey.

Section §3.2 describes our imaging and spectroscopic data and the analysis technique for measuring the incidence of nearby companions, §3.3 describes our results

and whether merging galaxies may have higher levels of optical extinction or dilution by star formation, and finally the results are summarized in §3.4.

3.2 Data and Analysis

For our analysis, we considered three samples. We studied a sample of BAT-detected AGN galaxies, a control sample of inactive galaxies from the SDSS matched to the BAT sample, and finally a sample of type 2 Seyferts from the SDSS matched to the BAT sample. We will henceforth refer to the three samples as BAT AGN, the control sample, and SDSS AGN, respectively. Our BAT AGN sample consists of nearby ($z < 0.05$) AGN and the total sample includes 181 BAT-detected AGN host galaxies, $\approx 90\%$ of the entire northern hemisphere AGN sample. In this BAT AGN sample, 72/181 galaxies have spectral and imaging coverage of galaxy neighbors in the SDSS. We used these 72 BAT AGN to compare to the other two samples. We subtracted the AGN contribution using GALFIT (Peng et al. 2002) for the broad-line AGN in the SDSS and Kitt Peak (see Chapter 2) images in the BAT sample.

We generated a control sample of inactive galaxies to compare apparent merger rates. Recent studies have found that merger rates are strongly linked to stellar mass and star formation. Geller et al. (2006) found increased star formation with smaller galaxy separation. In addition, Patton & Atfield (2008) found that at least 90% of all major mergers occur between galaxies which are fainter than $L^\star$. Therefore, to construct our control sample we used galaxies in the SDSS that have matched stellar masses, g–r colors (as a proxy for star formation), and redshift. From the comparison sample we excluded broad-line AGN using the SDSS galaxy class and narrow-line AGN using the Garching catalog (Kauffmann et al. 2003b). We also limited the redshifts to $z > 0.01$ because of the tendency of the automated SDSS photometry

to shred bright galaxies into multiple components. We selected 2 matched control galaxies for each of the 72 BAT AGN for a total size of 144 control galaxies.

We also used a sample of emission line selected AGN in the SDSS for comparison, which we refer to as the SDSS AGN. Winter et al. (2010) found that the majority (75%) of a sample of 64 BAT AGN were Seyferts. We therefore chose a sample of type 2 Seyferts from the Garching catalog using the emission line diagnostics of Kewley et al. (2006). We matched each of the 72 BAT AGN to the SDSS Seyfert sample in terms of color, stellar mass, and redshift for a total of 72 SDSS AGN.

We applied the same analysis technique to each of the three samples. To determine stellar masses we used the software kcorrect (Blanton & Roweis 2007) with the *ugriz* photometry. To determine the redshifts of possible companion galaxies we used the spectroscopic sample from the SDSS DR7. Since there is a 55″ fiber collision limit in the SDSS, as well as apparent magnitude limits for the spectroscopic survey, we supplemented our spectroscopic data for companions. We added any spectroscopic data of galaxy companions publicly available through NED closer than a projected separation of 30 kpc. In the range of 30 kpc to 1 Mpc we only used the redshifts of galaxy companions in the SDSS. Throughout this work, we adopt the following cosmological parameters to determine distances: $\Omega_m = 0.3$, $\Omega_\Lambda = 0.7$, and $H_0 = 70$ km s^{-1} Mpc^{-1}. We define apparent mergers as galaxies that show close physical pairs (with a real-space separation of <30 proper kpc) or clear signs of a disturbed morphology such as tidal tails or bridges between galaxies based on visual inspection of three-color images.

We measured the closest companion to each member of our BAT AGN, control, and SDSS AGN samples on scales up to 1 Mpc. To decide whether the neighboring galaxy is at the same radial distance, we followed the criteria of Patton & Atfield (2008) and used radial velocity differences of less than 500 km s^{-1} between the

sample galaxy and its possible companion. We also looked at the *gri* composite image of each galaxy for signs of recent mergers such as tidal tails, binary nuclei, and disturbed morphologies.

3.3 Results

We find that 18% (13/72) of the BAT AGN galaxies have disturbed morphologies consistent with a recent merger. Another 4 BAT AGN (6%) are in close physical pairs with separations of 20–30 kpc, where tidal effects are considerably weaker. Finally, one additional BAT AGN (1%) shows a single nucleus with signs of tidal tails. The overall fraction of BAT AGN undergoing mergers is therefore 25% (18/72). A full listing of the BAT AGN galaxies in apparent mergers is in the top panel of Table 3.3. In Figure 3.1, we show images of nine of these galaxies selected at random from Table 3.3. In the control sample we find only 1% in apparent mergers and for the SDSS AGN sample we find 4%. This small rate is consistent with that of Patton & Atfield (2008) who found merger rates of 2% for normal galaxies at similar distances and cosmology and other studies that have found no differences in merger rates between optically selected AGN and normal galaxies.

We also searched for galaxy companions to BAT AGN outside of the SDSS spectroscopic sample using NED. For the 109 BAT AGN with images and spectra obtained at Kitt Peak, we find a lower rate of 22/109 or 20% in apparent mergers. This lower number is expected because of the reduced number of spectra of galaxy companions in NED. A listing of these BAT AGN in apparent mergers is in the bottom panel of Table 3.3.

Application of our technique to an independent sample of INTEGRAL-selected AGN detected in the hard X-rays (z <0.05, Beckmann et al. 2009) in the northern

Table 3.1.   BAT AGN in Apparent Mergers

Galaxy Name[1]	z	log $\frac{M^*}{M_\odot}$[2]	Dist (kpc)[3]	Disruption[4]	Companion[5]	Notes[6]
2MASX J09043699+5536025	0.037	10.4	9	X	2MASX J09043675+5535515	SDSS
ARP 151	0.021	9.6	10	X	SDSS J112535.23+542314.3	SDSS
KUG 1208+386	0.023	10	24		2MASX J12104784+3820393	SDSS
MCG +06-24-008	0.026	10.2	30		SDSS J104444.22+381032.9	SDSS
Mrk 0739E	0.03	10.4[7]	2	X	NGC 3758	SDSS
Mrk 1018	0.043	9.7	...	X	...	SDSS
Mrk 110	0.035	10	...	X	foregound star?, tidal tail	SDSS
Mrk 463E	0.05	10.6[7]	4	X	Mrk 463W	SDSS
Mrk 477	0.038	9.9	19	X	SBS 1439+537	SDSS
NGC 0835	0.013	10.5	15	X	NGC 833	SDSS
NGC 1142	0.029	10.7	17	X	SDSS J025512.06-001032.9	SDSS
NGC 5106	0.032	10.6	25	X	NGC 5100 NED01	SDSS
NGC 985	0.043	10.6	2	X	NGC 0985 NED02	SDSS
UGC 03995	0.016	10.6	9	X	UGC 03995 NOTES01	SDSS
UGC 05881	0.021	10.8	24		SDSS J104644.87+255502.1	SDSS
UGC 06527 NED03	0.026	10.5	24	X	UGC 06527 NED02	SDSS
UGC 07064	0.025	10.2	30		CGCG 158-011 NED01	SDSS
UGC 08327 NED02	0.037	10.9	35	X	UGC 08327 NED01	SDSS
2MASX J00253292+6821442	0.012	10.1	3	X	...	
2MASX J11454045-1827149	0.033	10	14	X	LEDA 867889	
2MASX J17232511+3630257	0.04	10.35	21		2MASX J17232321+3630097	
ESO 490-IG026	0.025	10.7	...	X	...	
FAIRALL 0272	0.022	10.3	19	X	FAIRALL 0271	
IRAS 05589+2828	0.033	10.4	8	X	2MASX J06021038+2828112	
M106	0.002	9.9	24		NGC 4248	
MCG +04-48-002	0.014	10.2	24		NGC 6921	
MCG -02-12-050	0.036	10.7	33	X	2MASX J04381113-1047474	
Mrk 279	0.03	10.5	27	X	MCG +12-13-024	
Mrk 348	0.015	10.3	22		2MASX J00485285+3157309	
Mrk 520	0.026	10.4	...	X	...	
NGC 235A	0.022	9.9	9	X	NGC 0235B	
NGC 2992	0.008	10.3	20	X	ARP 245N	
NGC 3227	0.004	10	10	X	NGC 3226	
NGC 3786	0.009	10	14	X	NGC 3788	
NGC 5506	0.006	10	17		SDSS J141324.11-031155.8	
NGC 6240	0.024	11[7]	0.9[8]	X	...	
NGC 7319	0.022	10	11	X	Stephan's Quintet	
NGC 7469	0.016	10.5	25		IC 5283	
NGC 931	0.017	10.6	6	X	UGC 01935 NOTES01	
UGC 11185 NED02	0.041	10.2	24	X	UGC 11185 NED01	
2MASX J04234080+0408017	0.048	10	6	X	...	Uncertain
3C 111.0	0.048	10	24		2MASX J04181911+3801368	Uncertain

.

[1]The top section includes BAT AGN in apparent mergers (18/72) that was compared to the SDSS AGN and control sample. The bottom section includes apparent mergers in the Kitt Peak sample (22/109) with spectroscopic coverage of companions only from NED.

[2]Host galaxy stellar mass based on using *ugriz* photometry and the kcorrect software of Blanton & Roweis (2007).

[3]Distance to nearest galaxy companion.

[4]Signs of disruption consistent with a merger.

[5]NED name where available.

[6]SDSS: In the SDSS spectroscopic sample, uncertain: Companion is within 2 mags of the *J*-band filter mags of BAT AGN galaxy, but has no spectroscopic redshift.

[7]Galaxy nuclei are too close to accurately separate galaxies for stellar mass.

[8]Based on a recent *Chandra* observation.
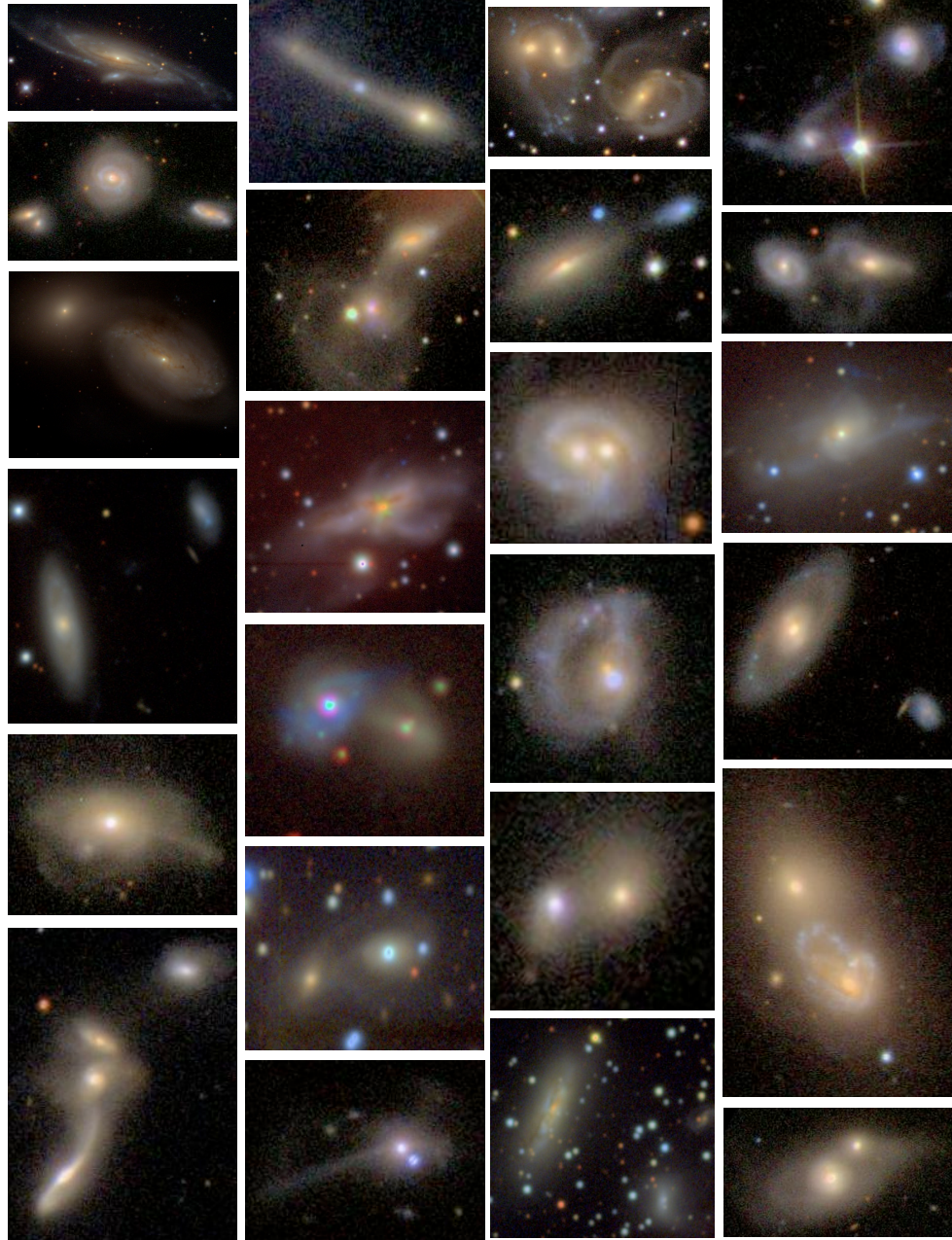
Figure 3.1: Composite *gri* images of BAT AGN hosts with disturbed morphologies or companions within 30 kpc from the SDSS and Kitt Peak. The nine galaxies were selected at random from the 40 galaxies in Table 3.3. An arcsinh stretch was used as described in Lupton et al. (2004) with intensity scaled by flux. Galaxies from left to right, first column: NGC 235A, NGC 1142, UGC 08327 NED02, Mrk 1018, ESO 490-IG026, SBS 1439+537, second column: UGC 06527, 2MASX J0904, NGC 985, Mrk 0739E, Fairall 0272, third column: NGC 7319, Arp 151, 2MASX J1145, NGC 6240, UGC 11185.

hemisphere finds a similar rate of 28% (15/53) in apparent mergers with companions within 30 kpc or in disrupted systems.

In addition, we looked for faint companions to BAT AGN in the SDSS photometric catalog with no spectroscopy. We looked specifically at the magnitude difference between the galaxy and its possible companion. Within 30 kpc we find no additional close companions within 2 mag of the host galaxy for the BAT AGN, but an additional 1% for the SDSS AGN, and 2% for the control sample. Between 2 and 3 mag, we find 4% for the BAT AGN sample, 3% for control sample, and 3% for the SDSS AGN. These faint galaxies could be at higher redshifts, and the small percentage indicates we miss only a small number of true faint companions.

We use the approach of Bell et al. (2006) for a rough estimate of the number of mergers per Gyr to assess the incidence of mergers. They estimate a typical merger timescale of 0.4 Gyr for a merger of two equal mass galaxies of radius 15 kpc that are within a distance of <30 kpc of each other. Mergers of unequal masses will tend to take longer because of reduced dynamical friction, so Bell et al.'s approach provides an upper limit on the merger rate. Following this method, the merger rate per Gyr is the percentage of galaxies in apparent mergers divided by 0.4 Gyr or about 63% per Gyr for the BAT AGN. This suggests that galaxy merging may be an important mechanism to power the AGN.

Next, we looked for the presence of companions on larger scales, between 30 kpc and 100 kpc. The cumulative distribution of nearest companion galaxies within 100 kpc can be found in Figure 3.2-left. The mean nearest neighbor galaxy separations are 41±28 kpc, 72±18 kpc, and 61±24 kpc for the BAT AGN, control galaxies, and SDSS AGN sample respectively. For galaxies with companions within 100 kpc, a Kolmogorov–Smirnov (K-S) test indicates a <5% chance that the distribution of nearest neighbor distances for the BAT AGN are from the same parent distribution
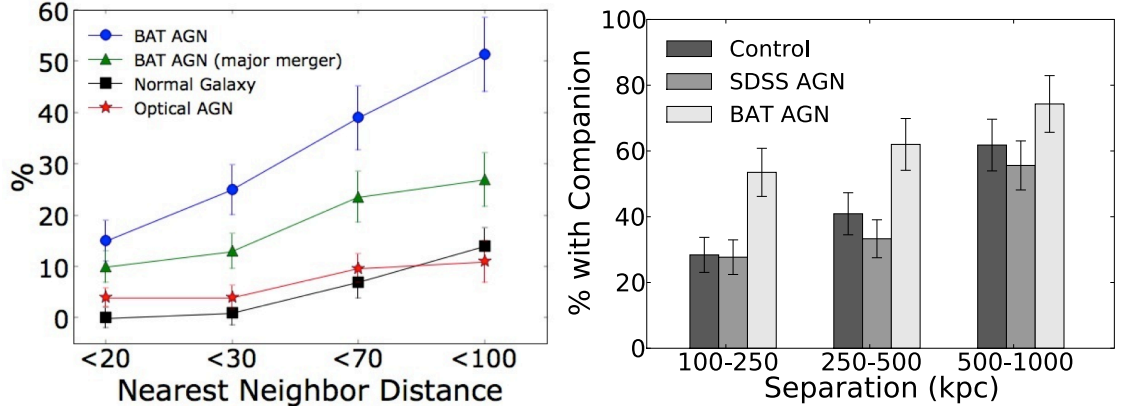
Figure 3.2: Left: cumulative distributions of BAT AGN, control galaxies, and SDSS AGN with nearest neighbors identified in the SDSS survey as a function of physical separation in kpc. The error bars assume Poisson statistics. The filled circles indicate BAT AGN with any galaxy companion. The triangle line is for AGN with a companion galaxy that has a stellar mass within a factor of 10 of the galaxy and may be considered a major merger. We find a much higher fraction of BAT AGN with close companions on scales < 100 kpc. Right: fraction of BAT AGN, control galaxies, and SDSS AGN with companions with projected physical separations of 100–1000 kpc. An excess of companions at 100–250 kpc is seen among BAT AGN.

as the control galaxies or SDSS AGN. This indicates that the BAT AGN have, on average, more and closer companions than the control or SDSS AGN galaxy on scales less than 100 kpc. We confirm that SDSS AGN and normal galaxies have similar clustering and apparent merger rates (e.g., Li et al. 2006): a Kuiper test of the SDSS AGN and control galaxies gives an 87% chance that both samples are taken from the same parent population.

We also determined the fraction of galaxies with neighbors between 100 kpc and 1 Mpc. A K-S test of the distribution of closest companions within 250 kpc yields a likelihood of <1% that the distributions of BAT AGN and control galaxies or SDSS AGN are from the same parent population. A Kuiper test indicates that there is less <5% probability that the BAT AGN companion galaxy distances are from the same parent population as the control sample or SDSS AGN. In addition, a statistically higher percentage of BAT AGN have neighbors at 100–250 kpc compared to the

control or SDSS AGN (Figure 3.2-right). All of these statistical tests indicate that the BAT AGN have closer companions than the control or SDSS AGN sample on scales less than 250 kpc.

Next, we examined the optical spectra of the BAT AGN in more detail to test whether the hard X-ray method may be selecting different types of AGN compared to the optical emission line classification. Optical fluxes were corrected for galactic extinction based on Balmer decrements and were taken from Winter et al. (2010), Ho et al. (1997a), and the Garching catalog of reduced optical spectra. The total sample includes 29 broad-line and 45 narrow-line BAT AGN. We examined the distribution of the hard X-ray to [O III] $\lambda 5007$ ratio for the non-merging and merging broad-line AGN (Figure 3.3) and found that all but one of the merging broad-line AGN, NGC 3227, are in the higher X-ray to optical ratio bin. Merging and non-merging systems have similar hard X-ray luminosity distributions so this larger X-ray to [O III] ratio in merging systems is attributed to an [O III] deficit, possibly due to unaccounted optical extinction.

In the case of narrow-line AGN, we find that merging galaxies do not have higher hard X-ray to [O III] ratios than non-merging galaxies. The mean hard X-ray to [O III] ratio is about 10 times larger for the narrow-line compared to the broad-line AGN, though, so other factors may have a stronger influence on the ratio such as the amount of narrow-line region gas, the geometry of the torus, the scattering fraction, or different levels of absorption of the hard X-ray flux for these objects. This higher hard X-ray to [O III] ratio among narrow-line AGN contradicts the AGN unification model, unless the [O III] flux is affected by orientation effects and/or is severely underestimated due to extinction.

We also looked to see if a disproportionate fraction of merging systems are missed as AGN using optical emission line diagnostics. Using the classification scheme of
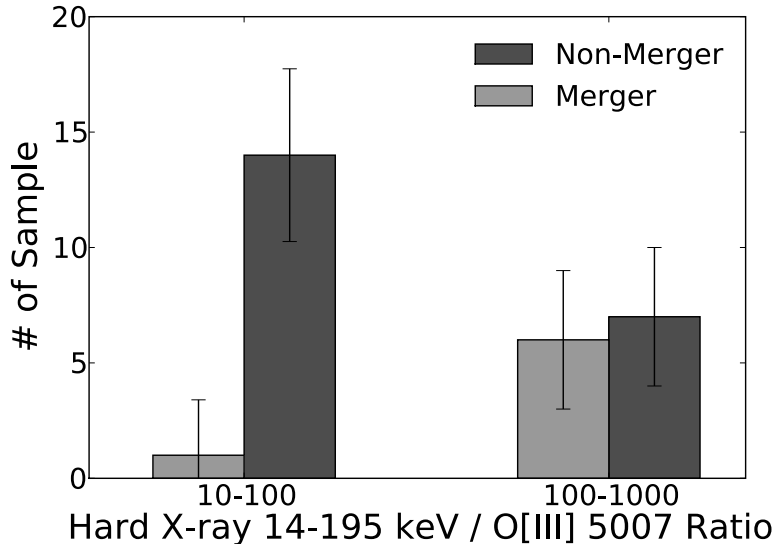
Figure 3.3: Histogram of the hard X-ray to [O III] $\lambda5007$ ratio for broad-line BAT AGN. In order to mitigate possible systematics effects associated with the different instrument configurations of the various surveys, we averaged the [O III] flux measurements from the different surveys before calculating the X-ray to [O III] ratios. A K-S test indicates a 3% chance that the distributions of non-mergers and mergers are taken from the same parent population.

Kewley et al. (2006) we find that 19% of the non-merging BAT AGN are classified as composite or HII region-line galaxies rather than AGN. In galaxies undergoing a merger we find a rate of 33%. The lower merger rate in the SDSS AGN sample may therefore be due to the fact that the optical emission-line classification is biased against mergers.

Elevated star formation activity could dilute the AGN emission, causing the AGN to be missed using optical emission line classification. We therefore investigated the *IRAS* data to see if the level of star formation in the merging systems was higher than the non-merging systems (Figure 3.4). The 60 μm is a useful tracer of strong bursts of recent star formation and is less affected by AGN emission. We define the specific star formation rate as the logarithm of the ratio of 60 μm emission to stellar mass.

The mean of the specific star formation rate for merging systems is higher
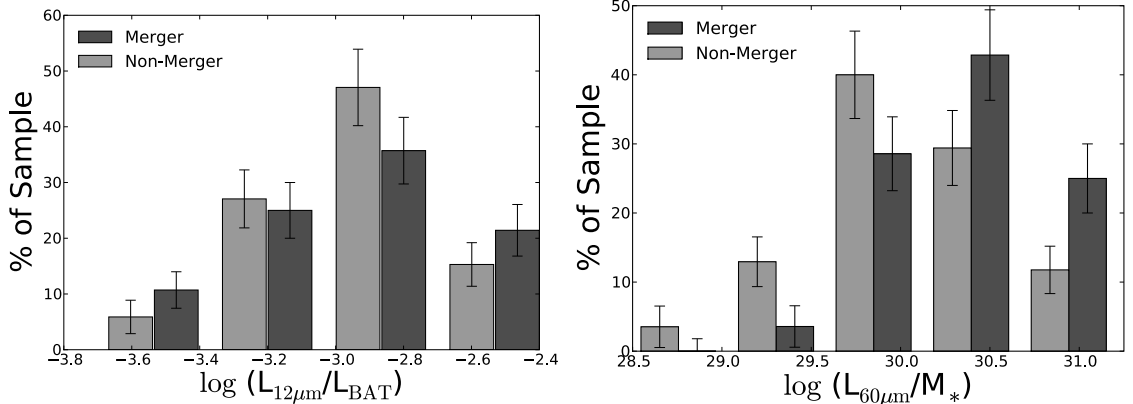
Figure 3.4: Left: histogram of the IRAS 12 μm to hard X-ray emission ratio for merging and non-merging BAT AGN. The sample includes 28 mergers and 85 non-mergers. No difference is observed between merging and non-merging systems. Most systems have $L_{12\mu m}/L_{BAT} \approx 0.1\%$, confirming the known strong correlation between the mid-IR and hard X-ray emission [e.g.,][]Vasudevan:2010p5970. Right: histogram of the logarithm of the ratio of 60 μm emission to stellar mass. This ratio is larger on average among merging systems, indicating enhanced star formation in these systems.

(30.59 ± 0.42 erg s$^{-1}M_\odot^{-1}$) than for non-merging systems (30.34 ± 0.57 erg s$^{-1}M_\odot^{-1}$) and a K-S test indicates a 2% chance that the distribution of star formation ratios for merging and non-merging galaxies are the same. A Kuiper test has a 10% chance. If we include upper limits of the *IRAS* flux a Kuiper test indicates a 7% chance. These statistical tests indicate enhanced star formation activity in merging systems compared to non-merging systems.

To further investigate the possibility that BAT AGN are found in galaxies with higher merger rates than average, we looked at the level of star formation activity based on the *IRAS* 60 μm emission in BAT AGN compared to normal galaxies in the control sample and redshift-matched SDSS AGN. A larger fraction of the BAT AGN (61%) are detected at 60 μm than normal galaxies in the control (14%) and SDSS AGN (11%). We also find that 18% of the BAT AGN are luminous infrared galaxies (LIRGS;$L_{IR} > 10^{11}L_\odot$) and only 3% of the control galaxies and 1% SDSS AGN are LIRGs. These results indicate that BAT AGN have elevated star formation

activity relative to normal galaxies and SDSS AGN (AGN contamination to the 60 μm emission in LIRGs is negligible; (Petric et al. submitted).

3.4   Summary and Discussion

We find a larger fraction of BAT AGN with disturbed morphologies or in close physical pairs ($<$30 kpc) compared to matched control galaxies or optically selected AGN. The high rate of apparent mergers (25%) suggests that AGN activity and merging are critically linked for the moderate luminosity AGN in the BAT sample. We also investigated why this merging rate is larger than in optical AGN samples. We find that merging broad-line AGN galaxies are preferentially found in galaxies with high hard X-ray to [O III] λ5007 ratios. We also find a higher specific star formation rate in merging systems in the BAT sample. This suggests that these merging AGN may not be identified using optical emission line diagnostics because of optical extinction and dilution by star formation. Additional support for this picture comes, for instance, from Goulding & Alexander (2009) who found that optical emission line classification may be missing 50% of local AGN identified via mid-infrared spectroscopy with *Spitzer*. This also seems to be the case at slightly higher redshifts and luminosities among ULIRGs ($L_{IR} > 10^{12} L_{\odot}$; Veilleux et al. 2009b).

Chapter 4

Detection of a Binary AGN in Mrk 739 using *Chandra*

4.1 Introduction

In the previous chapter we found that the merger rate of BAT AGN host galaxies is much than higher normal galaxies suggesting an association between AGN activity and galaxy mergers. If galaxy mergers are the prime way to 'ignite' the central source by sending a large amount of gas into the center region and triggering the AGN (di Matteo et al. 2005), then we expect some fraction of these binary black holes to be actively growing simultaneously, thus creating a binary AGN. Thus, the detection and frequency of binary AGN is important since it provides constraints on models of galaxy formation and a critical test of the merger-driven AGN model. We had also found in chapter 3 that AGN selected using optical emission line diagnostics preferentially fail to detect merging BAT AGN. We therefore hypothesized that the fraction of binary or double AGN systems may be much higher than optical emission line surveys suggest and proposed time using the high spatial resolution of *Chandra*

($\approx 0.5''$). The use of *Chandra* was critical, since in most of these objects, the angular resolution of the *Swift* XRT or *XMM-Newton* is unable to determine the presence of multiple nuclei for separations $<10''$ in equal luminosity sources or $<15''$ if the secondary X-ray source is faint.

Despite their theoretical importance, only a handful of close binary AGN (<5 kpc projected separation) have been discovered. The two clearest cases are the *Chandra*-detected double nucleus in the luminous infrared galaxy (LIRG; $L_{IR}>10^{11}L_\odot$) NGC 6240 (Komossa et al. 2003) with a projected separation of 1 kpc at a distance of 103 Mpc and the LIRG Mrk 463 at 3.8 kpc separation and a distance of 220 Mpc. Recently some likely binary AGN have been discovered based on double-peaked [O III] λ5007 emission lines (Liu et al. 2010). However, there is still some question whether these systems are 'true' binary AGN or are a single AGN with an asymmetric distribution of outflowing gas in the narrow line region (Fischer et al. 2011; Smith et al. 2010). Unfortunately, these systems are at higher redshifts with extremely close separations where the resolution of *Chandra* is unable to resolve these objects to confirm their binary AGN nature.

In this chapter we focus on a single binary AGN in the BAT sample, Mrk 739, which is important because of its extremely close 3.4 kpc separation and because it shows no evidence of being an AGN in the optical, UV, or radio. This suggests that binary AGN may be more common than surveys at other wavelengths suggest. Other than NGC 6240, it stands as the nearest case of a binary AGN discovered to date.

4.2 Observations and Data Analysis

In the following subsections, we describe the observations and analysis of Mrk 739. Throughout this work, we adopt $\Omega_m = 0.3$, $\Omega_\Lambda = 0.7$, and $H_0 = 70$ km s^{-1} Mpc^{-1} to determine distances. At the redshift of Mrk 739, $1''$ corresponds to 580 pc.

4.2.1 Optical: SDSS Imaging and Gemini Optical Spectroscopy

Mrk 739 was imaged by the SDSS on March 10, 2005. Using a Sérsic profile with a fixed bulge ($n=4$), we fit the optical nuclei using two-dimensional surface brightness fitting (GALFIT; Peng et al. 2002). In Mrk 739E, a point source component was used to measure the AGN light since it has a broad line region (BLR).

We observed Mrk 739 with Gemini on February 7, 2011. Both nuclei were observed simultaneously in the B600-G5307 grating with a $1''$ slit in the 4300–7300 Å wavelength range. The exposure totaled 37 minutes. We follow Winter et al. (2010) for correcting Milky Way reddening, starlight continuum subtraction, and fitting AGN diagnostic lines. To correct our line ratios for extinction, we use the narrow Balmer line ratio (Hα/Hβ) assuming an intrinsic ratio of 3.1 and the Cardelli et al. (1989) reddening curve.

4.2.2 UV and Radio: $XMM - Newton$ and VLA

Mrk 739 was observed in the UV with $XMM - Newton$ in June 2009 (PI Brandt, Vasudevan in prep.). We follow the XMM ABC guide for photometry. We also analyzed archival VLA observations with times of 33 minutes at 1.49 GHz and 38 minutes at 4.86 GHz.

4.2.3   X-rays: *Chandra*

Chandra observed Mrk 739 on April 22, 2011 with an exposure time totaling 13 ks. Sub pixel event repositioning was applied to improve the resolution of the image. Two extraction regions of $1.5''$ radius were used for spectral fitting and timing analysis with CIAO version 4.3. To fit the X-ray spectra, we used a fixed Galactic photoelectric absorption (Kalberla et al. 2005), a floating photoelectric absorption component at z=0.0297, and a power law. For the eastern source (Mrk 739E), we also include a pileup model because mild pileup (10%–20%) is expected based on pixel count rates.

4.2.4   Submillimeter: CO Observations

The ^{12}CO (2–1) and (3–2) molecular lines of Mrk 739 were observed with the James Clerk Maxwell Telescope (JCMT) on March 12–13, 2011. The A3 (211-279 GHz) and HARP (325-375 GHz) receivers were used. The spectra were co-added, binned, and fitted with linear baselines. To calculate velocity-integrated line flux densities, we assumed an aperture efficiency of 0.60 and 0.53 for the A3 and HARP receiver and followed Greve et al. (2009).

4.3   Results

4.3.1   Optical Properties of Mrk 739

Two hard X-ray point sources coincide with the best fit model of the optical light from the bulge components (Figure 4.1). The bulge magnitudes are m_r=14.03±0.15 for Mrk 739E and m_r=13.75±0.15 for Mrk 739W. The small difference in apparent magnitudes suggests a major merger between the two galaxies.
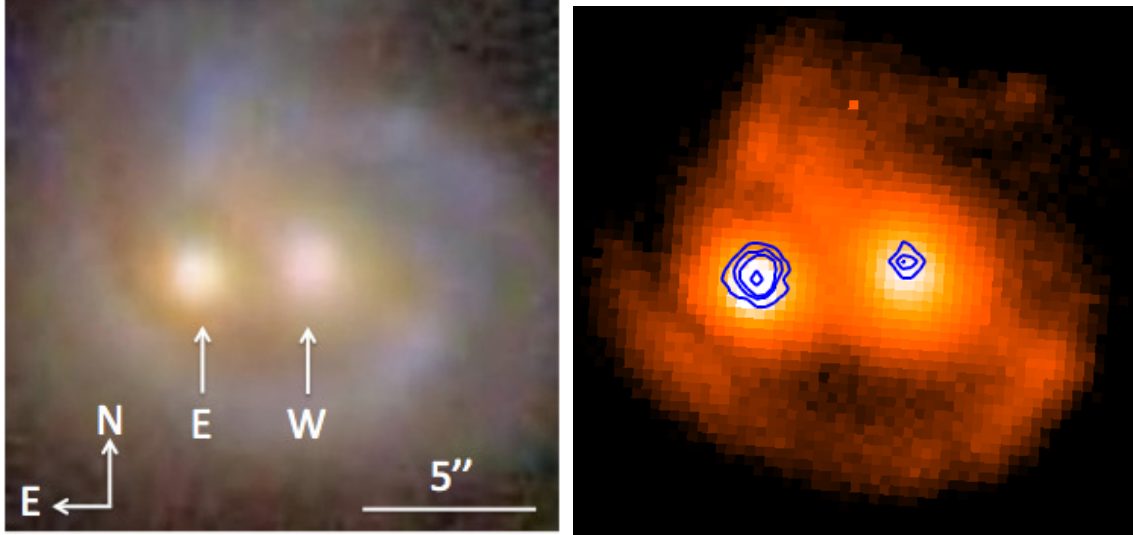
Figure 4.1: **Left**: composite SDSS *gri* filter image of Mrk 739. **Right**: SDSS *r*-band image overlaid with contours from *Chandra* (blue) at same scale. The X-ray sources are coincident with the bulge components seen in the optical for Mrk 739E and Mrk 739W.

The optical spectra for both sources are shown in Figure 4.2. Mrk 739E shows broad lines (FWHM Hβ=2960 km s^{-1} and Hα=2120 km s^{-1}) consistent with a Seyfert 1. Mrk 739E also has strong [Fe VII] 5721 and 6087 $\mathring{A}$ emission, a feature of some Seyfert 1 galaxies indicative of highly ionized material near the central AGN (e.g., Veilleux 1988). In Mrk 739W, there are narrow lines at the spectral resolution of instrument (FWHM=280 km s^{-1}). Based on the Balmer decrement, $E(B-V)$=0.26 for Mrk 739E and $E(B-V)$=0.43 for Mrk 739W. Mrk 739W is classified as a starburst using the [OI]/Hα and [SII]/Hα line diagnostics and a composite galaxy using the [NII]/Hα diagnostic (Kewley et al. 2006). Assuming that all of the Hα luminosity is from star formation and using Kennicutt (1998), the estimated star formation rate (SFR)=0.3 $M_\odot$ yr^{-1}.
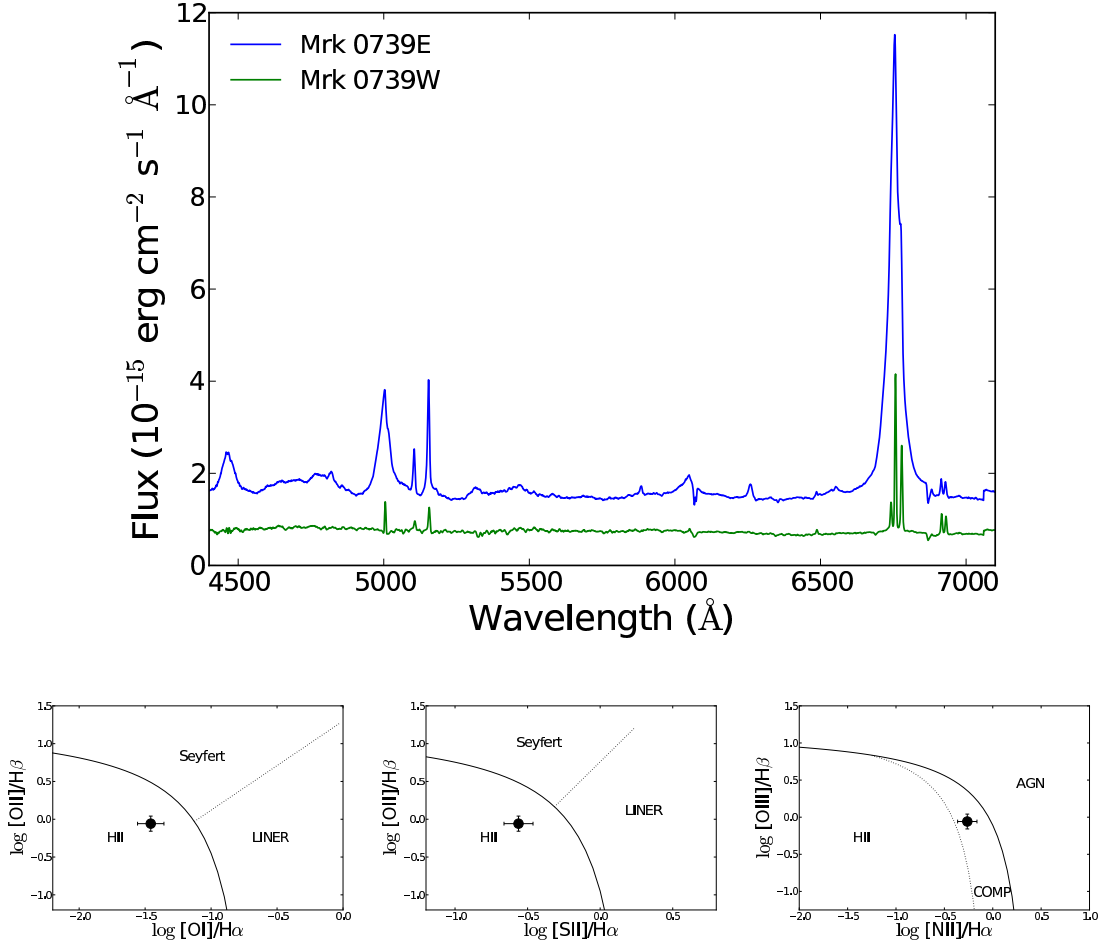
Figure 4.2: **Upper panel**: optical spectra of Mrk 739E and Mrk 739W. **Lower panel**: emission line ratios of Mrk 739W, the narrow line source discovered to be an AGN in X-rays. Mrk 739W is consistent with star formation in the [OI]/Hα and [SII]/Hα diagnostics and a composite galaxy in the [NII]/Hα diagnostic.

4.3.2 UV, Far-Infrared, and Radio

The UV image from $XMM - Newton$ Optical Monitor shows sources coincident with the hard X-ray sources (Figure 4.3). In the UV, m_{UVW1}=15.4±0.1 and m_{UVM2}=16.6±0.1 for Mrk 739E and m_{UVW1}=16.6±0.1 and m_{UVM2}=16.4±0.1 for Mrk 739W. The spectral index connecting 2500Å and 2 keV, α_{OX}, is -1.10±0.04 for Mrk 739E, typical of an AGN (-1.15±0.24; Steffen et al. 2006). In Mrk 739W, α_{OX}=-1.53±0.1, sug-

71

gesting the UV is dominated by star formation. Assuming all the UV emission in Mrk 739W is from star formation and following Kennicutt (1998), we estimate SFR=0.6 $M_\odot$ yr^{-1}.

Mrk 739 was detected in all bands by IRAS. The measured luminosity is log $L_{\odot,\mathrm{IR}}$=10.9 and log $L_{\odot,\mathrm{FIR}}$=10.6. Following the Kennicutt (1998) relationship between far-infrared (FIR) luminosity and star formation rate, we estimate SFR=6.9 $M_\odot$ yr^{-1}.

Mrk 739E was detected at both 1.49 and 4.86 GHz (Figure 3), with a flux density of 2.6±0.2 mJy at 1.49 GHz and 0.5±0.2 at 4.86 GHz (after convolving to match the 1.49 GHz resolution). This is a spectral index ($S_\nu = K \times \nu^{-\alpha}$) of α =1.2±0.5.

The VLA data for Mrk 739W are consistent with resolved star formation and show no signs of an AGN. The emission at 1.49 GHz has an integrated flux density of 2.6±0.2 mJy. The 4.86 GHz convolved data also shows resolved emission with an integrated flux density of 1.3±0.3 mJy. The spectral index for Mrk 739W is $\alpha = 0.8$±0.3, consistent with optically thin synchrotron emission from supernovae found in star forming galaxies. We use Yun et al. (2001) to convert the 1.49 GHz luminosity of Mrk 739W to a SFR of 3.1 $M_\odot$ yr^{-1}.

4.3.3 X-ray

We detect two hard X-ray sources coincident with the eastern optical nucleus (Mrk 739E) and western nucleus (Mrk 739W). Both sources show hard X-ray spectra extending out to 10 keV (Figure 4.4). In the 2–10 keV band, we find a FWHM of $0.48'' \pm 0.05$ (280 pc) for Mrk 739E and $0.51'' \pm 0.07$ (295 pc) for Mrk 739W. The *Chandra* spectra of Mrk 739E is well fit (χ^2_ν=1.4) by a power law ($F \propto E^{-\Gamma+2}$) with photon index $\Gamma = 2.1 \pm 0.1$ and $N_\mathrm{H} = 1.5 \pm 0.2 \times 10^{21}$ cm^{-2} consistent with a Seyfert 1. Mrk 739W is well fit (C-stat/dof=0.8) by a harder power law with more absorption and a photon index $\Gamma = 1.0 \pm 0.2$ and $N_\mathrm{H} = 4.6 \pm 0.1 \times 10^{21}$ cm^{-2}. While positive
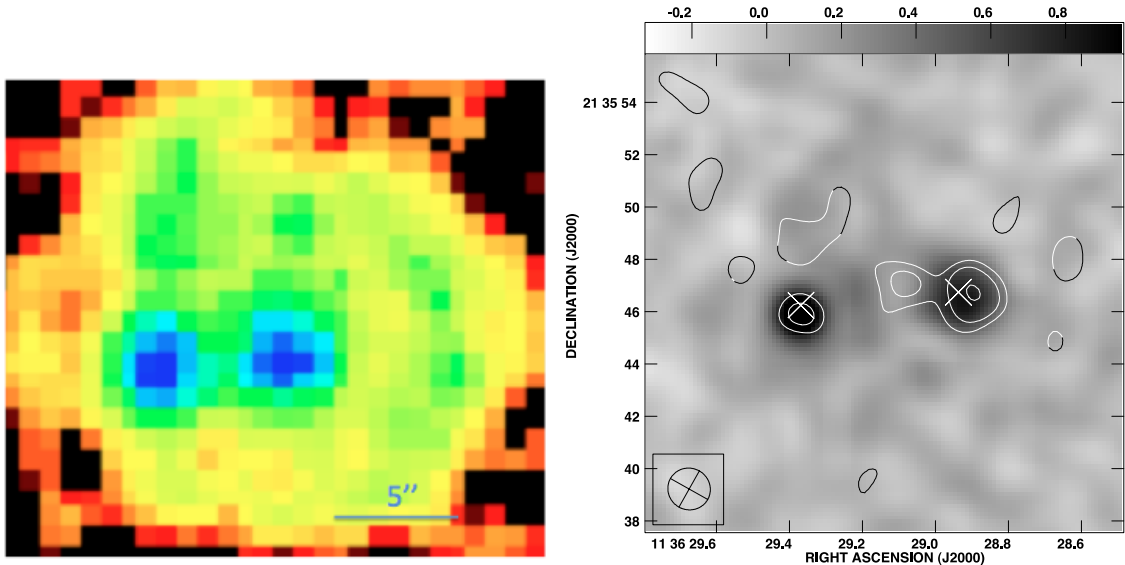
Figure 4.3: **Left**: $XMM-Newton$ UVM2 image of Mrk 739. **Right**: the grey-scale image is the 1.49 GHz VLA data, while the contours are the 4.86 GHz data convolved to 1.49 GHz beam. White ×'s indicate the $Chandra$ hard X-ray positions. Both the UV and radio data in Mrk 739W show extended emission consistent with star formation.

residuals do exist at the location of the neutral 6.4 keV iron Kα line in Mrk 739W, there are too few counts to confirm its existence. The 2–10 keV absorption-corrected luminosities are $L_{2-10\,\mathrm{keV}} = 1.1\times10^{43}$ and 1.0×10^{42} erg s^{-1} for Mrk 739E and Mrk 739W, respectively. An archival $XMM-Newton$ 2009 observation of Mrk 739 is unable to resolve the emission to either source, but shows $L_{2-10\,\mathrm{keV}}{=}1.0\times10^{43}$ and $\Gamma = 1.92 \pm 0.02$ consistent with the $Chandra$ spectra of Mrk 0739E.

Timing analysis is a critical part of identifying AGN since nearly all show variability. Bins of 1.5 ks were chosen to ensure >20 counts per bin (Figure 4). We find statistically significant variations in the fluxes of both sources. There is a factor of 2.5 change in flux for Mrk 739W and 0.3 for Mrk 739E during the ≈4-hour observation.

Mrk 739 was detected by $Swift$ BAT with $L_{14-195\,\mathrm{keV}}{=}2.4{\pm}0.5 \times 10^{43}$ erg s^{-1}, $\Gamma{=}2.6{\pm}0.4$, and a factor of two variability over five years (Figure 4). Because of the
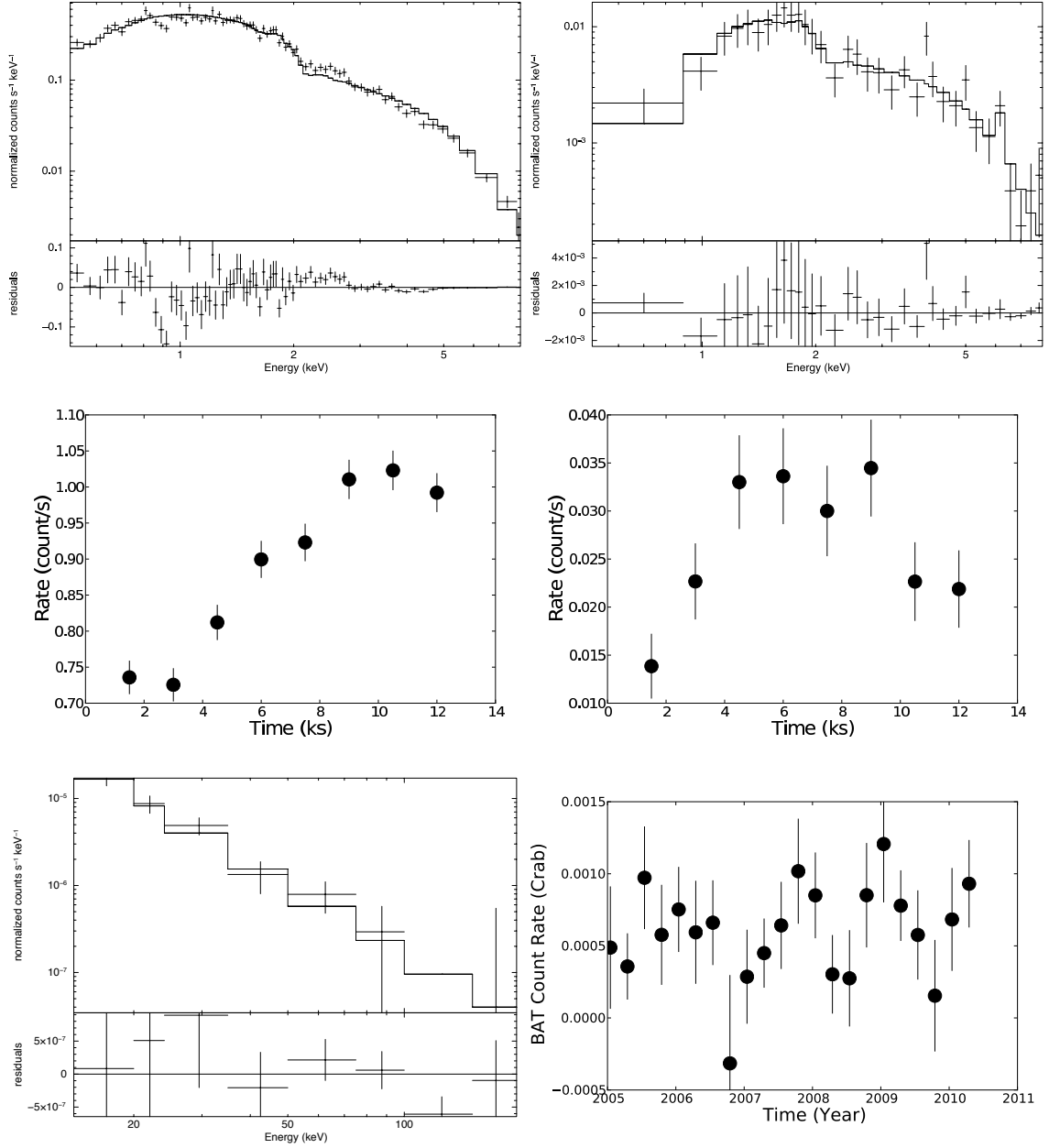
Figure 4.4: **Upper panel**: *Chandra* spectra of Mrk 739E (left) Mrk 739W (right).
Middle panel: *Chandra* count rate in 1.5 ks bins for Mrk 739E (left) Mrk 739W
(right). There is a factor of 2.5 variability in flux over the 4-hour observation of
Mrk 739W. **Lower panel**: *Swift* BAT spectra (left) and average count rate in 3
month bins (right) for Mrk 739.

variability and much steeper photon index of Mrk 739W, it is difficult to identify
the source of the $L_{14-195\,\mathrm{keV}}$ luminosity (Mrk 739E, Mrk 739W, or both).

4.3.4 Detection of a Binary AGN

The hard X-ray (>2 keV) band provides one of the best tools for finding AGN since it is less affected by contamination and absorption and can only be produced in large amounts by AGN. Our discussion of this binary AGN will be limited to Mrk 739W since Mrk 739E was already known to be an AGN based on its BLR (Netzer et al. 1987).

In Mrk 739W, the hard X-ray emission is point-like at the location of one of the bulge components in the galaxy consistent with an AGN. Energetic phenomena related to vigorous star formation such as OB stars, X-ray binaries, and SN shocks produce hard X-rays. However, in star forming regions the dominant X-ray emission is from point-like ultraluminous X-ray sources (ULXs; Bertram et al. 2007). ULXs are by definition not located at the centers of galaxies where the central supermassive black hole resides.

The luminous hard X-ray emission, hard photon index, and time variability of Mrk 739W also provide little support for the hypothesis that this source is a ULX. In a study of 154 ULXs, the average luminosity is much lower ($L_{0.5-8\,\mathrm{keV}} = 2.2 \pm 4.5 \times 10^{39}$ erg s^{-1}). The most luminous ULX ever detected, ESO 243-49 HLX-1 (Farrell et al. 2009), has a 0.2–10 keV luminosity of 10^{42} erg s^{-1}, however, its hard X-ray (2–10 keV) luminosity is only 4×10^{40} erg s^{-1} because it has a soft photon index of 3.4. Therefore, if Mrk 739W is a ULX, it is the most luminous ULX in the hard X-rays ($L_{2-10\,\mathrm{keV}}$) by over an order of magnitude. The average ULX power law index is also $\Gamma=1.97\pm0.11$, which is significantly softer than Mrk 739W ($\Gamma=1.0 \pm 0.2$). Finally, no ULXs have shown such high amplitude variability over the short timescale of hours with this level of variability only seen on time scales of days to weeks (Gladstone 2010).

The measured SFRs in Mrk 739W provide an additional constraint as to whether the hard X-ray emission could be from star formation. A SFR greater than 200 $M_\odot$ yr^{-1} would be required to generate the observed hard X-ray luminosity based on the relationship between SFR and X-ray emission (Ranalli et al. 2003). The predicted SFR in Mrk 739W is 0.3, 0.6, and 3.1 $M_\odot$ yr^{-1} from the Hα, UV luminosity, and 1.4 GHz emission. The predicted SFR from FIR emission of the combined system is 6.9 $M_\odot$ yr^{-1}. All of these rates are significantly lower than the 200 $M_\odot$ yr^{-1} needed to generate the observed hard X-ray luminosity. In addition, it is likely that much of this star formation would be extended and resolved in *Chandra*.

It is interesting that Mrk 739W has not been detected as an AGN using optical emission line spectroscopy. Noguchi et al. (2010) found that optical emission line studies are biased against 'buried AGN' that have a small scattering fraction or a small amount of narrow line region gas. AGN with a low ratio of [O III] to hard X-ray luminosity ($L_{[OIII]}/L_{2-10\,keV}$ <0.1) tend to be 'buried AGN'. The $L_{[OIII]}/L_{2-10\,keV}$=0.008 of Mrk 739W is consistent with a 'buried AGN' and the lowest ratios found in their study. This finding is also consistent with a recent study that found that merging AGN selected in the ultra hard X-rays tend to have low $L_{[OIII]}/L_{14-195\,keV}$ ratios and be preferentially misclassified using optical line diagnostics (Koss et al. 2010).

For AGN with low luminosity in the [O III] line, nebular emission from star formation can overwhelm the AGN signature in optical emission line diagnostics. Schawinski et al. (2010) found that for $L_{[OIII]}=10^{40}$ erg s^{-1}, nearly 54% of star forming galaxies with AGN will be classified as star forming or composites. The small value of $L_{[OIII]}=7.5 \times 10^{39}$ erg s^{-1} in Mrk 739W suggests that star formation is overwhelming the AGN photoionization signature.

4.3.5 CO Properties and Molecular Gas Mass

CO velocity profiles can provide information on the dynamics of the molecular gas. The ^{12}CO 3–2 and 2–1 spectra in Mrk 739 have almost identical shapes. Each spectrum has a narrow profile with FWHM=94±8 and 98±6 km s^{-1} for single-Gaussian fits to the CO (2–1) and CO (3–2) profiles, respectively. These profiles are significantly narrower than the CO (2–1) emission from NGC 6240 (Figure 4.5) and imply a nearly face-on orientation to any disk-like structure in this system.

CO measurements also provide estimates of the amount of molecular gas. In Mrk 739, I_{CO}=109±33 and 169±51 Jy km s^{-1} for the 2–1 and 3–2 lines. Following Solomon et al. (1992), L'_{CO}=10.9×10^8 and 7.5×10^8 K km s^{-1} pc^{-2} for the 2–1 and 3–2 lines. Adopting α=1.5-4 $M_\odot$ (K km pc^{-2})$^{-1}$ for the conversion from CO luminosity to molecular hydrogen, we find log $M_\odot(H_2)$=9.2-9.6, similar to the Milky Way (Sanders et al. 1984).

4.3.6 Relative Velocity of the Binary AGN

Measurements of radial velocities provide important insights about the dynamics of the merger. We use the Na I $\lambda\lambda$ 5890, 5896 (Na D) absorption lines from stars and cold gas since narrow emission lines in AGN often have blueshifts (Bertram et al. 2007). There is an offset of $\approx$40 km s^{-1} between the two bulge components (8995±15 km s^{-1} for Mrk 739E and 8953±15 km s^{-1} for Mrk 739W). The CO data also show evidence of two components with the peak brightness temperatures similar to the radial velocities in the Na D absorption lines (Figure 4.5). When fit with gaussians, the peaks consistent with the Na D radial velocities (8921±22 and 8980±16 km s^{-1} in CO 2–1 and 8956±12 and 8993±22 km s^{-1}). High resolution (1$''$) interferometric CO imaging of this system would provide evidence to confirm this picture.
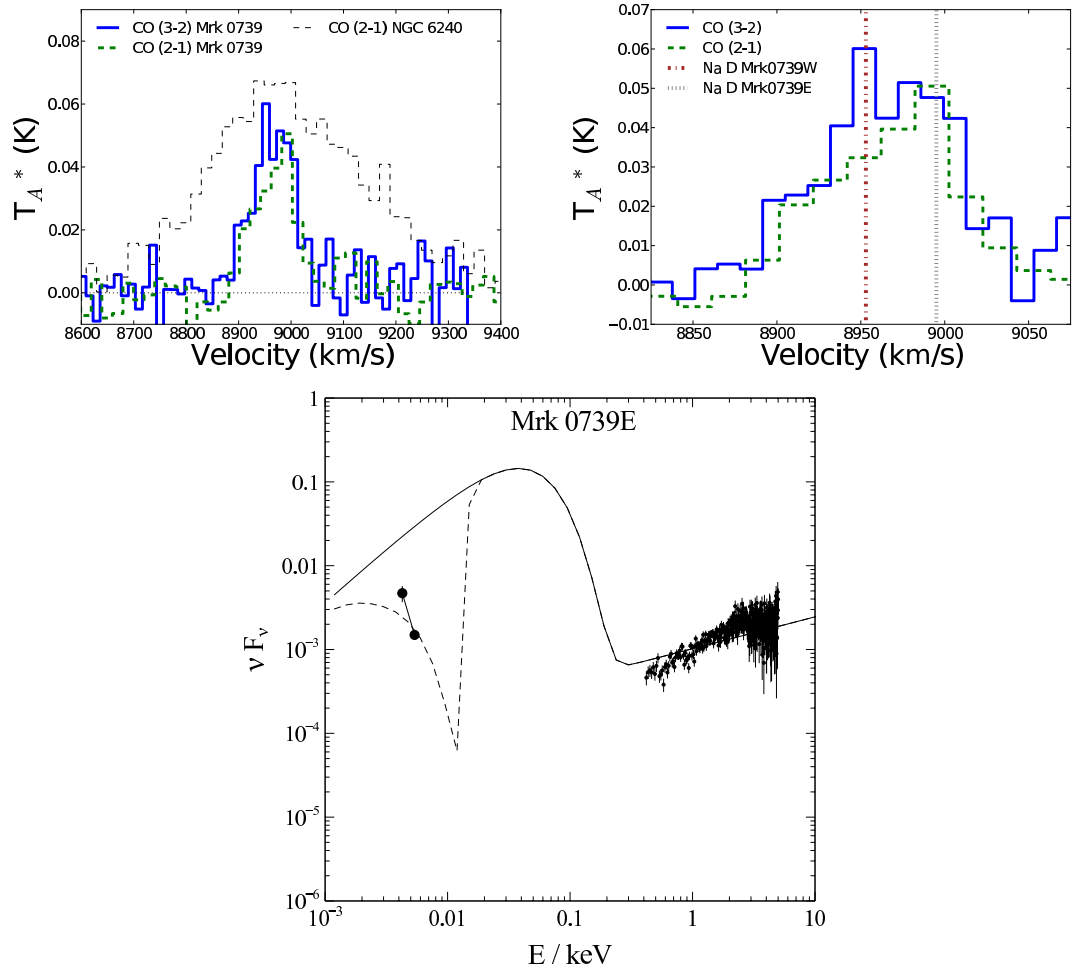
Figure 4.5: **Upper left**: CO observation of Mrk 739 with an observation of NGC 6240 overlaid for comparison. The brightness temperature of NGC 6240 is reduced by 0.63 to account for the increased distance of Mrk 739 (Solomon et al. 1992). **Upper right**: CO observation with radial velocities of the Na D absorption lines from the optical spectra. **Lower**: measured UV and X-ray emission for Mrk 739E. The extinction-corrected SED model is shown as a solid line and the dashed line indicates the fit to the observed data.

There is also evidence of outflows in the narrow line region of Mrk 739E. There is a 192±22 km s^{-1} blueshift in the [O III] line and a 153±25 km s^{-1} in the lower ionization [O I] λ 6300 line compared to the Na D absorption. This blueshift is consistent with other nearby QSOs which have an average [O III] blueshift of -174 km s^{-1} (Bertram et al. 2007). In Mrk 739W, there is no evidence of outflows in the narrow line region.

4.3.7 Bolometric Luminosity and Eddington Ratios

Using *Chandra* and UV photometry and following Vasudevan et al. (2009), the bolometric luminosity is 1.0×10^{45} erg s^{-1} in Mrk 0739E (Figure 5). The extinction corrected 2500 $\mathring{A}$ luminosity is $\log L_{2500\mathring{A}} = 43.7 \pm 0.3$. Using H$\beta$ and continuum emission (Vestergaard & Peterson 2006), the black hole mass is $\log M_{BH}$=7.04±0.4 $M_\odot$, giving an Eddington ratio of λ_{Edd}=0.71, the highest amongst all the *Swift* BAT selected AGN (Vasudevan et al. 2010). Our estimates are consistent with Ho et al. (2008) who find λ_{Edd}=0.78 using only optical spectra and the same method to determine black hole mass. Uncertainties in intrinsic dust reddening, as well as the inclination angle and spectral hardening parameter in the accretion disk model can lower the Eddington ratio at most 58% to λ_{Edd}=0.30.

In Mrk 739W, the bolometric luminosity is 2×10^{43} erg s^{-1} using only the hard X-ray data with a bolometric correction factor of 22 from Vasudevan et al. (2009).

4.4 Discussion

We discovered a binary AGN in the galaxy Mrk 739 based on *Chandra* imaging showing two unresolved (FWHM≈300 pc) luminous hard X-ray sources with a projected separation of 3.4 kpc (5.8±0.1″). We find that a high level of star formation

combined with a very low $L_{[OIII]}/L_{2-10\,keV}$ ratio cause the AGN to be missed in optical spectroscopy. In the radio, there is resolved emission with a spectral index consistent with star formation. The CO observations of the (3–2) and (2–1) lines indicate large amounts of molecular gas in the system. This gas could be driven towards the black holes during the violent galaxy collision and be key to fueling the binary AGN. In Mrk 739E, there is a high Eddington ratio ($\lambda_{Edd}=0.71$) and small black hole ($\log M_{BH} = 7.05\pm0.3$) consistent with an AGN accreting at a high accretion rate. Other than NGC 6240, this stands as the clearest and nearest case of a binary AGN discovered to date.

Mrk 739 is an important example of how critical high resolution ($< 1''$), hard X-ray (>2 keV) imaging is in finding binary AGN (< 5 kpc). Observations with *Chandra* provide one of the most effective tools since obscuration and/or contamination from merger induced star formation can hide the AGN at other wavelengths. Mrk 739W showed no evidence for hosting an AGN until the *Chandra* observation despite a host of previous observations including UV and optical spectroscopy, and radio data from the VLA. While mega surveys such as the SDSS, 2dF, and 6dF are finding valuable information on hundreds of thousands of AGN using optical emission line diagnostics, this technique can be biased against finding AGN in objects that have high levels of star formation or obscuration like mergers (see also chapter 3, Goulding & Alexander 2009; Veilleux et al. 2009a).

The three nearest binary AGN (NGC 6240, Mrk 739, Mrk 463) discovered to date with *Chandra* share many properties which may hold clues as to why they form. A surprising result is that all three are luminous in the ultra hard X-rays and detected in the *Swift* BAT all sky survey ($\log L_{14-195\,keV} > 43.4$ erg s^{-1}). This suggests that binary AGN happen more often in systems with bright X-ray AGN. More X-ray follow-up work needs to be done with less luminous merging systems to

confirm this result. The large FIR (60 and 100 μm) luminosities (log $L_{\odot,\mathrm{FIR}}$=11.5, 11.1, and 10.6 for NGC 6240, Mrk 463, and Mrk 739) suggest that these systems may be linked to gas-rich progenitor galaxies consistent with theoretical models (Yu et al. 2011, submitted).

Chapter 5

Instrumentation Development in the Ultra Hard X-rays: The InFOCμS Balloon Mission

5.1 Introduction

The first part of the thesis focused on observational studies of nearby AGN using the ultra hard X-rays and now I change the discussion to the development of new focusing optics at this wavelength. Because of the difficulty of focusing energetic ultra hard X-rays, instruments like $Swift$ BAT used a coded aperture mask of lead tiles to use a shadow pattern to detect sources. In a coded aperture, images from multiple apertures overlap and it is necessary to use a complex algorithm to reconstruct the original image. The image is formed from the whole array of sensors and therefore accepts much more background radiation than in focusing optics. Thus, for equal collecting areas, the sensitivity of a focusing instrument is always better for single point sources. In $Swift$ BAT, the coded aperture provides

a positional accuracy of $\approx 5'$ for bright sources. This sometimes leads to source confusion and requires lower energy X-ray followup (<10 keV) to determine the exact source. Focusing optics could provide a much higher sub-arcminute resolution with better sensitivity than $Swift$ BAT. In addition, because of increased sensitivity, variable emission can be studied on much shorter time scales.

The InFOCμS ultra hard X-ray balloon telescope (Figure 5.1) was designed to extend the focusing optics beyond the limit of current X-ray satellites at 10 keV using multilayer mirrors and a long 8m baseline. The InFOCμS balloon last flew in September, 2004, capturing some of the first ultra hard X-ray images using focusing optics and was scheduled to fly in 2008 or 2009 from Australia. As part of this effort, I spent a year working on the instrumentation for the balloon launch with 6 months in Nagoya, Japan working with collaborators on the project under a science grant from the Japanese Society for the Promotion of Science. Unfortunately, because of NASA funding issues, the balloon has not yet launched. However, the launch of a new hard X-ray imaging satellite, $NuSTAR$, in 2012, holds much promise for furthering our understanding of AGN by imaging them at high redshift where the bulk of black hole growth is occurring. Therefore, the discussion of this new imaging instrumentation in this chapter is important. In the following, I detail my instrumentation work for this balloon project which focused on the star cameras.

5.2 The Importance of Focusing Optics in the Ultra Hard X-rays

Focusing optics in the ultra hard X-rays allow a revolutionizing leap ahead in imaging sensitivity and spatial resolution compared to the current coded aperture mask and collimator technologies deployed in satellites like $BeppoSAX$, $Swift$ BAT, $Integral$,

Figure 5.1: Image of the InFOCμS Gondola.

and *Suzaku*. This will greatly improve our understanding of nonthermal processes in astrophysics such as particle acceleration processes in the same way that grazing incident telescopes, that focus softer X-rays, revolutionized our understanding of thermal processes with the systematic mapping of galaxies, clusters of galaxies, and supernovae remnants.

Currently, the best data for the hard cosmic X-ray background is obtained by satellites using collimator or coded aperture mask technologies, but these technologies are unable to resolve the majority of sources producing this flux ($\approx 98\%$ unresolved, Ajello et al. 2008). This has led to the prediction of a large population of obscured high redshift AGN creating the X-ray background. Only a ultra hard X-ray telescope with focusing optics could provide the sensitivity to resolve the point sources contributing to this flux. In addition, in the dense galactic center where the dense gas and dust can't be penetrated by softer energies, there are so many sources, that *Swift* BAT and *Integral* suffer from source confusion. Ultra hard X-ray focusing optics will provide the resolution to resolve the individual Galactic sources such as neutron stars or black hole candidates that are producing this energy.

Multilayer mirrors enable focusing optics to go beyond the 10 keV energy limit
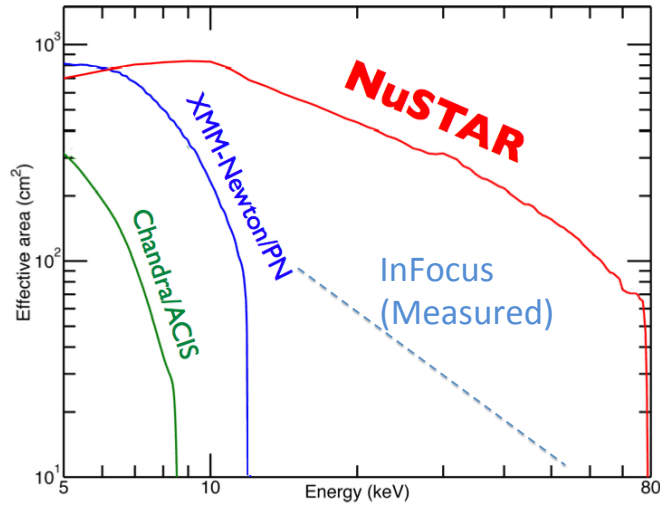
Figure 5.2: Plot of effective area with energy in keV. Multilayer mirrors such as used in InFOCμS and $NuSTAR$ enable focusing optics to go beyond the 10 keV energy limit of grazing incidence optics employed in soft X-ray imaging instruments.

of grazing incidence optics employed in soft X-ray imaging instruments such as $Swift$ XRT, $Chandra$, and XMM (Figure 5.2). With the use of multilayer mirrors, the reflection is through Bragg reflection, and the limiting angle of reflection is increased up to much higher energies of 10-80 keV. The ultra hard X-ray regime is also dominated by noise from high-energy cosmic rays hitting the instrument and the Earths atmosphere, so sensitivity is critical. With focusing optics, systematic errors can be significantly reduced since the background from cosmic diffuse emission is related to area, and this will be reduced in focusing, dramatically increasing signal to noise.

5.3 The InFOCμS mission

Balloon telescopes in the upper atmosphere are a critical way to perform scientific observations at a fraction of the cost and time of deploying satellites. At about 40 km, ultra hard X-rays (> 20 keV) are not completely absorbed by the atmosphere. Balloon flights are also particularly relevant since hard X-ray focusing optics have not yet been deployed in satellites and the balloon platform allows a very long baseline for focusing without the complication of folding the telescope into a rocket shroud. Balloon instruments also offer an important test bed for the future deployment on satellites.

The InFOCμS balloon mission is a joint collaboration between the United States and Japan. Nagoya University is contributing the work on the telescope such as fabricating and applying multilayer mirrors and the star camera for performing fine pointing measurements. NASA Goddard is contributing the focal plane detector, telescope gondola, inertial navigation sensor, rough sensor systems, and overall system integration.

5.4 Star Camera Hardware Design and Testing

The star cameras provide the fine pointing solution for the telescope, so that the location of the incident ultra hard X-rays can be determined precisely and the motors can hold the target in the field of view of the telescope. Because the X-rays easily penetrate through the balloon, but are absorbed by the atmosphere, it is desirable to point the X-ray telescope to the zenith, directly through the balloon. The star cameras detecting optical light must then be pointed off the telescope axis to determine the pointing direction of the X-ray telescope.

My major hardware work on the star cameras was to optimize the best integration time for different operational modes. For instance, doing temperature testing to observe the change in focal properties of the lens, designing a stepper motor to ensure the cameras stay focused during flight, selecting a filter to limit sky brightness, and constructing a baffle to limit off-axis optical light. I used a variety images from the last flight to test the star cameras as well as real time testing on top of the Nagoya science building.

An overview of the electronic system for each star camera is shown in Figure 5.3. The flight control computer initiates a TTL pulse to instruct the CCD to take an image. This image is processed by a small single board computer with the star camera code to find an attitude solution and PSF of the image that is passed back to the flight control computer. Once every 10 seconds, an image is stored to the external hard drive. If the PSF of the image is poor, a focusing sequence can be done using the stepper motor. The temperature and pressure are monitored during flight and a heater can be used to keep the CCD within operating temperatures. If necessary, an image can be sent to the ground station for further analysis.

The star cameras provide the fine pointing solution for the telescope with sensitivity to stars down to magnitudes ≈9 in daytime float conditions. Each camera (Figure 5.4) combines a 1 megapixel CCD with a 200 mm f/2 lens to image a 2° by 2.5° field of the sky. I obtained two CCDs to use on the star camera's, a Prosilica GE 1380 and 1650. The Prosilica 1650 was more expensive and supposedly more sensitive. I tested both CCD's (Table 5.1) to determine which one was more effective in our star camera application and to test the affects of different temperatures on the CCDs. I found that the cheaper CCD was more effective than the more expensive CCD in terms of having fewer hot pixels as well as having hot pixels that were found in all images that could be easily removed with a mask. I also found that
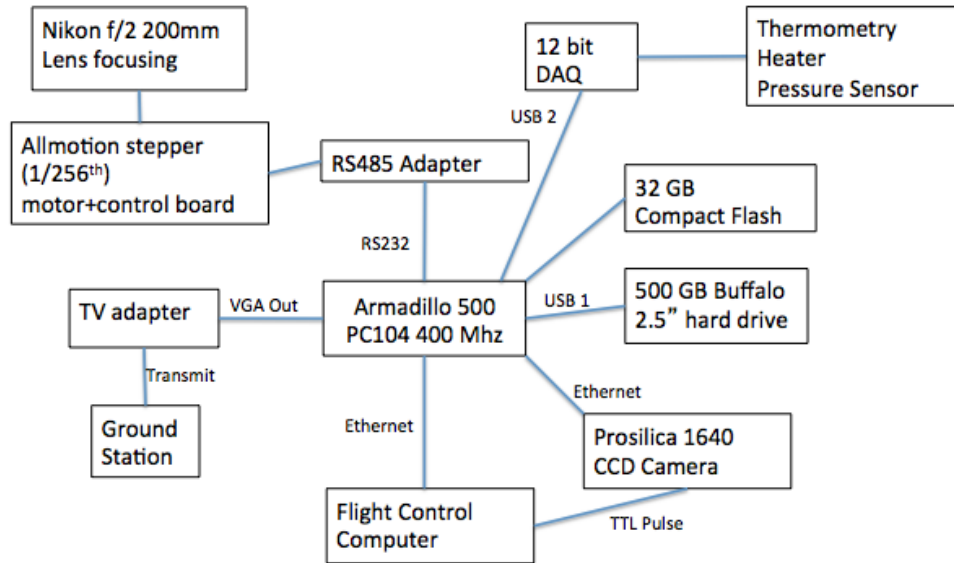
Figure 5.3: Overview of the electronic system for each star camera.

Figure 5.4: Star camera lens (Nikon 200 mm lens with 2.56 x 1.92 degrees FOV) and CCD (Prosilica GE1650).

the number of hot pixels and dark current increases slightly at higher temperatures.

The work on the star camera focused on optimizing several factors including a filter to maximize signal to noise of the stars during day operations, determining the quickest integration time for reliable solutions during different operating conditions, designing a focusing system on the camera to deal with the extreme temperature variations of day/night during balloon flight. At typical balloon altitudes there is still atmosphere to create a bright daytime sky background, so a filter needs to be used during daytime operation. This filter needs to be optimized to maximize the star signal to background in daytime operations and maintain nighttime perfor-

mance.

Table 5.1: Star camera CCD testing results for Prosilica 1380 and 1650 under normal and hot ($\approx$120 degrees F) operating temperatures.

CCD characteristics	1380	1380hot	1650	1650hot
Row Pixels	1360	"	1600	"
Column Pixels	1024	"	1200	"
Total Pixels	1392640	"	1920000	"
Max Bias of all pixels 5 trails	1	1	2	"
Average Bias/pix	0.382	0.386	0.52	0.53
Dark current/pix/sec	0.041	0.056	0.0146	0.047
Top pixel 1 sec	77	84	206	213
Top 5 hot pixels/cts/sec	20.2	28.2	168.2	202.2
Next 10 hot pixels/cts/sec	3.9	5.61	102.7	177.7
Next 25 hot pixels/cts/sec	2.8	3.6	78.7	149.4
Top 5 hot pixel similarity at 0.1,1,15 sec exp	80%	80%	40%	40%
Hot and Cold top 5 similarity	80%	"	60%	"
Hot+Cold top 50 similarity	88%	"	74%	"

A final critical element of any day time operating star camera is the baffle. The baffle was constructed to ensure all stars greater than $\approx 10°$ from the optical axis are blocked, so that the camera can image during daytime within $\approx 60°$ of the sun. This baffle must also limit scattered light from its surface. The baffle is attached to the front of the star camera and is sandblasted using anodized aluminum to prevent scattered light and reflections inside the baffle.

5.5 Star Camera Software and Testing

The software used a modified form of the pyramid algorithm, using the angles of individual triads of stars on the image to find matches within the look-up catalog. Once this was done a fourth detected star was selected from the image. The four star polygon structure, the pyramid, is associated with an almost certain stellar identification that is efficient and fast. For the catalog search, I used the HEASARC database of SAO stars, which has almost 270,000 stars with V mags and proper motions. The catalog was converted to expected apparent (RA, DEC) based on the epoch of the observation and restricted to a 5 square degree region based on

the approximate pointing solutions from rough sensors like differential GPS or magnetometers, so that a smaller portion of the star catalog is searched. The output solution for each field was the RA, DEC for the center of the field and the rotation angle. After the initial match, the software uses previous star camera solutions for a reference. After the flight, the star camera and gyroscope pointing solutions can be combined to obtain a higher accuracy position estimation.

Another challenge was to determine an integration time that will find the proper solution in the least amount of time given the CDD sensitivity, dynamic range, and expected star brightness. To maintain >4 stars in a frame, the star camera can require an integration time of up to 300 ms in bright daytime float conditions. If this integration time is too short, too few stars will be found for a solution. If the time is too large, the camera can't send feedback to the pointing system rapidly enough to ensure the X-ray target is in the center of the telescope where the response is maximum. For example, at 40 keV, the mirror response drops to 50% at only a few arc minutes off axis. In addition, during telescope movement to a new target, the integration times must be reduced since the images would be streaked as the telescope moves if the same integration time was used as in pointing. Another optimization factor is the effect of temperature variations on the focus of the lens. If the temperature changes the lens can go out of focus and blur the image impeding the star camera matching to a new star field therefore a stepper motor was tested and optimized to adjust the focus with temperature.

To test the most effective input parameters for the software, I used images from a previous flight of InFOCμS in 2004 which used the camera eventually used in the BLAST balloon mission (Rex et al. 2006). The BLAST camera saved images from the InFOCμS flight that I used to test the software (Figure 5.5). In Figure 5.6, I show the number of stars detected at different levels of signal to noise. Using
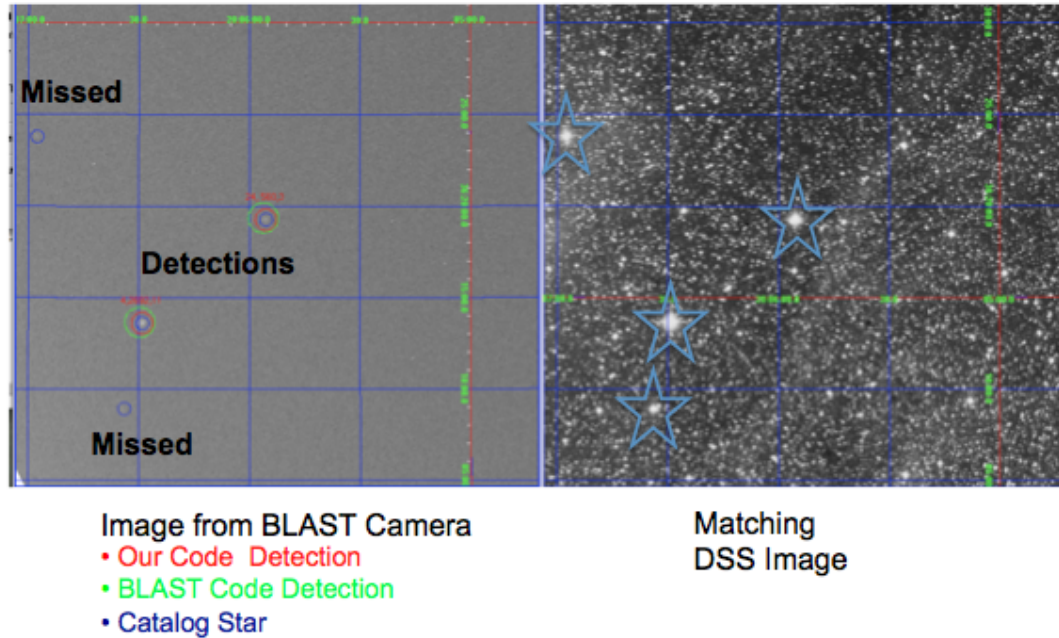
Figure 5.5: *Left*: Image taken from BLAST camera in 2004 flight. Both the BLAST software and our software detect the same stars. *Right*: DSS image of same field showing bright stars.

a detection requirement of $\sigma = 1.4$ in three adjacent pixels, the software is 100% accurate at identifying stars, but finds a smaller number of stars. I also tested the number of stars detected by magnitude and the detected flux in the algorithm.

I also tested the star camera on the top of the Nagoya University Science building on clear nights. Because in the night sky it is much easier to detect stars than in a balloon during the daytime, I was able to detect many more stars in a shorter 0.2 sec integration. In this image the software detected 241 correct stars with a only 10 false detections (4%). Based on the night sky testing in Japan, my software achieved real-time pointing solutions at 5 hz with errors of $3''$ in RA and DEC, and $40''$ in roll. These errors were similar to those from star cameras on other balloon borne telescopes such as BLAST (Pascale et al. 2008).
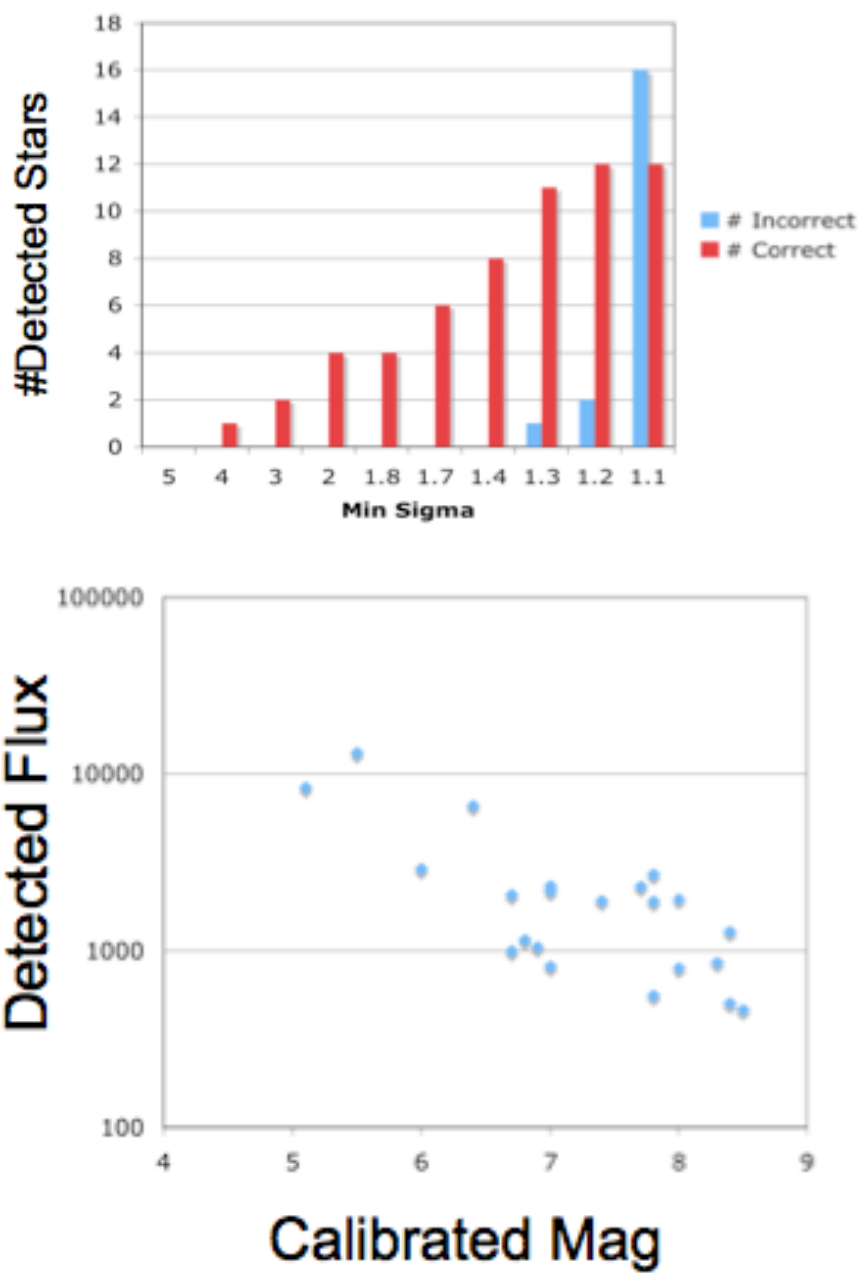
Figure 5.6: *Upper*: number of detected stars with different sigma levels. As the minimum sigma is lowered more stars are detected but some of them are incorrect. *Lower*: detected flux in star camera software vs. calibrated USNO V-band magnitudes.
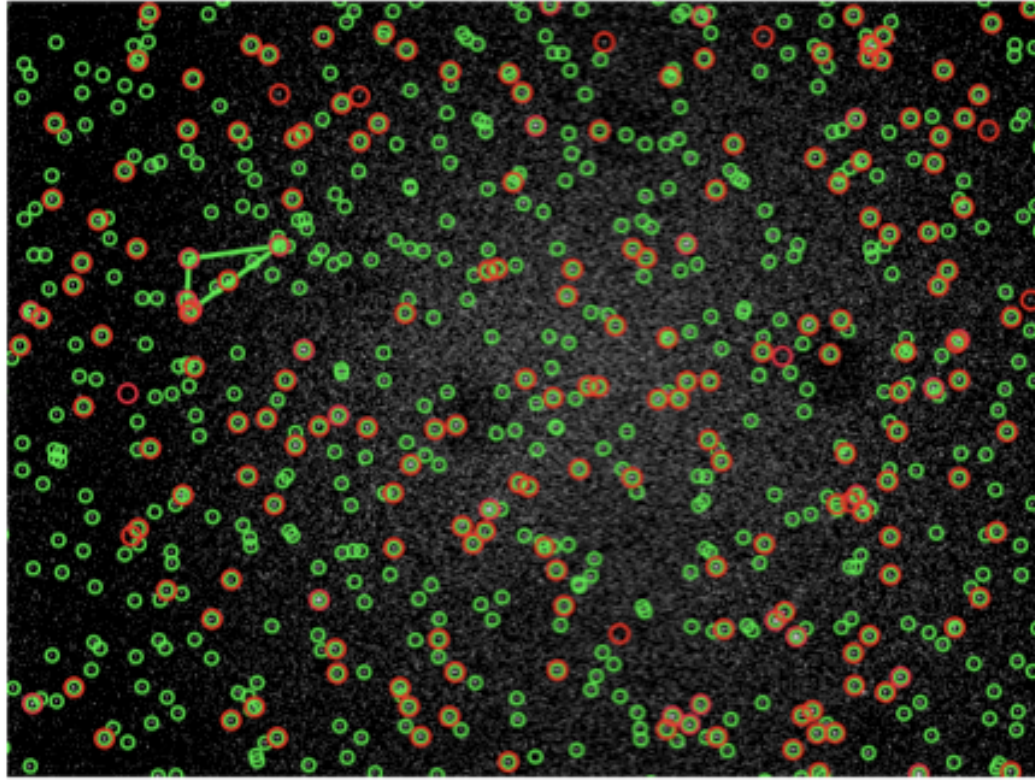
Figure 5.7: Nagoya night sky testing with 0.2 sec integration using the Prosilica 1380 CCD and Nikon 200mm lens with a 4 inch camera baffle. Green circles indicate USNO stars and red circles indicate stars detected by the software. 241 stars are detected with a 10 false detections (4%). The FOV is 2.54° by 1.99° with a pixel scale of $7''$/pixel.

5.6 Summary

Focusing optics in the ultra hard X-rays allow a revolutionizing leap ahead in imaging sensitivity over current coded aperture technologies. The InFOCμS balloon mission was designed to use multilayer mirrors to extend focusing optics to the ultra hard X-rays. As part of the InFOCμS collaboration, I designed the hardware and software for the star cameras that are used to determine the attitude of the X-ray telescope during flight. The errors were similar to those from star cameras on other balloon

borne telescopes such as BLAST. While the instrumentation has not yet flown on InFOCμS, the launch of $NuSTAR$ on February 12, 2012, holds much promise for furthering our understanding of AGN in the ultra hard X-rays by being able to image distant AGN at high redshift where the bulk of black hole growth is occurring. Finally, InFOCμS is eventually expected to fly with a new generation of higher resolution (5–10$''$) ultra hard X-ray optics in 2013 which will need the best resolution achieved by these star cameras.

Chapter 6

Conclusions and Future Work

In this dissertation, we have presented results that show that ultra hard X-ray selected AGN have quite different host galaxy properties than methods using other wavelengths. In particular, we found that BAT AGN have similar [O III] luminosities as the SDSS Seyferts, suggesting that they also have similar intrinsic luminosities, yet they have very different properties in terms of their host galaxy properties.

Among our results from our study of the host galaxies in Chapter 2 is that BAT AGN are powered both through merger events and less powerful nonmergers such as accretion of cold gas in late type systems. Consistent with this, we find that the BAT AGN host galaxies have intermediate optical colors ($u - r$ and $g - r$) that are bluer than a comparison sample of inactive galaxies and optical emission line selected AGN suggestive of younger star formation in gas rich systems. These bluer colors are associated with a much higher fraction of spiral morphologies and mergers in the BAT sample. BAT AGN also tend to be in rare massive spirals with a rate that is 5 to 10 times higher than in inactive galaxies or optical AGN. BAT AGN have enhanced far-IR emission suggestive of higher levels of star formation compared to the comparison samples. Consistent with a link between supermassive black hole growth and the mass of the host galaxy, the average ultra hard X-ray luminosity

increases with stellar mass for BAT AGN. Finally, in agreement with the unified model of AGN, host galaxy colors and morphology of BAT AGN are independent of X-ray column density and optical Seyfert classification.

While many recent studies seem to discount the merging hypothesis in fueling moderate luminosity AGN, this study of BAT AGN has found quite the opposite. In our study of merging and clustering of the BAT AGN in chapter 3, we found a higher incidence of galaxies with signs of disruption compared to a matched control sample (18% versus 1%) and of close pairs within 30 kpc (24% versus 1%). BAT AGN also have a larger fraction with companions compared to normal galaxies and optical emission line selected AGN at scales up to 250 kpc. Our results suggest these merging BAT AGN may not be identified using optical emission line diagnostics because of optical extinction and dilution by star formation. In support of this hypothesis, in merging systems there is a higher hard X-ray to [O III] flux ratio, as well as emission line diagnostics characteristic of composite or star-forming galaxies, and a larger IRAS 60 μm to stellar mass ratio.

If AGN are triggered in galaxy mergers, then we expect some fraction to be a dual AGN. In order to test this hypothesis we obtained *Chandra* imaging of BAT AGN in close mergers. In chapter 4, we discuss the discovery of one of the nearest binary AGN to date, Mrk 739, based on follow up of merging BAT AGN. Mrk 739W showed no evidence for hosting an AGN until the *Chandra* observation despite a host of previous observations including UV and optical spectroscopy, and radio data from the VLA. Consistent with our study of mergers in chapter 3, we found that a high level of star formation combined with a very low $L_{\rm [OIII]}/L_{2-10\,\rm keV}$ ratio cause the AGN to be missed in optical observations. We also found large amounts of molecular gas in the system using ^{12}CO observations of the (3–2) and (2–1) lines that could be driven towards the black holes during the violent galaxy collision and

be key to fueling the binary AGN.

Finally, in chapter 5 we discussed the exciting development of focusing optics in the ultra hard X-rays and the development of the InFOCμS balloon mission. As part of the InFOCμS collaboration, I designed the hardware and software for the star cameras that are used to determine the attitude of the X-ray telescope during flight. The star camera errors were as low as those from star cameras on other balloon borne telescopes such as BLAST. While the balloon was unable to fly again during my PhD, its flight in 2004 marked the first instrument to using focusing optics in ultra hard X-ray imaging.

6.1   Future Work

There are still many exciting scientific projects with the BAT AGN that are extensions of the work done in this PhD. In this next section, we discuss five of these projects in detail.

6.1.1   Broad Band Correlations in the $Swift$ BAT AGN

One of important properties of AGN is the broadband nature of their emission and their spectral energy distribution (SED, Elvis et al. 1994). The AGN bolometric luminosity is one of the most important quantities for understanding the formation and growth of supermassive black holes. In type 1 AGNs, we have a clear view of the central supermassive black hole and we can measure the amount of energy radiated from the far-infrared to hard X-rays. A study of type 1 AGN selected in the ultra-hard X-rays provides a unique opportunity to study the SED of a less biased sample of AGN that already has a wealth of information on the emission in the X-rays.

As part the work determining the colors of BAT AGN, I did extensive modeling using GALFIT of the AGN light in the centers of bright Seyfert 1. A natural result is to construct an AGN SED utilizing these measurements. I also would like to obtain a better understanding of the entire SED of $Swift$ BAT AGN including how spectroscopic measures correlate with AGN bolometric luminosity, as well as the nature of the MIR to FIR emission.

An understanding of the AGN bolometric luminosity is also timely because large surveys such as the SDSS, 2dF Galaxy Redshift Survey (Colless et al. 2001), and the 6dF Survey (Jones et al. 2004), are finding samples of hundreds of thousands of AGN. While the use of diagnostic lines provide an important understanding of different types of AGN such as LINERs or Seyferts, these surveys often use a single measure such as [O III] flux to measure the intrinsic bolometric luminosity of the AGN. Finally, previous studies of the initial 9 month sample of BAT AGN have found a weak correlation between [O III] luminosity and hard X-ray luminosity (Meléndez et al. 2008; Winter et al. 2010).

Another important issue in the study of the AGN bolometric luminosity is the nature of the MIR to FIR emission. Some authors attribute the bulk of the radiation to star formation in the dusty host galaxy, even for luminous AGN. However, as we found in Chapter 2 there is also a significant correlation between the BAT ultra-hard X-ray luminosity and the FIR luminosity. The new availability of all sky observations from WISE and Akari, as well as archival observations from IRAS, offer a greater potential to understand the nature of the MIR to FIR emission.

I do have some preliminary results for the optical SED of BAT AGN. In Figure 6.1, we find a linear correlation between i-band PSF emission using Seyferts 1s and BAT luminosity. In this sample, we excluded galaxies classified as Seyfert 1.9 as well as X-ray absorbed Seyfert 1s. In Figure 6.2, we plot correlations for all of the
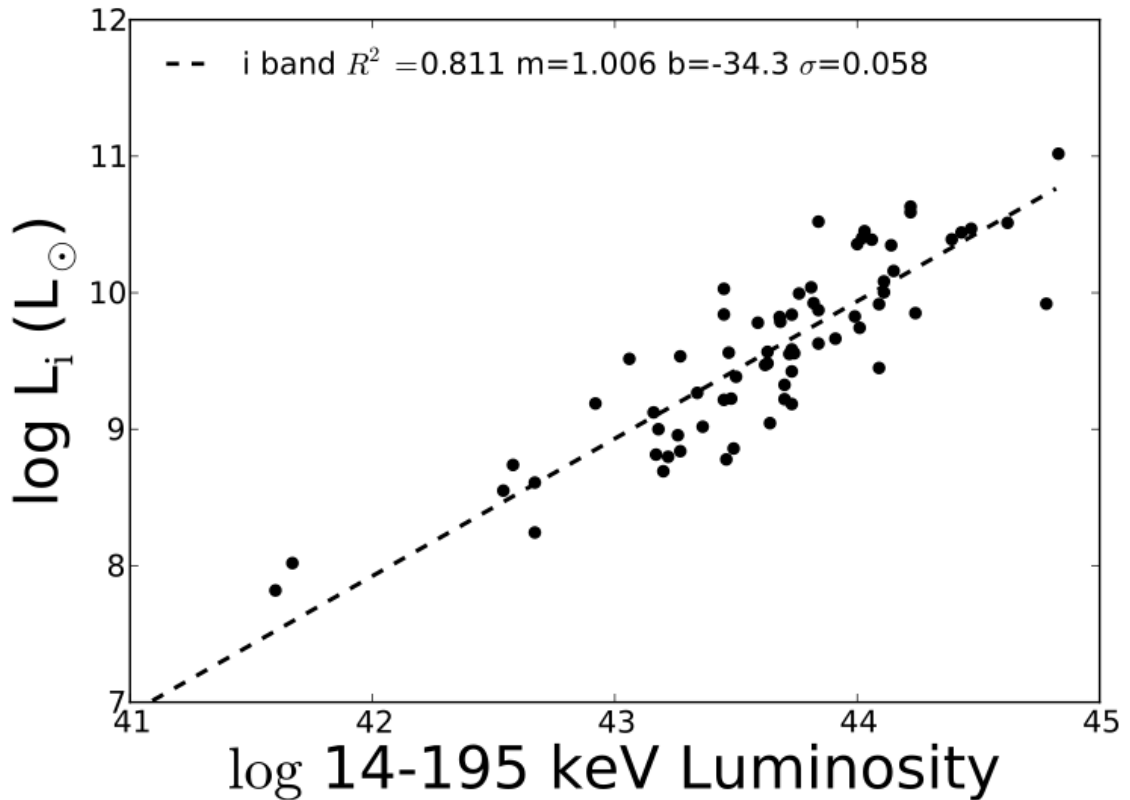
Figure 6.1: Optical AGN Emission in the i band vs. BAT luminosity.

AGN emission measures in the *ugriz* with GALFIT, where we again see a strong correlation of optical emission with ultra hard X-ray emission. We also show the [O III], [O IV], and 2-10 keV X-ray emission correlations. We find the strongest correlation in 2-10 keV emission, but a much weaker correlation in [O IV] and no correlation in [O III]. This suggests that [O III] emission may be a poor estimate of intrinsic bolometric luminosity.

Since correlations in luminosity are biased because of the common multipliers of distance, we also plotted the correlations in the average flux ratios with ultra hard X-ray emission. In Figure 6.3, we show this scatter as the coefficient of variation in the flux ratios. The coefficient of variation (CV), defined as the ratio of the
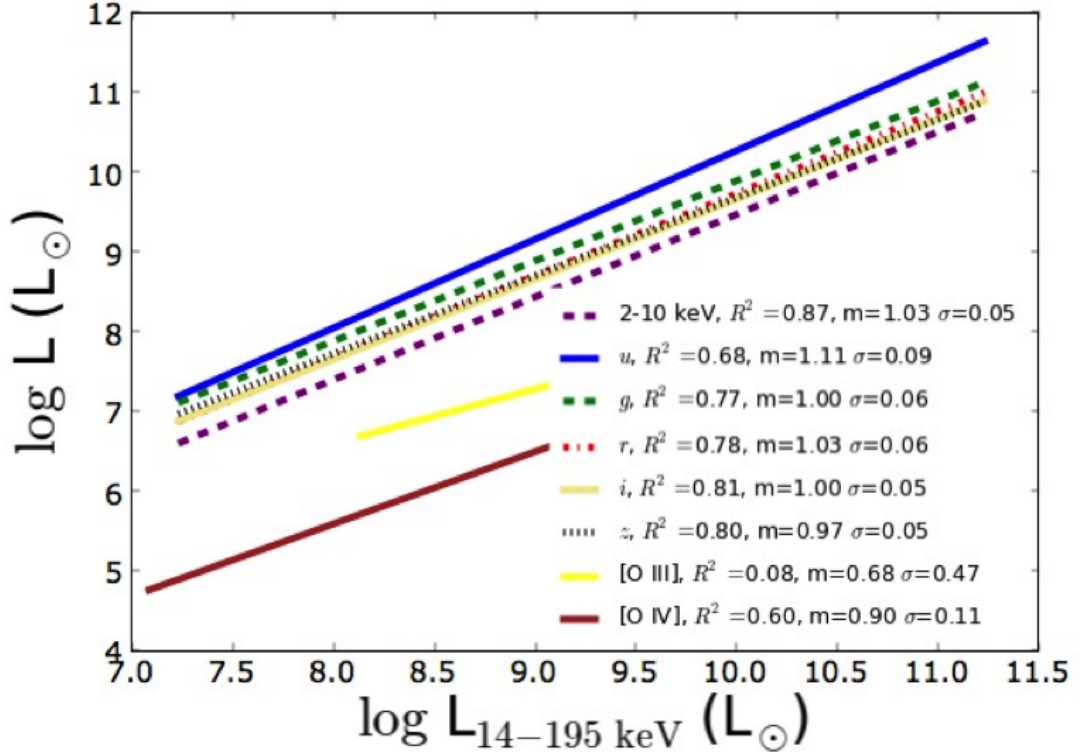
Figure 6.2: Correlations of multiwavelength AGN emission with BAT luminosity.

standard deviation to the mean ($\sigma/mean$), is a normalized measure of dispersion of a probability distribution to enable comparisons of data with different means. We find the lowest CV in the flux ratios of the optical and 2-10 keV emission to ultra hard X-ray emission. As we move from the NIR to FIR, we find a increase in the CV compared to the ultra hard X-ray. Finally, in the [O III] and [O IV] emission lines we see a much larger CV with ultra hard X-ray emission consistent with the poor correlation we found in our previous luminosity comparison.

We also measured the Eddington ratios for 90 BAT AGN with available black hole masses (Figure 6.4). Black hole masses were from reverberation mapping, Hβ, or velocity dispersions (for Seyfert 2). We assumed L$_{Bol}$= 15×L$_{BAT}$. We find an average Eddington ratio for broad line sources of 0.18±0.17 and for narrow sources
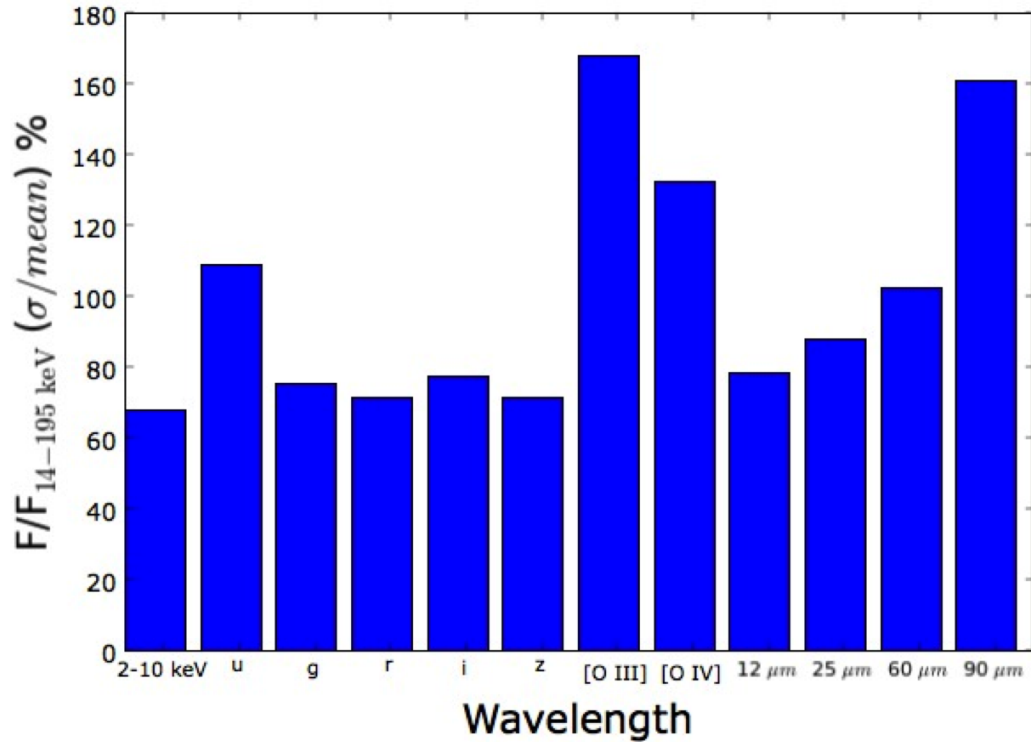
Figure 6.3: Variability of average flux ratios of ultra hard X-ray emission compared to other wavelengths.

0.085±0.086 for the BAT AGN sample. We also plot the Eddington ratios by galaxy morphology (Figure 6.5). We don't see any significant dependence on morphology such as mergers or spirals having higher Eddington ratios.

6.1.2 The Frequency of Dual AGN Activation in the Local Universe

One of the exciting results found in this thesis was that BAT AGN in merging galaxies, such as Mrk 739, may be hidden double AGN systems only detectable in the hard X-rays. An extension to this work would be to look at the frequency of dual AGN activation in the Local Universe for the entire merging sample of BAT
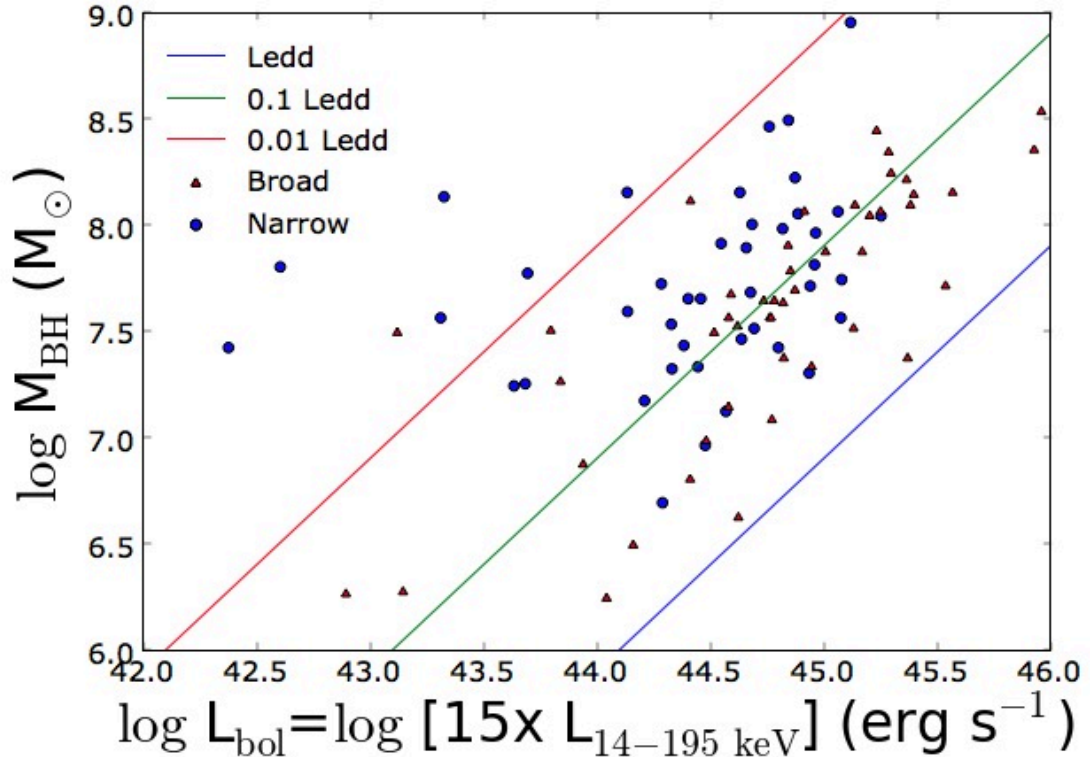
Figure 6.4: Eddington ratios of BAT AGN.

AGN.

Based on extensive optical follow-up as part of my thesis, I have identified 50 nearby BAT AGN in the process of merging in the northern hemisphere ($<$30 kpc companion, z$<$0.05). 24% or 12/50 of these AGN appear to be dual X-ray AGN indicating that this is an excellent sample to understand AGN triggering. The available X-ray data vary from objects whose luminosity are within a factor of 5 of each other (NGC 6240, IRAS 0342+44) to objects with a ratio of 100:1 (NGC 2992/2993). Over half (44%, 22/50) of these merging AGN have only low quality data from *Swift* XRT, where a faint or close X-ray AGN would be missed. Approximately a quarter (24%, 12/50) are in apparent mergers, but don't have optical spectra for the galaxy companion.
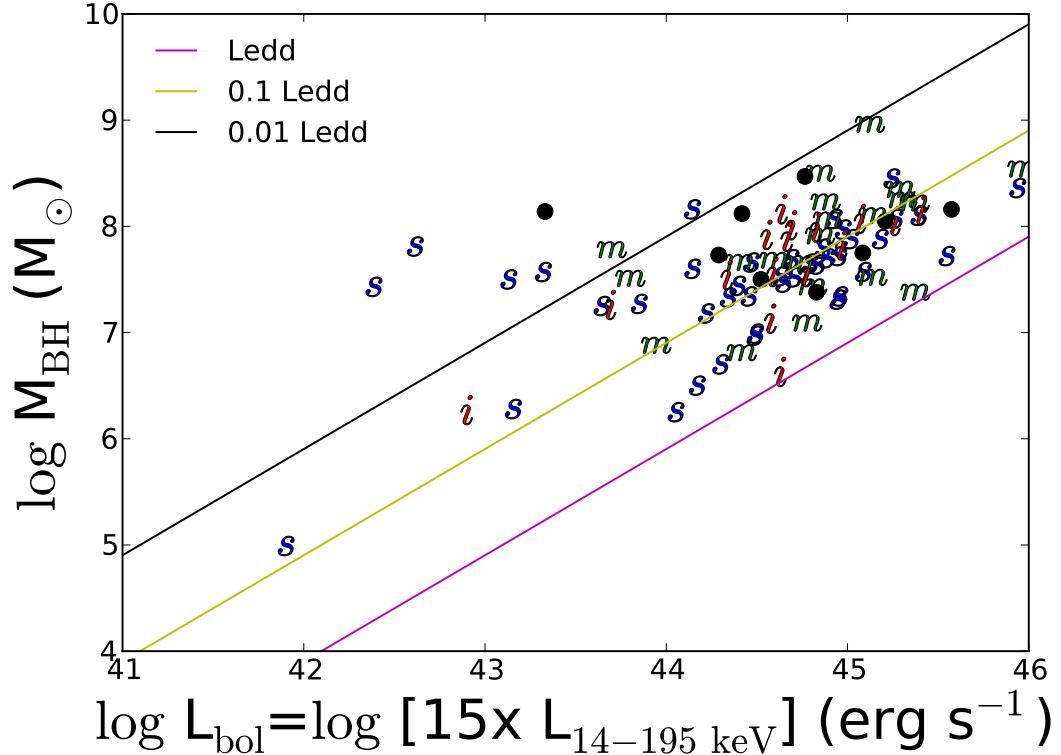
Figure 6.5: Eddington ratios of BAT AGN by morphology. In this plot s is for spiral, m for merger, a dot for elliptical, and i for intermediate between spiral and elliptical.

As I found in my thesis work on Mrk 739, additional high resolution *Chandra* data for this sample is crucial for determining the nature of any dual AGN sources since other methods can be biased. We are in the process of obtaining *Chandra* imaging for another 10 BAT AGN in mergers with companions within 15″. We have received data for 7/11 of our approved targets (including the double AGN Mrk 739). Of these IRAS 0558 is a clear dual AGN with nuclear X-ray emission from a dwarf companion 20″ (13 kpc) to the north (Figure 6.6). Later Gemini spectra confirmed the northern source is a Seyfert 2 at the same redshift and this system is a dual AGN.

We do have some exciting preliminary results from our sample. The mean 60
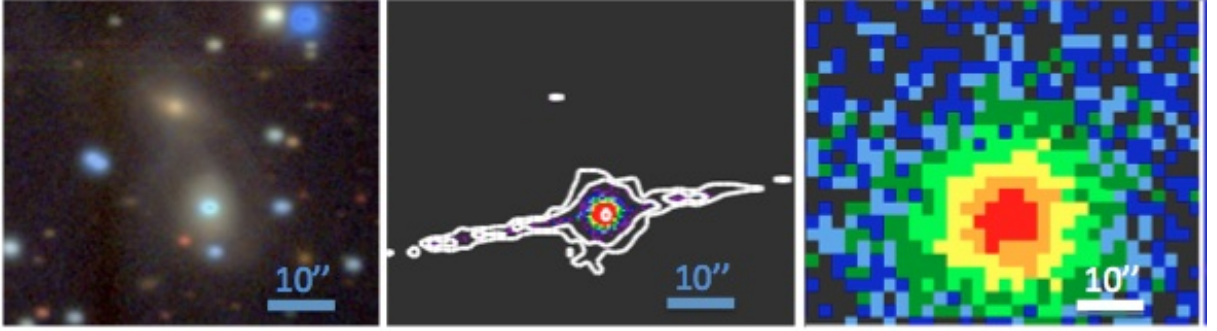
Figure 6.6: *Left:* Tricolor *gri* Kitt Peak image of IRAS0558. The two galaxies are separated by 19″ and both show hard X-ray emission. *Middle: Chandra* observation obtained in January, 2011 as part of our previous *Chandra* program. There is a faint northern X-ray source coincident with the northern galaxy. *Right: Swift* XRT image in same scale with no detection of the faint northern X-ray emission, showing the importance of the high resolution of *Chandra* in detecting dual AGN that are within 25″ of each other.

μm emission to stellar mass for the dual AGN is 4 times larger than for the other hard X-ray selected AGN, suggesting that these systems may be linked to significant amounts of star formation. The ratio of mean hard X-ray emission to stellar mass is also 3 times larger than the average for the BAT sample, suggestive of higher accretion rates. Our non-detections in the *Chandra* sample are all for low mass mergers suggesting that dual AGN are more prominent among major mergers where the neighboring galaxy is within a factor of 3 in stellar mass. Additionally, 8/12 of the systems show high column densities systems and are narrow line optical AGN. If we exclude those galaxies in close mergers ($<10″$) without *Chandra* imaging where we couldn't resolve X-ray emission from a second source and those without optical spectra for the second galaxy, we find a surprisingly high dual AGN fraction that peaks at close separations (Figure 6.7). These results can only be substantiated with a larger sample (there are only 12 X-ray detected dual AGN in the BAT sample including the 2 new ones from our 2011 *Chandra* observations).

We are also in the process of obtaining optical spectroscopy for some remaining
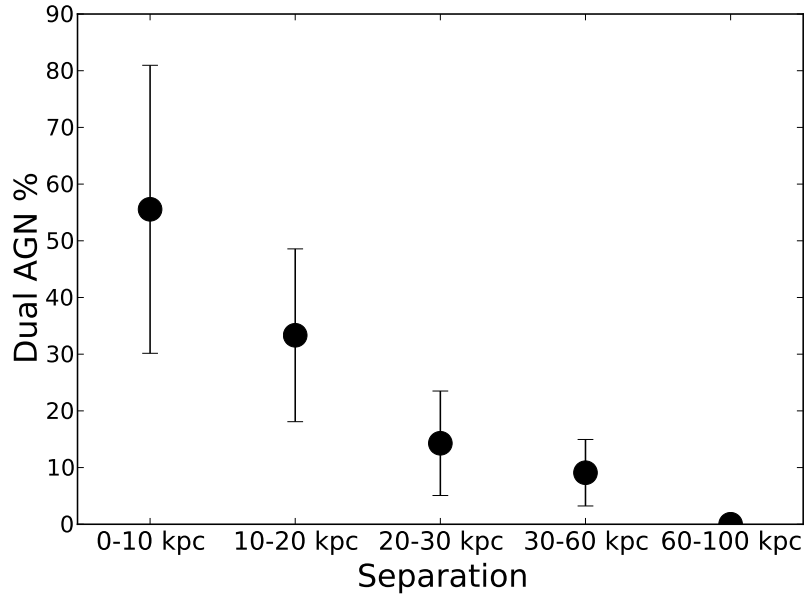
Figure 6.7: Fraction of dual AGN by projected companion separation from a sample of merging BAT AGN. We have also included the dual AGN fraction of a sample of 44 BAT AGN in the SDSS with companions at separations between 30 and 100 kpc.

galaxy mergers in our sample which will likely increase our fraction of dual AGN. Unfortunately because of fiber collision limits, most merging galaxy companions are missed in large surveys. We have found 3/50 in systems with dual optical AGN, but no detected secondary X-ray AGN, presumably because they are Compton-Thick and all X-ray emission is blocked. Optical emission line diagnostics may detect emission from the narrow line region gas, which is further from the obscuring torus and may be seen even if the AGN is Compton-thick.

Finally, we are obtaining optical imaging in the southern hemisphere to identify additional merging BAT AGN for X-ray follow-up. Our final goal will be to obtain a significant number of dual AGN (>25) with X-ray observations to understand AGN triggering in detail. These data will provide a sample to determine the incidence of multiple accreting nuclei in the low redshift universe for the first time.

6.1.3 Optical Spectra of the 22 month Sample of AGN

Since much of this thesis focused on the imaging properties of BAT AGN, another important part of the work on BAT AGN is to investigate the optical spectra of BAT AGN. As part of this we obtained optical spectra of 60 BAT AGN using the 2.1m Kitt Peak telescope over 14 nights. A sample Kitt Peak spectra of Mrk 3 can be found in Figure 6.8. Optical spectra provide a wealth of information in terms of stellar and AGN emission lines, the continuum power law of the AGN, the stellar continuum, and the level of extinction in the vicinity of the AGN.

We would like to use the optical spectra to answer the critical question of how the BAT sample is different from selection using optical spectroscopy. We will classify our sources using the criteria of Kewley et al. (2006) as H II galaxies, Seyferts, or LINERs using emission line criteria. Using the 60 BAT AGN from Kitt Peak and ≈70 AGN with available spectra in the SDSS, we will be able to identify a large sample of AGN that are missed using emission line diagnostics and try to answer the question of whether they are missed because of excess star formation diluting the AGN lines or obscuration or some other cause. This is important because Suzaku observations from Ueda et al. (2007) of two heavily obscured BAT AGN suggest that these AGN have an extremely geometrically thick torus with a small opening angle and/or have an unusually small amount of gas responsible for scattering with none of the usual emission lines like [OIII] $\lambda5007$ from scattered gas. Finally, by modeling the continuum with a power law from the AGN and stellar populations we can get a comparison of the level of star formation near the AGN that we can use along with our imaging results.

We have several other goals for this spectroscopy project. In the same way as we did in Chapter 2 and 3, we want to make a comparison of randomly selected Seyfert
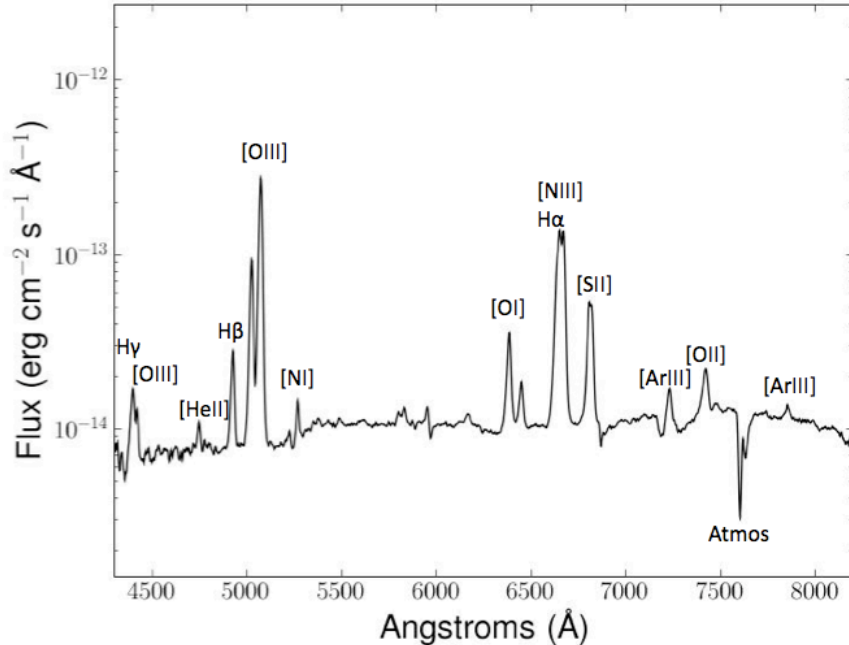
Figure 6.8: Goldcam spectra of Mrk 3 obtained in December 2008 at a resolution of 400 km s^{-1}.

2 AGN from the SDSS with the optical spectroscopy of BAT AGN. We would like to compare average level of extinction. We will also compare line diagnostics to BAT luminosity that correlates with optical signatures of AGN like [O III].

Finally, because of the proximity of the BLR to the central source, measurements of the BLR in Seyfert 1 are linked to the mass of the black hole. We plan to measure the black hole mass using the FWHM of the Hβ line and the λ5100 continuum luminosity using the relation from reverberation mapping (Bentz et al. 2006).

6.1.4 NIR Spectra

Since the extinction coefficient in the K-Band is nearly 10 times smaller than the optical (Veilleux 1999), NIR spectroscopy enables a test of whether the misclassification of BAT AGN discussed in the previous section is caused because of extinction or by dilution of the AGN emission by starlight. In particular, we would like to look

at NIR AGN diagnostics on a sample of merging AGN detected in the X-rays but misclassified as starburst using optical emission diagnostics. This will enable a test of our hypothesis in Chapter 3 that optical spectroscopy of merging AGN is biased because of unaccounted obscuration associated with the violent galaxy merger. Furthermore, we would like to test a large sample BAT AGN with optical diagnostics that classify them as starburst or those BAT AGN that have weak or no optical emission lines (Figure 6.9).

We also like to investigate those AGN with mismatched Seyfert 1 and 2 classifications based on optical emission line widths and X-ray column densities (Figure 6.10). These objects may be a new class of AGN already discovered at higher redshift, but currently with no low redshift analogs. In the XMM large scale structure survey, 7 out of 61 (11%) optical broad line sources exhibited X-ray absorbed spectra (Garcet et al. 2007). These sources were at much higher redshift ($<z>= 1.93$) than our target sources. As the low-redshift analogs of this class, we would be able to study the sources and hosts in much greater detail.

6.1.5   Molecular Gas in Ultra Hard X-ray Selected AGN

The link between star formation and feeding supermassive black holes is poorly understood. Several observational studies have found that many active galactic nuclei (AGN) host galaxies appear to be in the green valley on the color-magnitude diagram, in between actively star-forming galaxies in the blue cloud and passively evolving galaxies on the red sequence (Georgakakis et al. 2008; Schawinski et al. 2009a; Silverman et al. 2008). The lower levels of star formation have been attributed to AGN feedback where the reservoir of gas is heated and expelled during a phase of accretion onto the central supermassive black hole. However, direct observational evidence for a link between the destruction of this molecular gas and an AGN phase

Figure 6.9: Example of optically elusive detected BAT AGN with weak or no optical emission emission lines. In both of these cases, the Hβ line is not detected and the [O III] line is only weakly detected.

has been missing so far.

There is also a significant correlation between the BAT ultra-hard X-ray luminosity and the FIR luminosity as we found in Chapter 2. However, it is not clear if the variance is due to the contribution from star formation or from the IR AGN contribution. In addition, hard X-ray selected AGN tend to have much more FIR emission than optical AGN with similar AGN power based on the [O III] ionization line. A study of the amount of molecular gas in the BAT AGN could solve this degeneracy by identifying whether these AGN tend to have large amounts of molecular gas fueling increased levels of star formation or instead are involved in

Figure 6.10: Comparison of optical line width of Hα to the measured X-ray column. Broad line sources are red triangles and narrow line sources are blue circles. X-ray methods classify AGN as Seyfert 1 and Seyfert 2s based X-ray column densities of greater or lesser than 10^{22} cm^{-2}. Above these column densities the optical flux from the BLR close to the AGN is heavily obscured and only the scattering from the NLR should be observed. For those narrow line objects with low X-ray column densities the absorption may be due to dust which can be measured from line ratios and continuum emission in the NIR.

the destruction of molecular gas in the host galaxy.

We have used the James Clark Maxwell Telescope (JCMT) to observe 40 BAT AGN in the submillimeter to study the link between star formation, molecular gas destruction, and the AGN (Figure 6.11). Since molecular hydrogen is difficult to detect by infrared and radio observations, and the ratio between CO luminosity and H$_2$ mass is thought to be constant, CO offers a tracer of molecular gas. CO (high-J)/(low-J) intensity ratios have also been shown to be good tracers of molecular gas temperature and density within galaxies. We also observed 10 optical AGN from the SDSS matched in stellar mass and AGN luminosity to the ultra hard X-ray selected AGN to provide a control sample to test whether optical AGN samples may find AGN with less molecular gas. We have just completed our observations, and we detect only 1/10 optical AGN and 34/40 BAT AGN in CO, suggesting BAT AGN
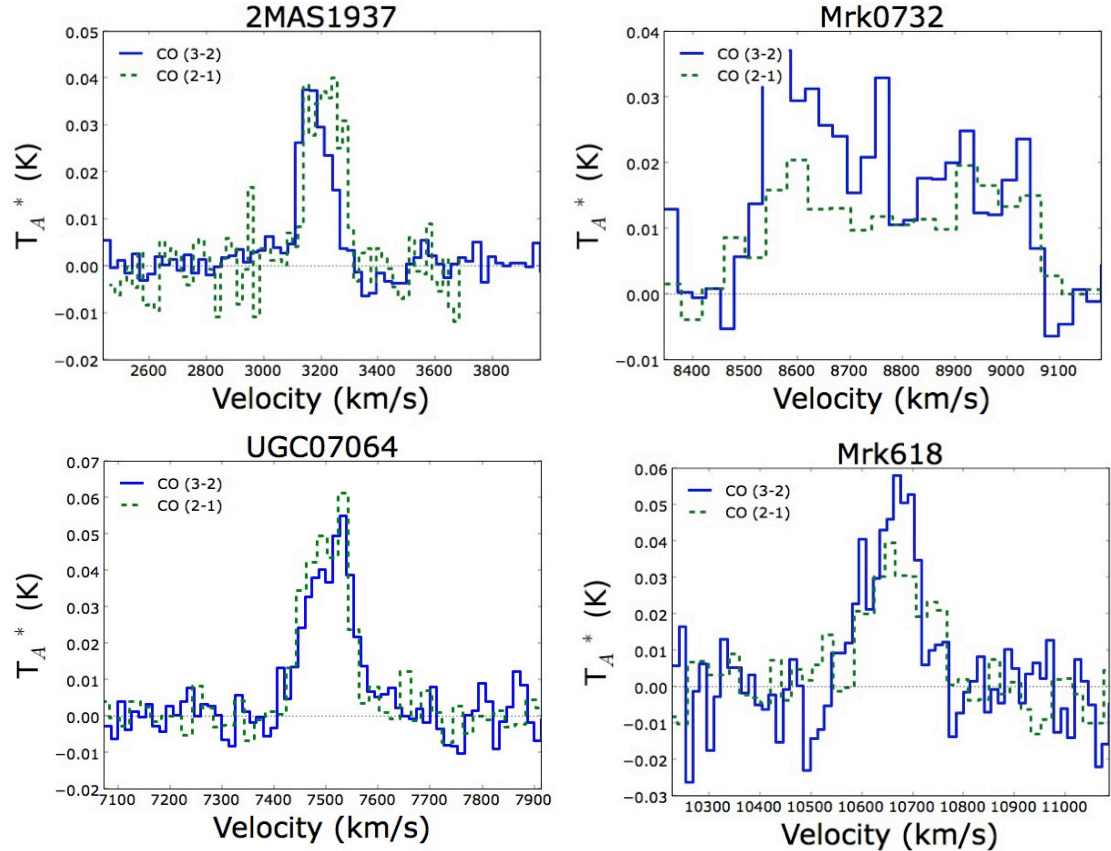
Figure 6.11: Sample of 4 observations of BAT AGN observed from the JCMT in the ^{12}CO(2–1) and (3–2) transition.

tend to have larger molecular gas reserves consistent with their larger amounts of star formation.

6.2   Final Thoughts

While mega surveys such as the SDSS, 2dF, and 6dF are finding valuable information on hundreds of thousands of AGN using optical emission line diagnostics, our study of BAT AGN found that this technique can be heavily biased against finding certain types of AGN like mergers or starbursts in spirals. These selection biases can hide many of the triggering mechanisms of AGN.

Although $Swift$ BAT has had many exciting discoveries described in this PhD

and many additional projects still to be done to understand nearby AGN, future ultra hard X-ray missions hold much promise. By using focusing optics in the ultra hard X-rays, a much higher subarcminute resolution and lower noise will resolve much of the X-ray background enabling the detection of a large population of high redshift sources as well as even more heavily obscured sources. Beginning with the launch of $NuSTAR$ in 6 months, and continuing with $Astro-H$, this will revolutionize our understanding of black hole growth in high redshift AGN that trace the peak growth and evolution of black holes as well as heavily obscured AGN.

Appendix A

Appendix to Chapter 2

In this appendix, I provide supplementary material for chapter 2 on the host galaxies of ultra hard X-ray selected AGN. We explain in detail our simulations using GALFIT to ensure the AGN is subtracted properly before measurement of host galaxy color. We also have additional details about the comparison SDSS sample and catalog as well as selection effects in the BAT and SDSS survey. Finally, we provide accompanying tables for this chapter.

A.1 AGN Subtraction and GALFIT Analysis

The AGN color is bluer than the host galaxy, so it is important to accurately subtract the AGN light before doing photometry of the host galaxy (Figure A.1). Two-dimensional surface brightness fitting was done using GALFIT (Peng et al. 2002) in the *ugriz* band to measure and subtract the AGN light. The program can simultaneously fit an arbitrary number of components using χ^2 minimization to determine the best-fit parameters. Our choice of GALFIT is based on the recent comparison of GIM2D vs. GALFIT which showed better fitting results and stability in finding solutions (Haubler et al. 2008). While the median atmospheric seeing of our sample
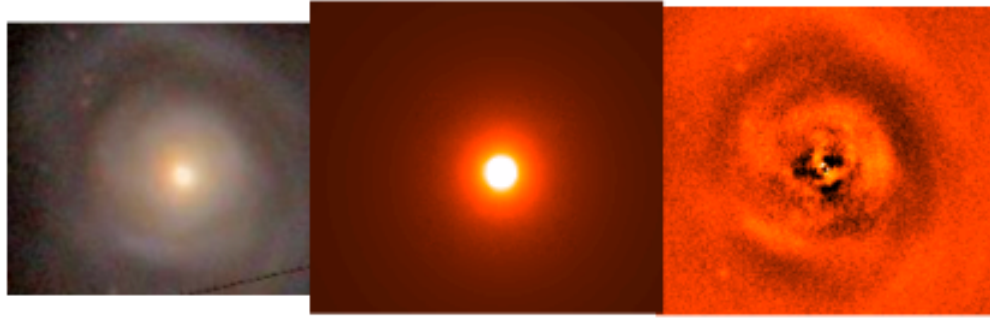
Figure A.1: *Left*: *gri* composite image of NGC 5548, a Seyfert 1.5, S0/a, with a larger ring. *Middle:* GALFIT fitting with a disk (n=1) and bulge (n=4) component. *Right:* Residuals left after fitting with GALFIT. The residual image is useful for showing what is not being fit, for instance, the non-axisymmetric spiral arms and large ring beyond the spiral arms.

was only $\approx 1.5''$, since the sample is at a very low redshift, this ground-based optical imaging is comparable or even superior to the best HST images at high-redshift (z>0.5).

Initial estimates of galaxy magnitude, position, position angle, axis ratio, and half-light radius were provided using SExtractor following the GALAPOGOS routine (Haubler et al. 2008). A point source (PS) was used to fit the AGN light. The PSF was modeled using five coadded bright stars in the same image field as the galaxy. An initial run of GALFIT was done using only a PS component to replace the SExtractor inputs for central position and PS magnitudes. Sky background estimates were made using SDSS sky values or from SExtractor.

To model the galaxy light we used the Sérsic profile, which is an exponential function with a variable half-light radius and an exponential parameter, n, called the Sérsic index (Sérsic 1968). For n=1, the Sérsic profile is the same as an exponential disk model. When n=4, the Sérsic profile is the same as a de Vaucouleurs bulge. Other authors have used different fixed and floating Sérsic index models including

a fixed bulge (n=4), a fixed disk and bulge (n=1 and n=4), and a floating Sérsic index (Schawinski et al. 2009b; Veilleux et al. 2006, 2009a). While a detailed study of the most effective way to measure the AGN and galaxy light has been done for simulated HST images (Kim et al. 2008; Pierce et al. 2010; Simmons & Urry 2008), little has been done for ground-based images similar to the current study. Therefore, to determine the best modeling approach with GALFIT and the associated error, we simulated AGN galaxies for both our Kitt Peak and SDSS images.

To determine the best model to measure the AGN and galaxy light, we simulated broad-line AGN galaxies by adding bright stars to the centers of images of inactive galaxies and NL AGN. We randomly selected one star from our images to use as the simulated AGN PS and placed it in the center of the galaxy. Since the SDSS and Kitt Peak data had different PSFs and exposure times, we tested them separately. To test the SDSS data, we selected 15 inactive galaxies from the SDSS catalog which matched in redshift, color, and apparent magnitude to our Seyfert 2 galaxies with $0.025 < z < 0.05$. These galaxies are the most distant in our sample and have the poorest resolution, so PS subtraction leads to large errors; they therefore serve as a worst case scenario for our sample. For the Kitt Peak images we chose a sample of 10 of the BAT Seyfert 2 galaxies with the same redshift range. For each of the simulated AGN galaxies we added the star at incremental percentage ($\%PS_r$) values of total (AGN and galaxy) light in the r band. In total, to test them in each filter, we created 300 simulated AGN galaxies and ran GALFIT 3500 times. We then used these simulated AGN galaxies to test the effectiveness of GALFIT with different models.

Figure A.2 shows the simulation results for the different Sérsic models for increasing $\%PS_r$ light in the r band. We did not find a significant difference in GALFIT modeling using the Kitt Peak or SDSS samples, so these results include both sam-

ples. We found an inaccurately modeled PSF will force GALFIT to converge to artificially high Sérsic indexes for the galaxy model. This has also been found in simulated HST images (Kim et al. 2008; Simmons & Urry 2008). The PSF mismatch causes light from the host galaxy component to be artificially increased by effectively taking light from the AGN component. This happens by inflating the galaxy Sérsic index. This effect increases as the $\%PS_r$ increases. In addition, as we move towards larger $\%PS_r$, the associated standard deviation of error of the modeled galaxy light increases.

To accurately remove the AGN light, it is important to choose the best model. We did this by finding the difference between the modeled galaxy light and the actual galaxy light. When no PS component is used in the models, GALFIT still finds a faint AGN, so after subtraction, the modeled galaxy light component is fainter than the actual one. When the host galaxy is brighter than the AGN in the r band ($\%PS_r<50$), the worst model is to simply subtract a PS component to estimate the galaxy light because this overestimates the AGN light. For the Sérsic and PS fitting models, the best model is to use an n=4 fixed bulge component and PS or n<4 variable Sérsic index and PS since these models have the smallest average error and standard deviation of error. The worst model is fitting with a disk (n=1) and bulge (n=4) or fitting with a variable Sérsic Index since these models have the largest average overestimation of galaxy light and have the largest standard deviation of error. Simmons & Urry (2008) also found this result using simulated HST images. To avoid any systematic biases against disk-like systems we used the n<4 variable Sérsic index although the fixed bulge (n=4) Sérsic model performed similarly. An initial guess of 2.5 was used for the Sérsic index. The index was allowed to float in the model along with all other values other than the sky background.

The next step was to broaden the examination of GALFIT's performance from
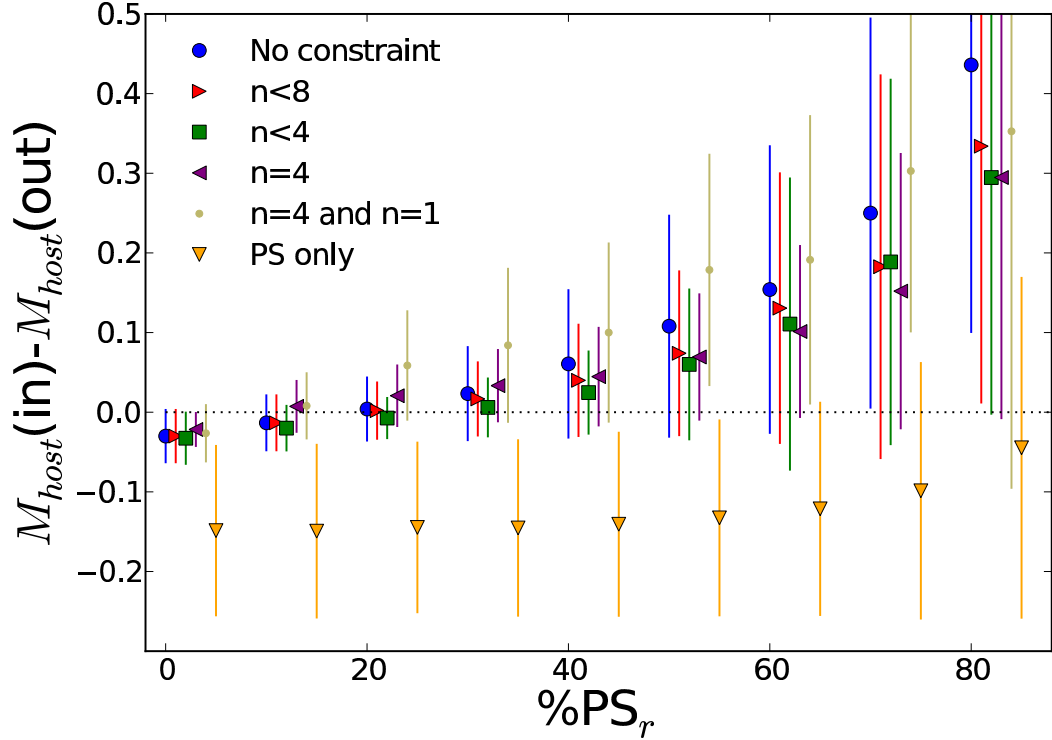
Figure A.2: To determine the best models to use for subtraction of the AGN light, we tested simulated AGN galaxies using different Sérsic models with a point source (PS) to fit the AGN light. We varied the AGN to total light ($\%\mathrm{PS}_r$) in the r band to test how the models performed at increasing levels of AGN light. A positive value indicates that the mean host galaxy light is overestimated. The error bars indicate standard deviations in each bin. As the ($\%\mathrm{PS}_r$) increases the host galaxy light is overestimated by all of the Sérsic and PS models and the standard deviation increases. We find that the model with a PS and floating Sérsic Index with n<4 or n= 4 is most effective at measuring the AGN light based on a lower measured AGN contamination and smaller standard deviation.

one filter to the entire *ugriz* filter set. In Figure A.3 (upper), we show the performance in each of the filters. They are similar to each other, but the blue bands have higher uncertainties because of poorer resolution.

When testing the performance across filters it is important to consider that the AGN SED emits more energy at bluer wavelengths than the host galaxy; otherwise we may underestimate the contamination in the bluer bands. To examine this, we

117
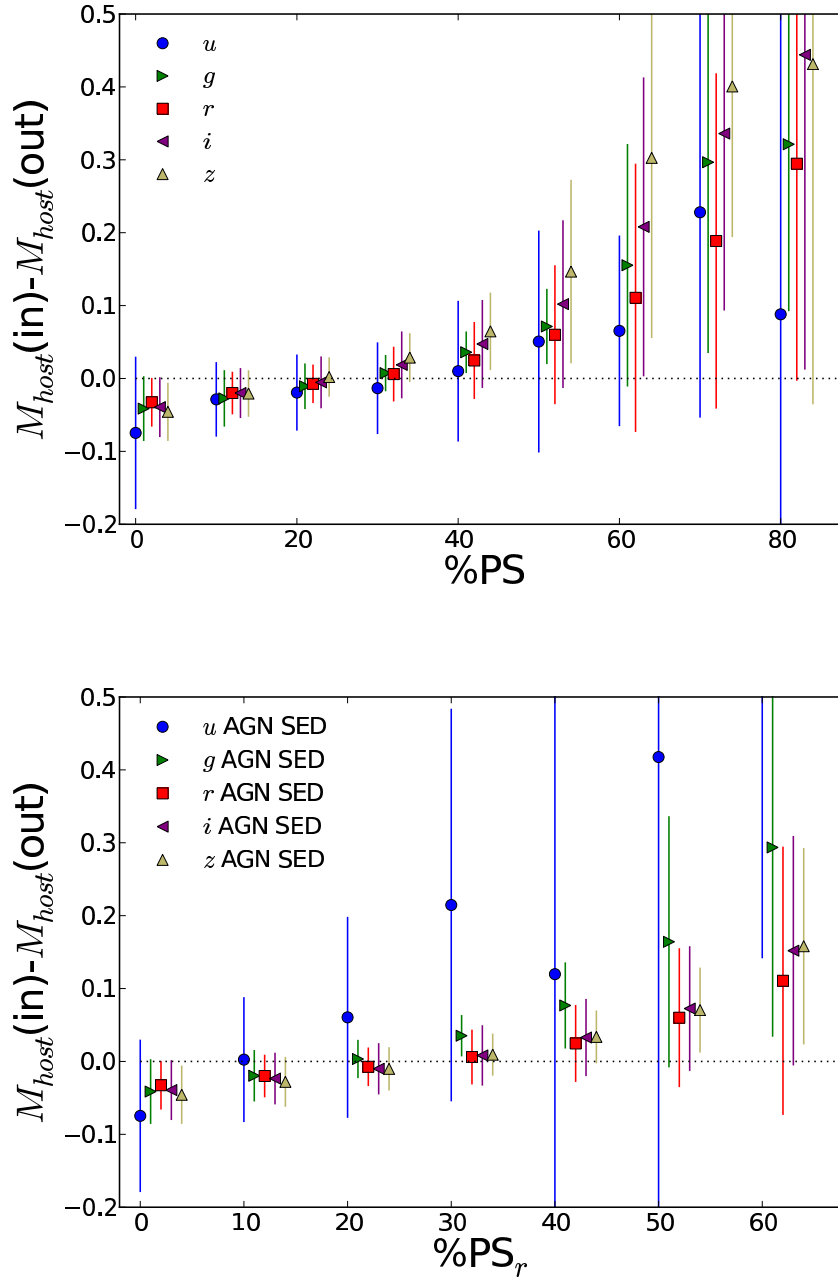
Figure A.3: *Upper Panel*: Effectiveness of GALFIT in removing the AGN light by filter for modeled AGN galaxies. We have used a PS and floating Sérsic Index with n<4 to measure the AGN light. Increasing levels of %PS are shown. As the simulated AGN light increases, the galaxy light is overestimated for all filters. The error bars indicate standard deviations in each bin. The errors are higher for the u and z where the resolution is poorer. *Lower Panel*: We also included the effect of the bluer quasar SED using the colors of AGN (Richards et al. 2006) and the colors of our average Seyfert 2 host galaxy. The error bars indicate standard deviations in each bin. The bluer filter performance is worse because of the higher ratio of AGN to galaxy light.

assumed a AGN SED power law of $f_\nu^{-0.5}$ as has been found for the optical spectrum of quasars (Richards et al. 2006). We then normalized to the total light in each filter band based off of the $\%PS_r$.

These final modeling results suggest important constraints where GALFIT is effective in removing the AGN light (Figure A.3, lower). Based on these results, we restrict our u band photometry to galaxies with AGN brightnesses of $\%PS_r < 20$ where the contamination is 0.05 ± 0.15 mag. For photometry in the other $griz$ filters, a less stringent restriction of $\%PS_r < 40$ is sufficient to keep our errors within $\sigma = 0.05\pm0.04$ mag.

In addition to our simulations, we also tested the real BAT AGN galaxies for AGN contamination after removing the AGN light measured by GALFIT. The effects of subtracting the AGN contribution with GALFIT are shown for the $u - r$ and $g - r$ for the broad-line AGN in Figure A.4. The galaxy colors stay flat with increasing % of AGN light up to $\approx20\%$ for the u band and $\approx35\%$ for the $griz$ band. This agrees with the results of our modeling of AGN contamination at 20% for the u band and 40% for the $griz$. Based on these results, we have imposed a tighter restriction of 35% AGN light on the $griz$ band photometry to ensure there is no AGN contamination.

We have restricted our color analysis of host galaxies because of our inability to remove the AGN light with GALFIT for the brightest AGN. After fitting with GALFIT, 17 or 10% of galaxies had bright broad-line AGN, where $\%PS_r > 35$, and these galaxies were not included in the $griz$ analysis because of uncertainty of the host galaxy photometry (Figure A.5). When we include both the galaxies that were not included because of pixel saturation and those with with $\%PS_r > 35$, the completeness is 71% for the highest quartile of BAT luminosity and $>95\%$ for the other 3 quartiles. In the u band, 41 galaxies or 23% were excluded because the
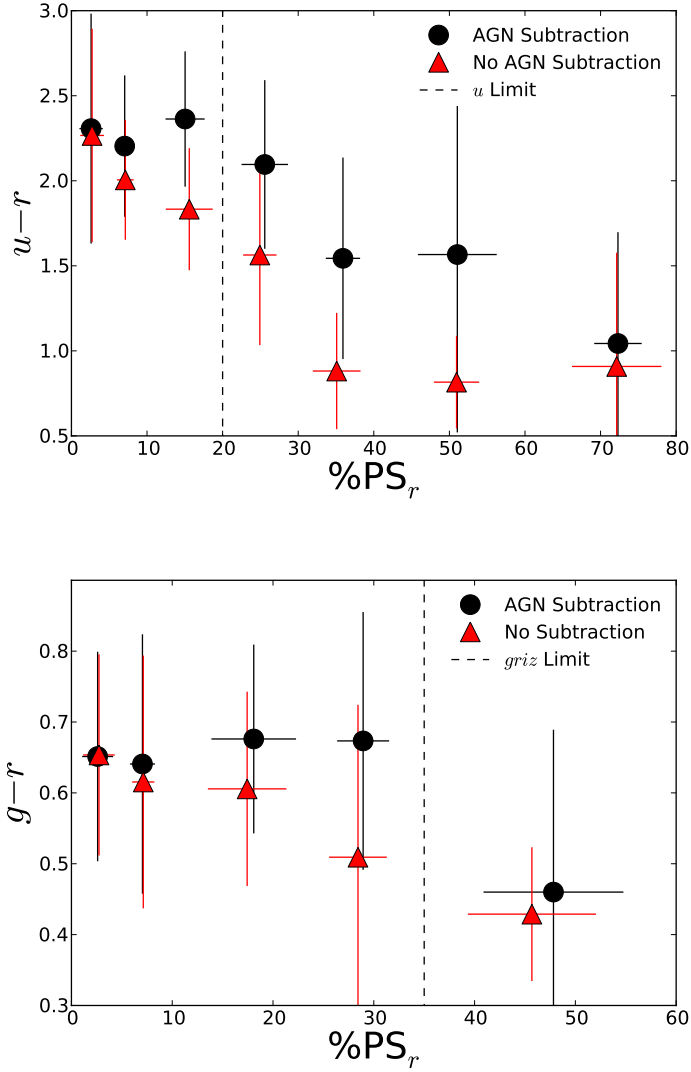
Figure A.4: *Upper Panel*: Average colors in $u - r$ for BAT AGN before and after AGN subtraction with GALFIT. The error bars indicate standard deviations in each bin. Using GALFIT for AGN subtraction, the colors are almost constant for %PS$_r$ <20. Based on our modeling we believe the strong blueward shift above 20% is due to AGN contamination not accounted for from GALFIT. *Lower Panel*: Average colors in $g - r$ for BAT AGN before and after AGN subtraction with GALFIT. The error bars indicate standard deviations in each bin. The ratio of AGN to galaxy light is smaller in g than u and we see a constant color to %PS$_r$ <35.

luminosity of the AGN exceeded 20%. The completeness is 71% for the highest quartile of BAT luminosity and >95% for the other 3 quartiles. This may introduce a small bias against QSO-like systems. However, in the regions where GALFIT is accurate in the removal of the AGN, we do not see any strong trends towards bluer colors in higher luminosity AGN.

Our photometry will be used to provide colors and stellar masses of the host galaxy. Contamination from the AGN will be reduced in relative color measurements, since the photometry from all filters includes light from the AGN and will to some extent be subtracted off in color measurements. Finally, when using photometry to determine stellar masses, the redder bands are weighted more heavily, as they tend to be less contaminated by the AGN component than the bluer bands.

A.2   Comparison Sample

In this section, we discuss considerations in our choice of the comparison sample from the SDSS, the use of catalog photometry, and importance of comparing galaxies with similar brightnesses or stellar masses. We have used galaxies with both photometry and spectroscopy from the SDSS as a comparison sample. Since 50% (93/185) of BAT AGN galaxies are in the SDSS spectroscopic coverage area, we can examine these galaxies to determine the completeness of the SDSS catalog sample. In Figure A.6, the SDSS spectroscopic coverage of BAT AGN by redshift bin is shown. While 70% of the BAT sample in the SDSS has spectroscopic coverage, the brightest galaxies in each redshift bin are missed for z<0.03. Above this redshift a few broad-line AGN with bright nuclei are misclassified as stars. Due to the selection effect against the brightest galaxies, in this study we have chosen a SDSS control sample of galaxies with 0.01<z<0.07.
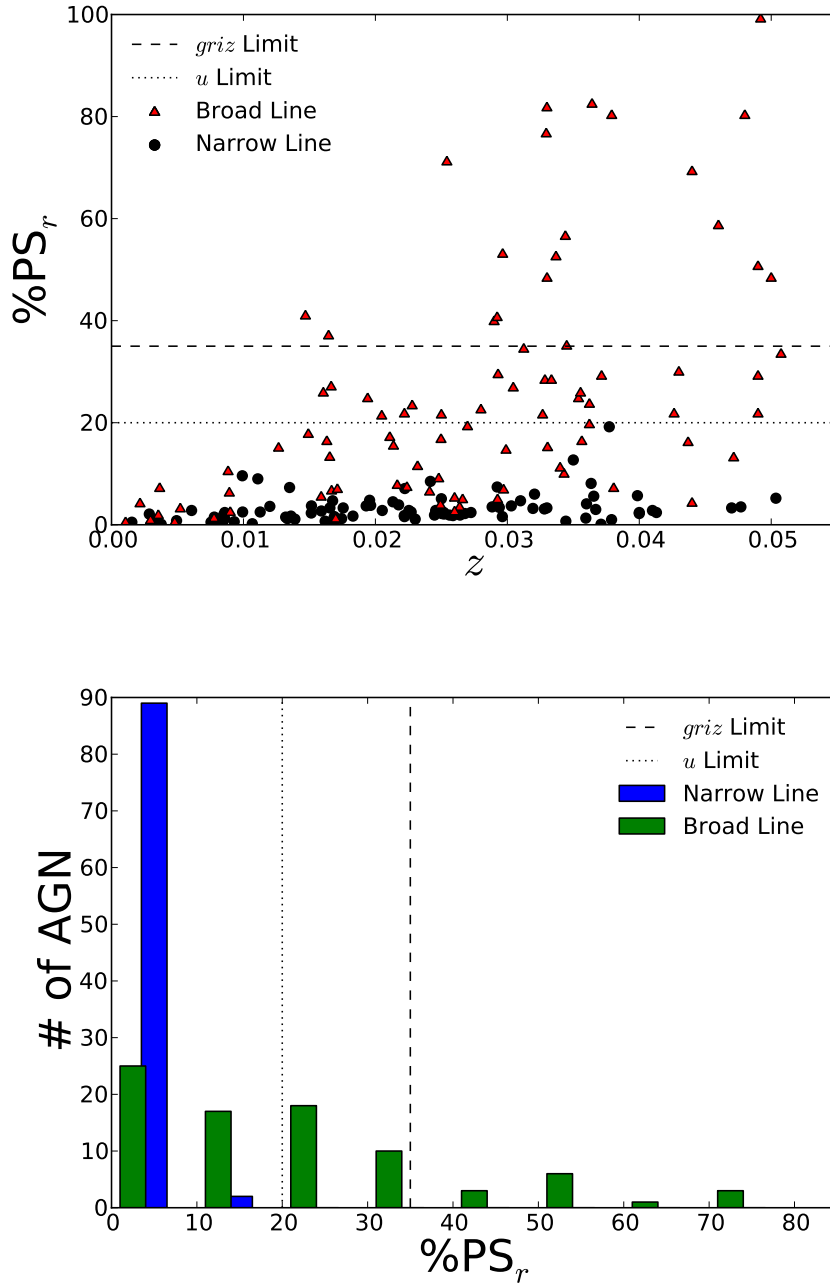
Figure A.5: *Upper Panel*: Plot of $\%PS_r$ for BAT AGN galaxies by redshift. Narrow-line AGN are represented as dots and broad-line AGN are indicated by triangles. Dashed lines indicate the limits above which GALFIT was unable to effectively remove the AGN light. These galaxies were not included in the analysis of colors because of AGN contamination. At higher redshifts we find more BAT AGN with higher ratios of AGN to galaxy light. *Lower Panel*: Plot of number of AGN in bins of $\%PS_r$. We find that GALFIT finds $\%PS_r < 5$ for most BAT narrow-line BAT AGN.
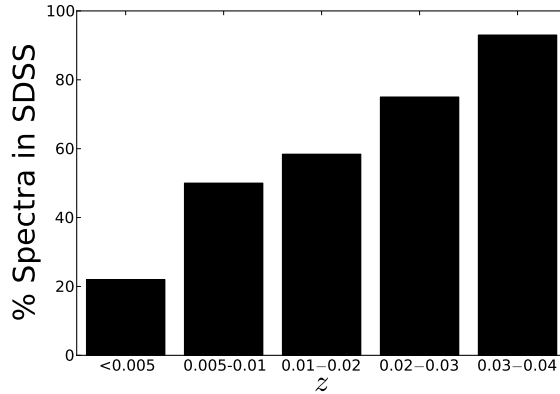
Figure A.6: Percent coverage of BAT AGN in the SDSS spectroscopic footprint with spectroscopy. Due to the brightness limits ($m_r < 15$) in the spectroscopic sample, 30% of the BAT AGN galaxies are missed by the SDSS spectroscopic sample. In addition, some broad-line AGN with bright nuclei are misclassified as stars and not included in the SDSS spectroscopy. Finally, some merging BAT AGN galaxies are not covered because of fiber collision limits in the SDSS. Due to this effect, we have used SDSS galaxies in the redshift range of 0.01<z<0.07 to compare to BAT AGN.

We also ensured that our own photometry of BAT AGN agreed with the SDSS catalog measurements. We can measure the differences between our photometry and those in the SDSS catalog since 62% (116/185) of BAT AGN are in the SDSS photometric catalog (Figure A.7). The SDSS photometric catalog incorrectly shreds (Figure A.8) features of bright, nearby galaxies, such as spiral arms, rings, and dust lanes into different components. This causes a systematic underestimation of the brightness of galaxies and variations in their measured color. Because of this shredding effect, we have restricted our SDSS catalog comparison to galaxies with m_r>13.5 and z>0.01, where we find good agreement in photometry. In Figure A.9, we show a comparison between the $g - r$ of BAT AGN measured in the SDSS catalog and measured using our own photometry. The SDSS catalog colors show better agreement than the photometry since the effects of shredding tend to cancel each other out in relative color measurements.
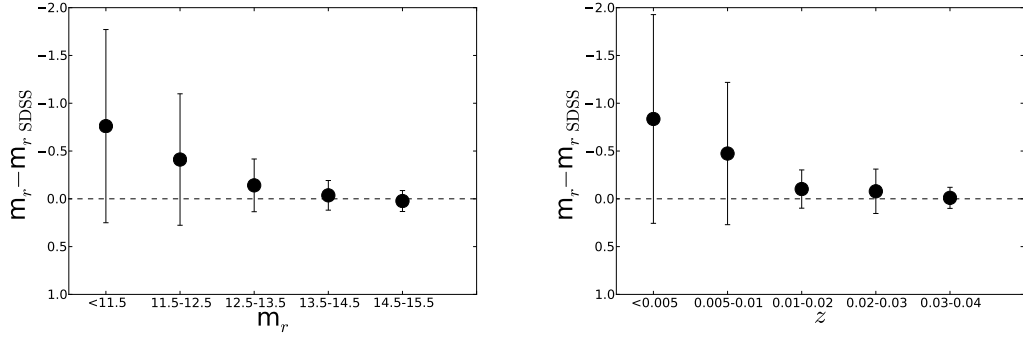
Figure A.7: Comparison of our measured Petrosian magnitudes to the SDSS catalog values for a range of magnitudes (m_r) (*left*) and redshifts (*right*). Negative values indicate we find a brighter magnitude than the SDSS catalog. Since the automated routine in the SDSS has a tendency to shred galaxies into multiple component galaxies, the magnitudes are reduced. This shredding effect is much stronger for the brightest galaxies. However, for $m_r > 13.5$ or $z > 0.01$ the magnitudes are in good agreement. Given these results, we have restricted our SDSS catalog comparison to this range.
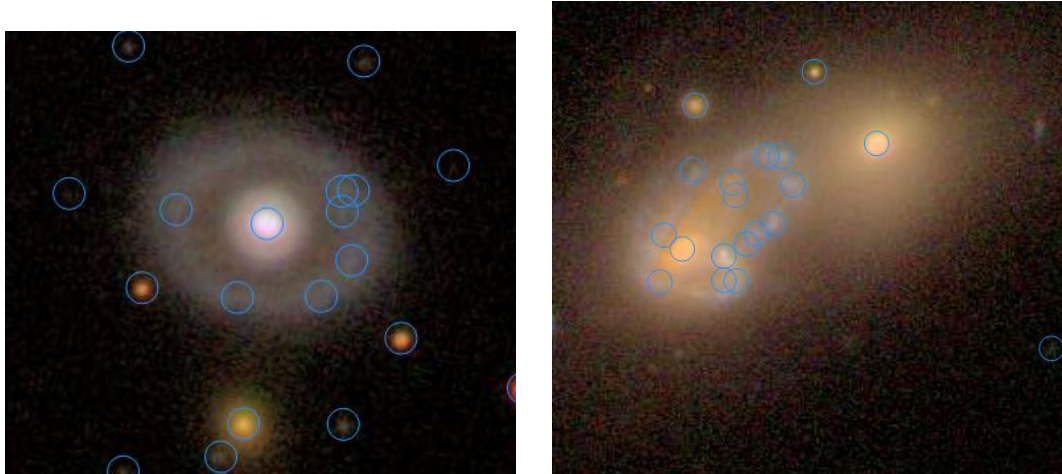
Figure A.8: Example of shredding that occurs with the brighter galaxies in the SDSS for Mrk 705. Each of the blue circles is a unique galaxy or star in the SDSS photometric catalog. The ring structure of Mrk 705 is separated into unique galaxies reducing the brightness measured in the catalog.

124
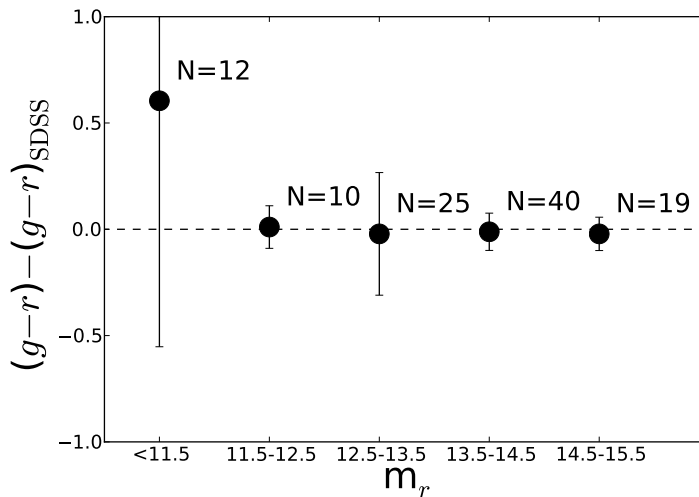
Figure A.9: Comparison of the average difference in $g - r$ color between our measurements and the SDSS catalog. The error bars indicate standard deviations in each bin. The SDSS catalog colors show better agreement than apparent magnitudes since the effects of shredding tend to cancel each other out in the reduced brightness of both filters.

When comparing host galaxy properties, it is important to consider the flux limited nature of both the SDSS and BAT surveys. In Figure A.10, a plot of average M_r by redshift for the BAT AGN, SDSS AGN, and inactive SDSS galaxies is shown. At higher redshifts the SDSS detects AGN and galaxies that are more luminous and have a higher stellar mass because of a selection effect against optically faint galaxies. On the other hand, the BAT AGN survey detects AGN galaxies of a constant optical brightness across a range of redshifts. Due to these selection effects, it is important to compare host galaxy colors between the BAT survey and SDSS survey only at similar brightnesses or stellar masses.
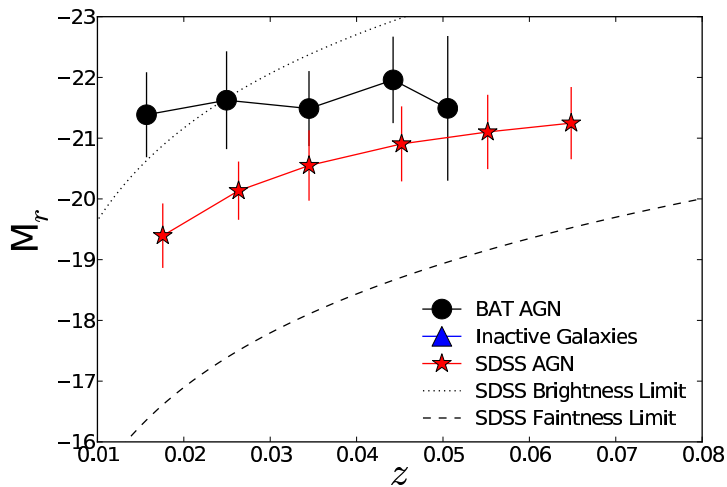
Figure A.10: Plot of average absolute mag in r for the BAT AGN, SDSS AGN, and inactive galaxies. The error bars indicate standard deviations in each bin. The dashed lines indicate the approximate brightness and faintness limits from the SDSS spectroscopic survey. At higher redshifts, the SDSS detects galaxies that are more luminous and have a higher stellar mass because of the selection effect against faint galaxies. On the other hand, the BAT AGN survey detects AGN galaxies of a constant optical brightness across a range of redshifts. Due to the selection effects it is important to compare host galaxy colors between the BAT survey and SDSS survey only at similar brightnesses or stellar masses. For comparison, in the redshift range between 0.03 to 0.05 and the survey coverage area of the SDSS, the BAT survey has 28 broad-line and 17 NL AGN. In this same range, the SDSS has 121 broad-line and 411 Seyfert 2 AGN.

A.3 Selection Effects in the BAT Survey

In the ultra hard X-rays, the BAT survey is also flux limited. Assuming the ultra hard X-ray AGN are distributed randomly following the distribution of luminosities at lower redshifts, and using the limiting sky sensitivity, we can make a further estimate of completeness (Figure A.11). We find that the BAT sources are complete for z<0.05 in this survey for log $L_{14-195\,\mathrm{keV}}$>43.7 or $\approx$log $L_{2-10\,\mathrm{keV}}$>43.2 assuming no intrinsic absorption. In addition, we limited our analysis of morphologies to NL BAT AGN. The completeness fractions are shown in Figure A.12 as a function of
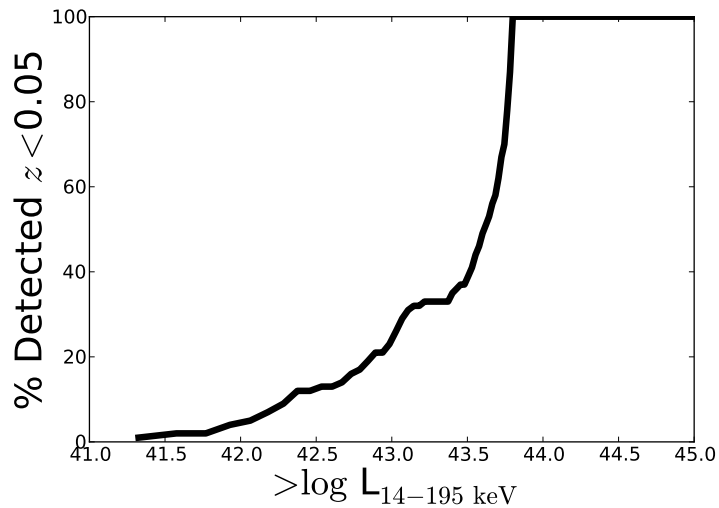
Figure A.11: Plot of estimated completeness above a ultra hard X-ray luminosity within the redshift range of this survey (z<0.05) using the median flux sensitivity of the 58 month survey (1.1×10^{-11} erg cm^{-2} s^{-1}; Baumgartner et al. 2010, submitted). This plot assumes the ultra hard X-ray AGN are randomly distributed by volume and uses the distribution of lower redshift sources to estimate those missed at higher redshift. We find that the BAT sources are complete for z< 0.05 in this survey for log $L_{14-195\,keV} > 43.7$ or $\approx$log $L_{2-10\,keV} > 43.2$ assuming no intrinsic absorption.

ultra hard X-ray luminosity. We see that the highest luminosity quartile for BAT luminosity is less complete than the lowest quartile, although this difference is <20%.

In addition, the BAT survey may miss heavily obscured Compton-thick sources that may be identified using methods at other wavelengths. Compton-thick sources are AGN where our line of sight to the source is blocked with obscuring matter that has an optical depth of $\tau > 1$ ($N_H > 1.5 \times 10^{24}$ cm^{-2}). At these optical depths, much of the X-ray emission is reflected and not direct. For Compton-thick sources, the column densities are so high that little to no direct emission escapes below 10 keV. Estimates of the number of Compton-thick sources in the BAT AGN sample have ranged from 3% to 20% (Ajello et al. 2008; Tueller et al. 2008; Winter et al. 2009). A recent analysis of the *INTEGRAL* AGN at 20–40 keV finds that the
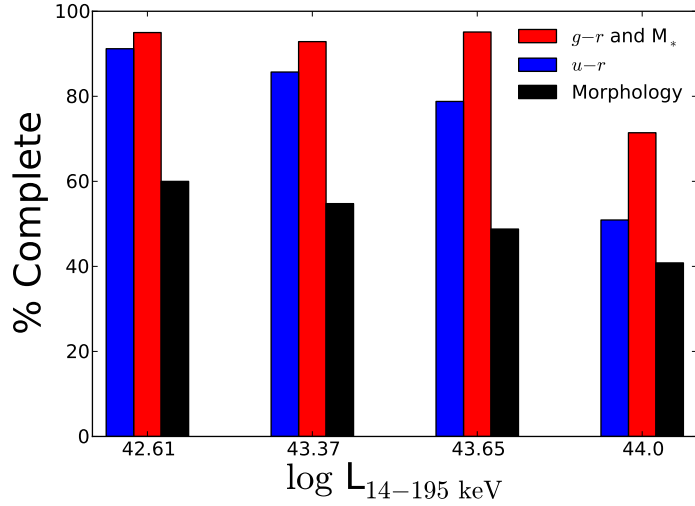
Figure A.12: Completeness of various measurements at each quartile of BAT luminosity. Morphology measurements were limited to narrow-line AGN while color measurements exclude systems with very bright AGN. The highest quartile of BAT luminosity is less complete than the lowest quartile, although this difference is $<20\%$.
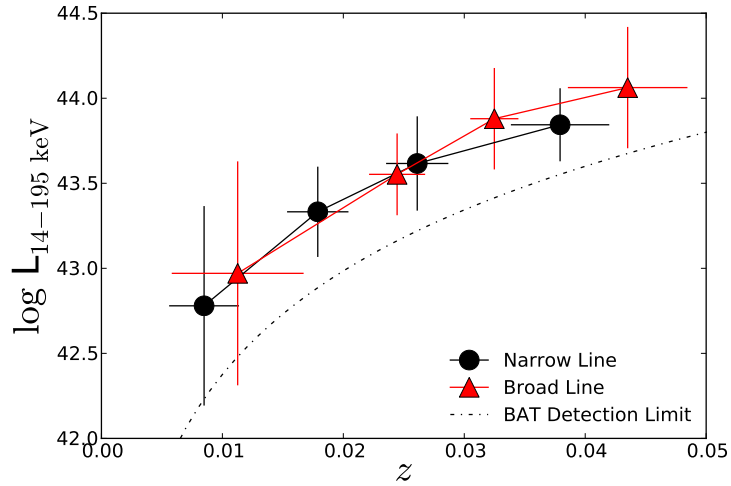
Figure A.13: Plot of average ultra hard X-ray luminosity compared to redshift for narrow-line and broad-line AGN in BAT. The error bars indicate standard deviations in each bin. The dashed line shows the approximate flux limit of the BAT survey. This shows that the BAT survey does have a slight tendency to find narrow-line AGN at closer redshifts than broad-line AGN. The mean redshift is 0.027 for broad-line sources and 0.022 for narrow-line sources. The mean log $L_{14-195\,keV}$ for broad-line sources is 43.56 ± 0.65 and 43.37 ± 0.59.

number of Compton-Thick AGN found by optical and ultra hard X-ray methods is in agreement up to z=0.015 (Malizia et al. 2009).

We independently estimated the number of missing Compton-thick sources by investigating the difference in narrow and broad-line sources by redshift. A plot of average ultra hard X-ray luminosity compared to redshift for narrow-line and broad-line AGN in the BAT survey can be found in Figure A.13. We have also plotted the approximate all-sky limiting flux of the BAT ultra hard X-ray detections for the 58 month catalog. This shows that the BAT survey does have a slight tendency to find narrow-line AGN at closer redshifts than broad-line AGN. The mean redshift is 0.027 for broad-line sources and 0.022 for narrow-line sources. The mean log $L_{14-195\,keV}$ is 43.56±0.65 for broad-line sources and is 43.37±0.59 for the narrow-line sources.

An additional way to estimate the number of missed absorbed sources is by measuring the percentage of NL BAT AGN by redshift (Figure A.14). We find that the number of narrow-line sources falls at higher redshifts. For z<0.01, 61% are NL AGN while at 0.03<z<0.05 only 31% are NL AGN. If we assume that the ratio of 61% narrow-line AGN in the z<0.01 bin is the true value and is constant with redshift, then we will be missing about 50 narrow-line sources at higher redshift or 27% of the entire sample. However, we do not find any statistically significant difference in color between NL and broad-line AGN or between luminous (log $L_{14-195\,keV}$>43.5) and less luminous sources. We also do not find any statistically significant difference with increasing X-ray column densities. These results suggest that the flux-limited nature of the survey does not strongly influence our overall results.

We can make an additional estimate of the number of missing Compton-thick AGN based on the ratio of NL to broad-line AGN in the SDSS survey. In the redshift range between 0.03 to 0.05, the SDSS has 121 broad-line AGN and 411 NL AGN. For comparison, the BAT survey has 28 broad-line AGN and 17 NL AGN in
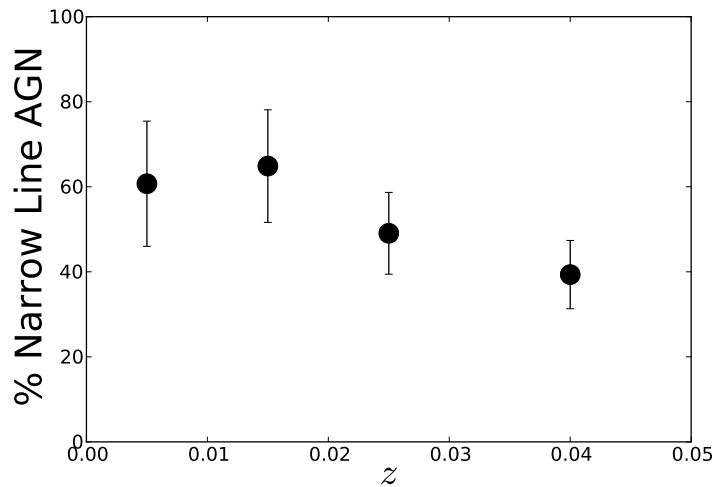
Figure A.14: Percent of narrow-line sources in different redshift ranges in the BAT AGN sample. The error bars represent 1σ Poisson statistics. We find that the number of narrow-line sources falls at higher redshifts. For z<0.01, 61% are NL AGN while at 0.03<z<0.05 only 31% are NL AGN. If we assume that the ratio of 61% narrow-line AGN is constant across redshift, we will be missing about 50 narrow-line sources at higher redshift or 27% of the entire sample.

this range. This suggests that approximately 77% (411/532) are narrow-line, which is greater than the 61% of NL BAT AGN at low redshift, but not outside of the 1 sigma error bars for z<0.02. We may therefore estimate that at a maximum $\approx$16% AGN are missed as Compton-thick. Unless a large fraction of the missed sources have systematically different colors, morphologies or mass than the detected sources we do not expect a large effect on our results.

Table A.1: Kitt Peak Observations

Name	Date	Type[1]	z	Dis[2]	E(B-V)[3]	Air[4]	PSF[5]
				Mpc	mag		″
1RXS J045205.0+493248	2008-02-07	Sy1	0.029	125.3	0.72	1.1	1.2
2MASX J00253292+6821442	2008-11-06	Sy2	0.012	51.2	1.04	1.2	2.5
2MASX J04440903+2813003	2008-02-08	Sy2	0.011	48	0.85	1.1	1.0
2MASX J05054575-2351139	2008-11-06	Sy2	0.035	151.9	0.03	1.7	1.5
2MASX J06411806+3249313	2008-02-09	Sy2	0.047	205.8	0.15	1.0	1.0
2MASX J09043699+5536025	2008-02-13	Sy1	0.037	161.4	0.02	1.1	1.2
2MASX J09112999+4528060	2008-02-12	Sy2	0.026	115.5	0.01	1.0	1.4
2MASX J11454045-1827149	2008-02-06	Sy1	0.032	142.7	0.03	1.6	1.4
2MASX J12005792+0648226	2008-02-10	Sy2	0.035	156.1	0.01	1.2	0.9
2MASX J21355399+4728217	2008-11-07	Sy1	0.025	107.6	0.62	1.0	1.0
2MFGC 02280	2008-02-14	G	0.015	64.8	0.77	1.7	2.1
3C 111.0	2008-02-08	Sy1	0.048	210.3	1.65	1.0	0.8
3C 120	2008-11-05	Sy1	0.033	143	0.29	1.3	1.5
Ark 120	2008-02-11	Sy1	0.033	146	0.12	1.2	1.1
ARK 347	2008-02-09	Sy2	0.022	96.9	0.03	1.0	0.8
ARP 102B	2008-02-13	Sy1	0.024	104	0.02	1.3	1.1
CGCG 420-015	2008-02-10	Sy2	0.029	127	0.08	1.2	0.9
ESO 490-IG026	2008-02-10	Sy1.2	0.024	106.8	0.09	2.0	1.3
ESO 506-G027	2008-02-11	Sy2	0.025	107.7	0.07	1.9	1.3
ESO 511-G030	2008-02-09	Sy1	0.022	96.2	0.06	1.9	1.9
FAIRALL 272	2008-02-10	Sy2	0.022	95.4	0.04	1.2	1.0
HB89 0241+622	2008-11-07	Sy1	0.044	192.2	0.72	1.2	1.2
IC 4329A	2008-02-10	Sy1	0.016	68.7	0.05	2.1	1.4
IGR J21277+5656	2008-09-06	Sy1	0.014	62.8	1.3	1.1	1.2
IRAS 04124-0803	2008-02-13	Sy1	0.037	164.9	0.08	1.3	1.4
IRAS 05218-1212	2008-02-13	Sy1	0.049	214.8	0.16	1.4	1.5
IRAS 05589+2828	2008-02-08	Sy1	0.033	143	0.42	1.2	1.0
LEDA 138501	2008-02-11	Sy1	0.049	215.8	0.16	1.1	1.4
LEDA 214543	2008-02-13	Sy2	0.032	138.8	0.11	1.2	1.3
MCG -01-05-047	2008-11-07	Sy2	0.016	72.2	0.02	1.2	1.3
MCG -01-13-025	2008-02-09	Sy1.2	0.015	68	0.03	1.3	1.2
MCG -01-24-012	2008-02-06	Sy2	0.019	84.2	0.03	1.3	1.7
MCG -01-40-001	2008-02-12	Sy2	0.022	97.6	0.08	1.3	2.1
MCG -02-12-050	2008-02-10	Sy2	0.036	157.9	0.07	1.4	0.9

Continued on Next Page. . .

131

Name	Date	Type[1]	z	Dis[2]	E(B-V)[3]	Air[4]	PSF[5]
				Mpc	mag		$''$
MCG -03-34-064	2008-02-06	Sy1.8	0.016	70.8	0.07	1.5	1.4
MCG -05-14-012	2008-11-06	Sy2	0.009	42.2	0.12	1.9	1.5
MCG -05-23-016	2008-02-11	Sy2	0.008	36.1	0.10	2.2	1.4
MCG +04-22-042	2008-02-12	Sy1.2	0.032	141.5	0.04	1.0	1.6
MCG +04-48-002	2008-09-08	Sy2	0.013	59.3	0.44	1.1	1.1
MCG +08-11-011	2008-11-04	Sy1.5	0.020	87.9	0.21	1.0	0.8
Mrk 10	2008-02-09	Sy1.2	0.029	126.4	0.04	1.2	1.1
Mrk 1018	2008-09-06	Sy1.5	0.042	186.1	0.12	1.2	1.0
Mrk 18	2008-02-09	Sy1	0.011	47.2	0.04	1.2	1.0
Mrk 279	2008-02-07	Sy1.5	0.030	131.7	0.01	1.2	1.3
Mrk 335	2008-11-07	Sy1.2	0.025	109.5	0.02	1.0	1.6
Mrk 348	2008-11-07	Sy2	0.015	64.7	0.06	1.0	1.7
Mrk 352	2008-11-07	Sy1	0.014	63.7	0.06	1.1	1.6
Mrk 417	2008-02-08	Sy2	0.032	142.1	0.02	1.0	0.9
Mrk 509	2008-09-05	Sy1.2	0.034	149.2	0.05	1.5	1.4
Mrk 520	2008-11-04	Sy1.9	0.026	114.7	0.05	1.0	1.0
Mrk 590	2008-02-12	Sy1.2	0.026	113.7	0.03	1.3	1.7
Mrk 79	2008-11-07	Sy1.2	0.022	95.4	0.07	1.0	1.2
Mrk 915	2008-09-05	Sy1	0.024	103.7	0.06	1.4	1.6
NGC 1142	2008-02-13	Sy2	0.028	124.6	0.07	1.2	1.4
NGC 1275	2008-02-12	Sy2	0.017	75.2	0.03	1.2	1.5
NGC 2110	2008-02-06	Sy2	0.007	33.1	0.37	1.6	1.8
NGC 2992	2008-11-06	Sy2	0.007	30.5	0.06	1.8	1.3
NGC 3081	2008-02-10	Sy2	0.007	32.5	0.05	1.7	1.0
NGC 3227	2008-02-08	Sy1.5	0.003	20.9	0.02	1.0	0.8
NGC 3281	2008-02-11	Sy2	0.010	45.4	0.16	2.6	1.4
NGC 3516	2008-02-07	Sy1.5	0.008	38.9	0.04	1.3	1.6
NGC 4102	2008-02-12	LINER	0.002	21	0.02	1.0	2.1
NGC 4593	2008-02-08	Sy1.9	0.009	44	0.02	1.2	1.4
NGC 5728	2008-02-08	Sy2	0.009	29.1	0.10	1.5	1.4
NGC 5995	2008-02-11	Sy2	0.025	108.5	0.15	1.4	1.8
NGC 6240	2008-02-14	Sy2	0.024	105.4	0.07	1.3	2.0
NGC 6814	2008-09-05	Sy1.5	0.005	22.8	0.18	1.4	1.2
NGC 7314	2008-11-06	Sy1.9	0.004	19	0.02	1.9	2.0
NGC 7319	2008-09-08	Sy2	0.022	95.3	0.07	1.1	1.0

Continued on Next Page. . .

Table A.1 – Continued

Name	Date	Type[1]	z	Dis[2]	E(B-V)[3]	Air[4]	PSF[5]
				Mpc	mag		"
NGC 7469	2008-11-05	Sy1.2	0.016	69.8	0.06	1.3	2.5
NGC 7679	2008-09-06	Sy1	0.017	73.4	0.06	1.1	1.4
NGC 7682	2008-11-07	Sy2	0.017	73.1	0.06	1.1	1.3
NGC 788	2008-11-06	Sy2	0.013	58	0.02	1.3	1.2
NGC 931	2008-02-10	Sy1.5	0.016	71.2	0.09	1.1	0.9
NGC 973	2008-11-05	Sy2	0.016	69.2	0.09	1.2	1.6
RX J2044.0+2833	2008-11-06	Sy1	0.05	219.4	0.03	1.2	1.7
SBS 1301+540	2008-02-12	Sy1	0.029	129.2	0.02	1.0	1.5
UGC 02724	2008-11-07	Sy2	0.047	209	0.20	1.1	1.3
UGC 03142	2008-02-09	Sy1	0.021	93	0.74	1.0	1.1
UGC 03601	2008-02-09	Sy1.5	0.017	73.3	0.08	1.0	0.9
UGC 12282	2008-09-07	Sy1.9	0.016	72.7	0.14	1.0	1.3
UGC 12741	2008-09-08	G	0.017	74.7	0.10	1.1	2.4

[1]AGN type and host galaxy type from Tueller et al. (2008). For AGN types, optical identifications are listed, where available. Where G is indicated, there are no optical emission lines indicative of the presence of an AGN and the optical spectrum looks like a galaxy spectrum.

[2]We used the mean of the redshift independent distance in Mpc from NED when available. Otherwise, we adopted the following cosmological parameters to determine distances: $\Omega_{\mathrm{m}} = 0.27$, $\Omega_{\Lambda} = 0.73$, and $H_0 = 71$ km s^{-1} Mpc^{-1}.

[3]Milky Way reddening values, E(B-V), from *IRAS* and *COBE/DIRBE*.

[4]Median airmass of all five filter observations.

[5]Gaussian FWHM of r band image.

Table A.2: SDSS Observations

Name	Date	Type [1]	z	Dis[2] Mpc	E(B-V)[3] mag	Air[4]	PSF[5] ″
2MASX J01064523+0638015	2005-09-28	Sy2	0.041	178.7	0.05	1.1	1.0
2MASX J03305218+0538253	2004-12-14	Sy1	0.046	201.3	0.37	1.1	1.7
2MASX J03534246+3714077	2003-01-28	Sy2	0.018	78.4	0.53	1.0	0.9
2MASX J07595347+2323241	2003-01-25	Sy2	0.029	128	0.05	1.4	1.4
2MASX J16174158+0607100	2003-04-25	Sy2	0.037	164.8	0.08	1.1	0.9
ARP 151	2002-04-01	Sy1	0.021	90.5	0.02	1.2	1.5
CGCG 031-072	2002-03-05	Sy1	0.033	143.2	0.03	1.2	1.8
CGCG 046-033	2001-04-16	Sy1.5	0.034	148.7	0.03	1.2	1.2
CGCG 102-048	2005-05-09	Sy1.9	0.026	116	0.03	1.1	1.2
CGCG 122-055	2004-12-13	Sy1	0.021	91.8	0.03	1.0	1.1
CGCG 198-020	2006-05-24	Sy1	0.026	112	0.04	1.2	1.6
CGCG 300-062	2001-09-20	Sy2	0.032	143	0.05	1.3	0.9
CGCG 312-012	2003-10-24	Sy2	0.025	110.3	0.04	1.3	1.5
CGCG 319-007	2004-06-15	Sy1.9	0.044	192.2	0.04	1.2	1.3
CGCG 427-028	2006-05-27	G	0.030	131	0.20	1.3	1.7
IC 0486	2002-01-14	Sy1.8	0.027	117.5	0.03	1.1	1.1
IC 0751	2003-04-01	Sy2	0.030	134.1	0.03	1.2	1.4
IC 2461	2002-11-07	Sy2	0.007	72.9	0.01	1.1	1.4
IC 2515	2003-03-07	Sy2	0.019	82.7	0.02	1.0	1.1
KAZ 320	2006-09-18	Sy1	0.034	149.6	0.15	1.6	1.6
KUG 1141+371	2004-01-31	Sy1	0.038	165.5	0.02	1.0	1.4
KUG 1208+386	2004-01-31	Sy1	0.022	98	0.03	1.0	1.6
LEDA 170194	2006-01-31	Sy2	0.036	159.4	0.04	1.4	1.4
M106	2003-03-06	LINER	0.001	7.5	0.01	1.3	1.3
MCG -02-08-014	1999-10-14	G	0.016	71.7	0.05	1.8	1.8
MCG +01-57-016	2005-09-26	Sy1.8	0.024	107.5	0.12	1.1	1.2
MCG +02-21-013	2005-03-10	Sy2	0.034	149.3	0.03	1.0	1.4
MCG +04-06-043	2005-11-04	Sy1	0.033	144.5	0.21	1.2	1.3
MCG +05-28-032	2004-12-15	LINER	0.023	99	0.02	1.1	1.3
MCG +06-24-008	2004-02-17	Sy2	0.025	111.5	0.02	1.0	1.2
MCG +06-49-019	2006-09-16	Sy2	0.021	91.6	0.17	1.0	1.3
MCG +11-11-032	2003-11-20	Sy2	0.036	156.3	0.15	1.3	1.3
MCG+10-17-061	2001-04-15	G	0.009	42.3	0.02	1.1	1.5
MRK 1044	1999-10-14	Sy1.8	0.016	70.4	0.05	1.5	1.5

Continued on Next Page. . .

Name	Date	Type[1]	z	Dis[2]	E(B-V)[3]	Air[4]	PSF[5]
				Mpc	mag		"
Mrk 110	2001-02-22	Sy1	0.035	153.6	0.01	1.2	1.2
Mrk 1210	2003-01-28	Sy1	0.013	57.6	0.02	1.0	1.0
Mrk 1392	2001-03-19	Sy1	0.036	157.3	0.04	1.5	1.5
Mrk 1469	2002-02-08	Sy1	0.030	134.1	0.03	1.0	1.3
Mrk 198	2003-03-06	Sy2	0.024	105.8	0.01	1.3	1.3
Mrk 268	2004-04-25	Sy2	0.039	173.6	0.02	1.1	1.3
Mrk 290	2001-03-23	Sy1	0.029	128.1	0.01	1.5	1.5
Mrk 463E	2005-05-09	Sy2	0.050	221	0.04	1.1	1.0
Mrk 464	2004-01-28	Sy1.5	0.050	222.8	0.02	1.0	1.0
Mrk 477	2002-05-09	Sy2	0.037	164	0.01	1.1	1.7
Mrk 50	2000-05-05	Sy1	0.023	99.7	0.01	1.3	1.3
Mrk 595	2005-10-12	Sy1.5	0.026	116.4	0.17	1.2	1.1
Mrk 704	2005-03-12	Sy1.5	0.029	126.3	0.02	0.9	0.9
Mrk 705	2006-01-31	Sy1.2	0.028	120.8	0.04	1.2	1.2
Mrk 728	2003-03-23	Sy1	0.035	154.7	0.03	1.3	1.5
Mrk 732	2002-12-11	Sy1.8	0.029	126.3	0.03	1.2	1.5
Mrk 739E	2005-03-10	Sy1	0.029	128.4	0.03	1.0	1.5
Mrk 766	2004-12-15	Sy1.5	0.012	54	0.01	1.2	1.2
Mrk 78	2004-12-13	Sy2	0.037	158.1	0.05	1.2	1.2
Mrk 817	2001-05-18	Sy1.5	0.031	135.2	0.00	1.7	1.7
Mrk 841	2003-04-25	Sy1	0.036	158.2	0.02	1.4	1.4
Mrk 926	2000-09-03	Sy1.5	0.047	206.5	0.04	1.4	1.4
NGC 0835	2000-09-26	Sy2	0.013	56.3	0.03	1.3	1.5
NGC 1012	2005-12-06	G	0.003	16.2	0.21	1.2	1.3
NGC 1052	1999-10-14	Sy2	0.004	19.6	0.02	1.6	1.6
NGC 1194	2002-09-05	Sy1.8	0.013	56.9	0.07	1.4	1.4
NGC 235A	2006-09-17	Sy2	0.022	95.5	0.01	1.7	1.5
NGC 2885	2004-12-13	Sy1	0.026	112	0.04	1.0	1.1
NGC 3079	2001-04-15	Sy2	0.003	19.3	0.01	1.4	1.4
NGC 3718	2002-01-13	LINER	0.003	17	0.01	1.5	1.5
NGC 3786	2004-05-14	Sy1.8	0.008	41.6	0.03	1.1	1.3
NGC 4051	2003-03-26	Sy1.5	0.002	14.5	0.01	1.2	1.2
NGC 4138	2003-04-25	Sy1.9	0.002	15.6	0.01	1.2	1.2
NGC 4235	2003-04-01	Sy1	0.007	35.1	0.01	1.0	1.0
NGC 4388	2003-03-23	Sy2	0.008	18.25	0.03	1.4	1.4

Continued on Next Page. . .

Table A.2 – Continued

Name	Date	Type[1]	z	Dis[2]	E(B-V)[3]	Air[4]	PSF[5]
				Mpc	mag		″
NGC 4395	2004-04-25	Sy1.8	0.001	4.11	0.01	1.5	1.5
NGC 452	2004-08-26	G	0.016	70.8	0.09	1.0	1.7
NGC 4686	2002-04-01	G	0.016	71.7	0.01	1.3	1.3
NGC 4992	2003-03-31	G	0.025	108.5	0.02	1.3	1.3
NGC 5106	2003-04-28	LINER	0.031	138.3	0.04	1.1	1.1
NGC 513	2004-09-15	Sy2	0.019	83.9	0.06	1.4	1.4
NGC 5231	2000-05-04	Sy2	0.021	93.5	0.03	1.3	1.2
NGC 5252	2001-03-19	LINER	0.022	95.5	0.03	1.4	1.4
NGC 5273	2004-03-17	Sy1.9	0.003	17.7	0.01	1.0	1.0
NGC 5290	2003-04-25	Sy2	0.008	35.7	0.01	1.0	1.6
NGC 5506	2001-05-24	Sy1.9	0.006	28.7	0.05	1.3	1.3
NGC 5548	2004-06-12	Sy1.5	0.016	71.4	0.01	1.3	1.3
NGC 5610	2004-06-13	Sy2	0.016	72.3	0.03	1.0	1.4
NGC 5674	2001-06-16	Sy1.9	0.024	107.3	0.05	1.1	1.4
NGC 5683	2002-05-08	Sy1	0.036	157.3	0.04	1.2	1.5
NGC 5899	2003-04-29	Sy2	0.008	43.9	0.03	1.3	1.3
NGC 5940	2003-04-27	Sy1	0.034	147.4	0.06	1.3	1.2
NGC 7603	2001-10-15	Sy1.5	0.029	126.6	0.04	1.0	1.0
NGC 985	1999-10-14	Sy1	0.043	187.7	0.09	1.5	1.5
SDSS J104326.47+110524.2	2002-12-14	Sy1	0.047	208.4	0.04	1.0	1.3
UGC 03995A	2001-12-18	Sy2	0.015	68	0.04	1.0	1.6
UGC 05881	2005-01-17	Sy2	0.020	88.1	0.04	1.0	1.0
UGC 06527 NED03	2001-12-20	Sy2	0.026	113.9	0.01	1.1	1.1
UGC 07064	2004-12-15	Sy1.9	0.025	107.6	0.02	1.1	1.1
UGC 08327 NED02	2003-03-24	Sy2	0.036	158.8	0.02	1.2	1.5
UGC 11185 NED02	2005-06-08	Sy2	0.041	174.2	0.07	1.1	1.1
UM 614	2000-05-05	Sy1	0.032	142.3	0.02	1.2	1.2

Continued on Next Page...

Table A.2 – Continued

Name	Date	Type[1]	z	Dis[2] Mpc	E(B-V)[3] mag	Air[4]	PSF[5] $''$
VII Zw 073	2004-10-15	Sy2	0.041	180.1	0.12	1.1	1.2

[1]AGN type and host galaxy type from Tueller et al. (2008). For AGN types, optical identifications are listed, where available. Where G is indicated, there are no optical emission lines indicative of the presence of an AGN and the optical spectrum looks like a galaxy spectrum.

[2]We used the mean of the redshift independent distance in Mpc from NED when available. Otherwise, we adopted the following cosmological parameters to determine distances: $\Omega_m = 0.27$, $\Omega_\Lambda = 0.73$, and $H_0 = 71$ km s^{-1} Mpc^{-1}.

[3]Milky Way reddening values, E(B-V), from *IRAS* and *COBE/DIRBE*.

[4]Median airmass of all five filter observations.

[5]Gaussian FWHM of r band image.

Table A.3.   Overlapping SDSS and Kitt Peak Galaxy Colors and Magnitudes

	Mr[1]	u-g[2]	g-r	r-i	i-z	Petrosian Aperture[3]
Kitt Peak-SDSS	-0.11±0.13	0.05±0.16	-0.02±0.035	-0.01±0.02	0.02±0.07	1.2±4.8%

[1]The SDSS website notes that that photometry of the bright galaxies in the SDSS is often underestimated because of an overestimation of sky brightness near them, see Lauer et al. (2007), Bernardi et al. (2007), and Lisker et al. (2007).

[2]The SDSS website also notes that the zeropoint of the u band is somewhat uncertain because of a red leak.

[3]Increased difference in Petrosian aperture size in the r band for Kitt Peak vs. the SDSS.

Table A.4: Photometry and Derived Properties

Galaxy	u^1	g	r	i	z	$\log \mathbf{M}_*{}^2$	$\mathbf{PS}_r{}^3$	$\mathbf{E}(g-r)^4$	$\mathbf{E}(g-r)^5$	u^6	$griz^7$
	mag	mag	mag	mag	mag	$\mathrm{M}_\odot$	%	mag	Inc. mag	Con.	Con.
2MASX J00253292+6821442	...	12.86	12.14	11.85	11.9	10.05	3.59	0.03	...		
2MASX J01064523+0638015	16.9	15.54	14.76	14.27	14.15	10.4	2.75	0.14	0.01		
2MASX J03534246+3714077	15.84	13.99	13.5	13.31	13.18	9.9	1.67	0.21	...		
2MASX J04440903+2813003	...	12.68	11.8	11.4	11.3	10.41	2.51	0.24	...		
2MASX J05054575-2351139	17.31	16.11	15.44	15.12	15.36	9.13	12.7	0.03	...		
2MASX J06411806+3249313	17.9	16.56	15.95	15.56	15.25	9.94	3.25	0.44	...		
2MASX J07595347+2323241	15.44	14.11	13.41	13.02	12.65	10.57	1.59	0.34	0.04		
2MASX J09043699+5536025	17.61	16.25	15.81	15.31	15.16	9.76	29.1	0.62	...	Y	
2MASX J09112999+4528060	17.57	15.98	15.19	14.77	14.54	9.76	2.16	0.27	...		
2MASX J12005792+0648226	15.72	14.68	13.91	13.49	13.34	10.58	1.28	0.17	...		
2MASX J16174158+0607100	18.06	16.24	15.37	14.92	14.60	10.14	0.99	0.31	0.08		
2MASX J21355399+4728217	16.32	14.84	14.12	13.82	14.25	9.41	21.4	0	0.1	Y	
2MFGC 02280	...	14.1	13.26	12.84	12.64	10.13	3.69	0.27	0.09		
ARK 347	16.29	14.5	13.75	13.36	13.10	10.3	2.83	0.34	...		
ARP 102B	17.31	15.05	14.06	13.65	13.37	10.25	8.47	0.14	...		
ARP 151	17.54	16.01	15.08	14.69	14.51	9.71	17.0	0.21	...		
CGCG 031-072	16.94	15.30	14.59	14.19	14.00	10.27	15.1	0.17	...		
CGCG 046-033	16.05	14.90	14.32	14.00	13.96	10.18	9.90	0.03	0.02		
CGCG 102-048	16.81	15.21	14.38	13.91	13.6	10.31	2.46	0.38	0.06		
CGCG 122-055	16.99	15.01	14.32	13.96	13.65	9.94	15.4	0.41	...		

Continued on Next Page...

Table A.4 – Continued

Galaxy	u^1	g	r	i	z	$\log \mathbf{M_*}^2$	$\mathbf{PS}_r{}^3$	$\mathbf{E}(g-r)^4$	$\mathbf{E}(g-r)^5$	u^6	$griz^7$
	mag	mag	mag	mag	mag	$M_\odot$	%	mag	Inc. mag	Con.	Con.
CGCG 198-020	16.34	14.49	13.81	13.39	13.23	10.38	5.24	0.31	$\cdots$		
CGCG 300-062	16.57	15.17	14.56	14.20	14.31	9.9	3.28	0	0.02		
CGCG 312-012	16.35	14.78	13.97	13.59	13.34	10.3	1.94	0.07	$\cdots$		
CGCG 319-007	18.11	15.09	14.35	13.95	13.75	10.63	4.20	1.03	$\cdots$		
CGCG 420-015	15.75	14.13	13.43	13.04	12.71	10.63	3.37	0.34	$\cdots$		
CGCG 427-028	16.42	14.77	13.93	13.49	13.25	10.51	3.69	0.21	$\cdots$		
ESO 490-IG026	15.52	13.45	12.74	12.27	12.32	10.67	8.95	0.31	$\cdots$		
ESO 506-G027	18	14.78	14.12	13.14	14.06	9.84	2.18	0.62	0.07		
ESO 511-G030	14.20	12.72	11.93	11.35	11.11	11.09	7.31	0.51	0.02		
FAIRALL 272	15.53	14.67	13.96	13.57	13.39	10.08	1.58	0.21	$\cdots$		
IC 0486	15.34	13.91	13.21	12.88	12.64	10.61	2.35	0	0.03		
IC 0751	15.44	14.36	13.71	13.31	13.07	10.48	4.65	0.21	0.08		
IC 2461	16.79	14.03	13.36	12.93	12.60	9.54	0.53	0.72	0.09		
IC 2515	15.69	14.54	13.85	13.40	13.15	10.04	3.73	0.38	0.09		
IC 4329A	15.35	13.24	12.40	11.83	11.89	10.53	25.8	0.27	0.08	Y	
KUG 1141+371	$\cdots$	15.69	14.94	14.54	14.46	10.19	7.11	0.14	$\cdots$		
KUG 1208+386	$\cdots$	14.97	14.31	13.88	13.59	10.02	23.3	0.44	$\cdots$	Y	
LEDA 170194	15.05	14.35	13.74	13.40	13.21	10.59	3.01	0.92	0.01		
LEDA 214543	17.6	15.29	14.43	14.05	13.75	10.35	6.02	0.62	$\cdots$		
M106	10.81	8.74	8.11	7.775	7.875	9.95	0.45	0.21	0.06		
MCG -01-05-047	14.89	13.45	12.68	12.2	11.95	10.5	0.02	0.44	0.12		

Continued on Next Page…

Table A.4 – Continued

Galaxy	u^1	g	r	i	z	$\log \mathbf{M}_*^2$	$\mathbf{PS}_r^3$	$\mathbf{E}(g-r)^4$	$\mathbf{E}(g-r)^5$	u^6	$griz^7$
	mag	mag	mag	mag	mag	$M_\odot$	%	mag	Inc. mag	Con.	Con.
MCG -01-13-025	15.23	13.80	13.05	12.68	12.42	10.23	5.39	0.17	$\cdots$		
MCG -01-24-012	16.22	14.33	13.66	13.27	13.12	10.16	3.83	0.31	0.04		
MCG -01-40-001	14.63	13.21	12.56	12.11	12.09	10.66	2.53	0.14	0.06		
MCG -02-08-014	17	14.69	13.9	13.42	13.12	10.01	4.74	0.65	0.11		
MCG -02-12-050	15.32	14.01	13.39	13.02	12.87	10.73	8.09	0.24	$\cdots$		
MCG -03-34-064	15.81	13.65	12.79	12.37	12.2	10.43	13.1	0.44	$\cdots$		
MCG -05-14-012	15.01	13.91	13.28	12.95	12.76	9.66	9.63	0.07	$\cdots$		
MCG -05-23-016	15.73	14.01	13.47	12.72	12.85	9.56	1.92	0.38	$\cdots$		
MCG +01-57-016	15.88	14.17	13.58	13.30	13.23	10.26	16.7	0.14	0.01		
MCG +02-21-013	16.11	14.4	13.68	13.24	13.07	10.68	0.73	0.21	$\cdots$		
MCG +04-06-043	15.53	14.96	14.23	14.07	13.80	10.3	28.3	0	0.01	Y	
MCG +04-22-042	16.62	14.78	14.06	13.61	13.51	10.49	21.4	0.31	0.03	Y	
MCG +04-48-002	15.08	13.45	12.7	12.41	12.22	10.2	1.11	0.14	$\cdots$		
MCG +05-28-032	16.52	15.04	14.23	13.74	13.44	10.14	1.07	0.48	0.04		
MCG +06-24-008	15.7	14.64	13.97	13.56	13.28	10.23	1.83	0.27	0.08		
MCG +06-49-019	15.37	13.58	12.82	12.46	12.30	10.56	4.52	0.31	0.03		
MCG +08-11-011	14.41	12.78	12.04	11.58	11.42	10.91	21.2	0.34	0.02	Y	
MCG +11-11-032	19.09	15.8	14.89	14.39	14.06	10.33	4.13	1.03	0.05		
MCG+10-17-061	14.98	13.43	12.86	12.54	12.33	9.8	2.48	0.21	$\cdots$		
Mrk 10	15.30	13.62	12.97	12.57	12.49	10.73	4.92	0.21	0.05		
Mrk 1018	16.59	14.45	13.65	13.28	13.06	10.92	21.6	0.21	$\cdots$	Y	

Continued on Next Page. . .

Table A.4 – Continued

Galaxy	u^1	g	r	i	z	$\log M_*^2$	PS_r^3	$E(g-r)^4$	$E(g-r)^5$	u^6	$griz^7$
	mag	mag	mag	mag	mag	M$_\odot$	%	mag	Inc. mag	Con.	Con.
Mrk 110	17.19	15.83	15.20	14.89	14.80	9.9	24.6	0	...	Y	
Mrk 1210	14.94	13.97	13.32	13.03	12.82	9.89	7.31	0.31	...		
Mrk 1392	16.07	14.41	13.80	13.39	13.05	10.64	19.5	0.68	0.04		
Mrk 1469	16.88	15.48	14.64	14.22	13.95	10.22	8.79	0.24	...		
Mrk 18	15.19	14.07	13.44	13.16	12.87	9.57	8.95	0.07	...		
Mrk 198	16.03	14.64	14.02	13.69	13.45	10.12	2.83	0.14	0.01		
Mrk 268	15.88	14.58	13.88	13.49	13.19	10.64	5.70	0.17	...		
Mrk 279	15.24	14.48	13.74	13.35	13.16	10.49	26.7	0.31	...	Y	
Mrk 348	14.8	13.29	12.59	12.1	12.1	10.33	2.33	0.14	0		
Mrk 352	...	14.94	14.27	13.92	13.73	9.65	17.7	0.14	...		
Mrk 417	16.87	15.32	14.65	14.27	14.01	10.2	3.13	0.31	...		
Mrk 463E	15.58	14.36	14.04	13.65	13.55	10.61	5.24	0.44	...		
Mrk 464	...	16.92	16.44	16.15	15.94	9.67	33.4	0.31	...	Y	
Mrk 477	15.97	14.78	14.73	14.45	14.34	9.87	19.2	0.24	...		
Mrk 50	17.07	15.41	14.69	14.32	14.01	9.9	11.3	0.27	...		
Mrk 520	15.19	14.14	13.52	13.18	13.00	10.4	4.92	0.14	0.03		
Mrk 590	15.76	13.29	12.66	12.20	12.13	10.84	3.40	0.58	...		
Mrk 595	16.07	14.75	14.07	13.72	13.50	10.3	19.2	0.14	...		
Mrk 705	15.17	14.85	14.22	13.86	13.57	10.18	22.4	0.41	...	Y	
Mrk 728	17.99	15.87	15.19	14.79	14.42	10.09	16.2	0.58	...		
Mrk 732	15.15	13.89	13.33	13.03	12.85	10.48	7.37	0.17	...		

Continued on Next Page. . .

Table A.4 – Continued

Galaxy	u^1	g	r	i	z	$\log \mathbf{M_*}^2$	$\mathbf{PS}_r{}^3$	$\mathbf{E}(g-r)^4$	$\mathbf{E}(g-r)^5$	u^6	$griz^7$
	mag	mag	mag	mag	mag	$M_\odot$	%	mag	Inc. mag	Con.	Con.
Mrk 739E	15.17	14.12	13.86	13.16	12.88	10.47	6.79	0.68	⋯		
Mrk 766	14.91	13.50	12.95	12.59	12.37	10.02	14.9	0.31	0.01		
Mrk 78	16.56	14.73	14.28	13.87	13.68	10.42	0.11	0.44	⋯		
Mrk 79	15.02	13.52	12.81	12.45	12.14	10.57	21.6	0.34	0.01	Y	
Mrk 817	16.38	14.61	13.92	13.61	13.47	10.41	34.3	0.07	0.01	Y	
Mrk 915	15.63	14.17	13.43	13.09	12.86	10.43	6.42	0	0.06		
Mrk 926	16.24	14.66	13.78	13.45	13.37	10.82	13.0	0.14	0.01		
NGC 0835	13.91	12.62	11.94	11.56	11.31	10.48	1.51	0.21	⋯		
NGC 1012	12.78	12.16	11.72	11.46	11.24	9.18	0.11	0.79	0.04		
NGC 1052	12.82	11.14	10.35	9.924	9.680	10.35	0.83	0.27	⋯		
NGC 1142	14.08	13.13	12.44	12.08	11.76	10.93	3.53	1.03	⋯		
NGC 1194	15.24	13.19	12.45	12.00	11.93	10.32	1.23	0.38	⋯		
NGC 1275	12.8	11.7	11.03	10.65	10.71	10.94	3.25	0	⋯		
NGC 2110	13.89	11.25	10.43	10.01	9.94	10.63	1.45	0.68	⋯		
NGC 235A	15	13.71	13.02	12.64	12.40	10.49	7.11	0.21	⋯		
NGC 2885	15.85	14.26	13.47	13.03	12.80	10.56	2.46	0.31	0.02		
NGC 2992	13.59	12.08	11.37	10.95	10.71	10.31	0.00	0.27	⋯		
NGC 3079	11.91	10.97	10.34	9.926	9.703	9.98	0.09	1.03	0.11		
NGC 3081	13.84	12.19	11.51	11.07	10.85	10.31	0.32	0.34	0.02		
NGC 3227	13.49	11.60	10.76	10.18	9.965	9.98	7.11	0.51	⋯		
NGC 3281	14.59	12.83	12.41	11.76	11.24	10.24	0.20	0.82	0.04		

Continued on Next Page. . .

Table A.4 – Continued

Galaxy	u^1	g	r	i	z	$\log \mathbf{M_*}^2$	$\mathbf{PS}_r{}^3$	$\mathbf{E}(g-r)^4$	$\mathbf{E}(g-r)^5$	u^6	$griz^7$
	mag	mag	mag	mag	mag	$\mathrm{M_\odot}$	%	mag	Inc. mag	Con.	Con.
NGC 3516	14.23	12.22	11.39	10.93	10.77	10.46	10.3	0.44	$\cdots$		
NGC 3718	12.87	11.11	10.41	9.990	9.759	9.98	0.89	0.34	0.05		
NGC 3786	13.85	12.86	12.20	11.83	11.40	10.01	6.19	1.03	$\cdots$		
NGC 4051	12.04	10.78	10.26	9.996	9.847	9.44	4.09	0	0.02		
NGC 4102	13.13	11.45	10.73	10.32	9.990	9.68	2.07	0.38	0.05		
NGC 4138	13.35	11.68	10.97	10.58	10.40	9.61	0.77	0.17	0.03		
NGC 4235	14.12	12.12	11.36	10.93	10.66	10.36	1.20	0.44	0.09		
NGC 4388	12.64	11.33	10.72	10.35	10.04	10.53	0.03	0.31	0.1		
NGC 4395	11.40	10.52	10.22	10.08	10.11	8.28	0.39	0.03	0.01		
NGC 452	14.75	13.38	12.59	12.15	11.89	10.48	3.25	0.27	0.08		
NGC 4593	14.48	11.48	10.74	10.24	10.09	10.75	2.35	0.79	0.02		
NGC 4686	14.59	13.01	12.18	11.75	11.45	10.68	0.81	0.24	$\cdots$		
NGC 4992	15.51	13.9	13.17	12.70	12.53	10.64	2.12	0.27	$\cdots$		
NGC 5106	15.81	14.21	13.53	13.13	12.83	10.59	3.22	0.34	$\cdots$		
NGC 513	14.74	13.41	12.74	12.41	12.13	10.44	4.83	0.1	$\cdots$		
NGC 5231	15.33	13.74	13.03	12.65	12.42	10.51	3.94	0.24	0.04		
NGC 5252	$\cdots$	13.47	12.73	12.35	11.95	10.59	1.67	0.24	$\cdots$		
NGC 5273	14.72	12.10	11.38	11.03	10.77	9.64	1.75	1.03	$\cdots$		
NGC 5290	13.41	12.42	11.65	11.18	10.96	10.23	1.24	0.31	0.08		
NGC 5506	15.21	12.39	11.66	11.24	10.91	10.02	2.83	0.75	$\cdots$		
NGC 5548	14.49	13.08	12.48	12.09	11.95	10.46	6.60	0.24	0.01		

Continued on Next Page. . .

Table A.4 – Continued

Galaxy	u[1]	g	r	i	z	log M*[2]	PS_r[3]	E(g−r)[4]	E(g−r)[5]	u[6] Con.	griz[7] Con.
	mag	mag	mag	mag	mag	M☉	%	mag	Inc. mag		
NGC 5610	14.71	13.29	12.71	12.39	12.09	10.28	1.58	0.24	0.07		
NGC 5674	14.10	13.13	12.70	12.35	12.15	10.57	3.80	0.51	0		
NGC 5683	16.66	15.44	14.73	14.44	14.25	10.22	23.5	0.07	…	Y	
NGC 5728	13.69	11.44	10.73	10.27	10.05	10.78	0.60	0.58	0.03		
NGC 5899	13.56	12.18	11.47	11.11	10.84	10.28	2.37	0.1	0.05		
NGC 5940	16.23	13.91	13.47	13.14	13.16	10.47	11.0	0.38	0		
NGC 5995	16.62	15.42	14.67	14.38	14.21	9.89	2.44	0	…		
NGC 6240	15.32	13.11	12.21	11.66	11.54	11.03	1.88	0.55	…		
NGC 6814	12.36	11.05	10.41	10.01	9.840	10.3	3.10	0.27	0		
NGC 7314	12.28	11.21	10.61	10.28	10.10	10.06	0.38	0.1	0.05		
NGC 7319	14.58	13.5	12.75	12.37	12.16	10.61	1.75	0.17	…		
NGC 7469	13.72	12.95	12.39	11.86	11.58	10.49	16.2	1.03	…		
NGC 7603	13.98	13.28	12.66	12.19	11.82	10.94	29.3	0.75	…	Y	
NGC 7679	13.97	12.94	12.50	12.31	12.16	10.17	5.54	0.03	0.03		
NGC 7682	14.95	13.29	12.57	12.16	11.91	10.53	1.21	0.27	0.01		
NGC 788	14.28	12.51	11.75	11.3	11	10.68	1.70	0.44	0.02		
NGC 931	14.63	13.08	12.51	11.82	11.55	10.6	27.0	0.82	…	Y	
NGC 973	14.81	12.95	12.06	11.44	10.74	10.84	0.65	1.03	0.12		
NGC 985	15.74	14.07	13.62	13.19	13.22	10.71	29.9	0.17	…	Y	
SBS 1301+540	17.50	15.87	15.30	14.88	14.81	9.79	14.5	0.17	0.05		
UGC 02724	16.77	15.47	15.02	14.63	14.63	10.04	3.53	0.07	0.03		

Continued on Next Page…

Table A.4 – Continued

Galaxy	u^1	g	r	i	z	$\log \mathbf{M_*}^2$	$\mathbf{PS}_r{}^3$	$\mathbf{E}(g-r)^4$	$\mathbf{E}(g-r)^5$	u^6	$griz^7$
	mag	mag	mag	mag	mag	M$_\odot$	%	mag	Inc. mag	Con.	Con.
UGC 03142	14.58	12.52	12.29	12.03	12.09	10.21	7.65	0.17	0.02		
UGC 03601	16.01	14.37	13.67	13.32	13.10	10.04	6.85	0.14	⋯		
UGC 03995A	13.2	12.69	12.06	11.70	11.40	10.57	2.67	0.96	0.05		
UGC 05881	15.66	14.35	13.62	13.26	13.05	10.22	2.75	0.07	0.06		
UGC 06527 NED03	16.21	14.68	14.03	13.69	13.48	10.22	1.90	0.14	⋯		
UGC 07064	14.89	13.7	13.11	12.72	12.50	10.54	5.10	0.34	0.01		
UGC 08327 NED02	16.79	14.88	14.09	13.73	13.47	10.55	5.59	0.34	⋯		
UGC 11185 NED02	16.34	15.24	14.6	14.12	13.85	10.41	2.2	0.72	⋯		
UGC 12282	14.67	13.02	12.11	11.52	11.33	10.78	1.06	0.44	⋯		
UGC 12741	15.48	14.14	13.49	13.13	12.96	10.08	1.16	0.07	0.08		
UM 614	15.65	15.83	15.15	14.82	14.67	9.99	28.3	0.07	⋯	Y	
VII Zw 073	16.19	15.1	14.58	14.23	14.08	10.33	2.35	0.17	0.01		
1RXS J045205.0+493248	14.55	14.06	13.69	13.44	13.50	10.1	39.8	⋯	⋯	Y	Y
2MASX J03305218+0538253	15.65	15.46	15.44	15.04	15.15	10.02	58.6	⋯	⋯	Y	Y
2MASX J11454045-1827149	15.43	15.00	15.28	14.31	14.18	10.04	76.5	⋯	⋯	Y	Y
3C 111.0	⋯	15.57	14.26	13.96	14.36	10.03	80.1	⋯	⋯	Y	Y
3C 120	15.23	14.10	13.55	13.19	13.21	10.41	48.3	⋯	⋯	Y	Y
Ark 120	13.99	13.59	13.21	13.04	12.84	10.72	52.4	⋯	⋯	Y	Y
HB89 0241+622	16.79	15.94	15.11	14.46	14.33	10.4	69.1	⋯	⋯	Y	Y
IGR J21277+5656	⋯	13.27	13.21	13.08	13.27	9.18	40.9	⋯	⋯	Y	Y
IRAS 04124-0803	17.79	16.03	15.95	15.45	14.96	9.8	80.1	⋯	⋯	Y	Y

Continued on Next Page…

Table A.4 – Continued

Galaxy	u^1	g	r	i	z	$\log \mathbf{M}_*^2$	$\mathbf{PS}_r^3$	$\mathbf{E}(g-r)^4$	$\mathbf{E}(g-r)^5$	u^6	$griz^7$
	mag	mag	mag	mag	mag	$\mathrm{M}_\odot$	%	mag	Inc. mag	Con.	Con.
IRAS 05218-1212	16.44	15.45	14.71	14.22	14.20	10.46	50.5	$\ldots$	$\ldots$	Y	Y
IRAS 05589+2828	$\ldots$	15.36	14.87	13.81	13.42	10.41	81.6	$\ldots$	$\ldots$	Y	Y
KAZ 320	15.94	15.20	15.00	15.07	14.61	9.7	34.9	$\ldots$	$\ldots$	Y	Y
LEDA 138501	$\ldots$	18.17	19.56	18.16	18.35	8.59	99.0	$\ldots$	$\ldots$	Y	Y
MRK 1044	15.49	14.54	13.88	13.52	13.40	9.88	36.9	$\ldots$	$\ldots$	Y	Y
Mrk 290	18.37	15.74	15.19	14.86	14.71	9.8	52.9	$\ldots$	$\ldots$	Y	Y
Mrk 335	16.26	15.34	14.94	14.89	14.66	9.47	71.1	$\ldots$	$\ldots$	Y	Y
Mrk 509	14.91	14.21	13.77	13.60	13.26	10.39	56.4	$\ldots$	$\ldots$	Y	Y
Mrk 704	17.48	15.04	14.30	13.78	13.55	10.34	40.5	$\ldots$	$\ldots$	Y	Y
Mrk 841	16.55	16.06	15.45	15.00	15.02	9.97	82.4	$\ldots$	$\ldots$	Y	Y
RX J2044.0+2833	15.28	15.19	14.64	14.48	14.50	10.37	48.3	$\ldots$	$\ldots$	Y	Y

Continued on Next Page...

147

Table A.4 – Continued

Galaxy	u[1]	g	r	i	z	$\log \mathbf{M_*}$[2]	$\mathbf{PS}_r$[3]	$\mathbf{E}(g-r)$[4]	$\mathbf{E}(g-r)$[5]	u[6]	$griz$[7]
	mag	mag	mag	mag	mag	$M_\odot$	%	mag	Inc. mag	Con.	Con.
SDSS J104326.47+110524.2	19.16	17.31	17.33	16.80	17.30	8.65	70.4	$\cdots$	$\cdots$	Y	Y

[1]Measured host galaxy Petrosian mag after subtraction of AGN contamination using GALFIT. In some cases the galaxy was not detected in the u band.

[2]We used the software KCORRECT (Blanton & Roweis 2007) with the $ugriz$ photometry to calculate the stellar masses. This code uses the stellar population models of Bruzual & Charlot (2003) and photoionization models of Kewley et al. (2001).

[3]The value of the percentage of AGN to total (AGN and galaxy) light in the r band.

[4]Estimated reddening correction for dust based on AGN host $ugriz$ SED fitting using FAST (Kriek et al. 2009) with single-burst stellar population models.

[5]Estimated reddening correction for spiral galaxies based on inclination following Masters et al. (2010).

[6]We excluded the u photometry from this study because of the possibility of AGN contamination even after subtraction with GALFIT since %$PS_r > 20$.

[7]We excluded the $griz$ photometry and determination of M_* from this study because of the possibility of AGN contamination even after subtraction with GALFIT.

Table A.5.   Color Comparison

log M_*	Type	N	Mean $(g-r)$	P(K-S)%[1]	Mean $(u-r)$	P(K-S)%
9.6 to 10	BAT	37	0.62±0.15		2.42±0.91	
	Inactive	23041	0.63±0.15	41	2.03±0.43	10
	SDSS AGN	455	0.72±0.10	<0.01	2.31±0.29	36
10 to 10.3	BAT	39	0.68±0.12		2.18±0.36	
	Inactive	7542	0.76±0.12	<0.01	2.40±0.38	<0.01
	SDSS AGN	743	0.76±0.09	<0.01	2.40±0.39	<0.01
10.3 to 10.6	BAT	39	0.69±0.13		2.26±0.57	
	Inactive	3108	0.81±0.12	<0.01	2.56±0.22	<0.01
	SDSS AGN	397	0.78±0.09	<0.01	2.48±0.28	<0.01
>10.6	BAT	39	0.70±0.14		2.23±0.67	
	Inactive	820	0.81±0.04	<0.01	2.78±0.20	<0.01
	SDSS AGN	148	0.83±0.07	<0.01	2.65±0.27	<0.01

[1]Probability percentage from a Kolmogorov-Smirnov (K-S) test that the BAT colors are from the same parent population.

Table A.6: Morphological Properties

Galaxy	R_P [1]	C [2]	Class [3]	b/a [4]	Broad [5]
	$''$	R_{90}/R_{50}			
2MASX J00253292+6821442	$\cdots$ [6]	$\cdots$	M	0.43	
2MASX J01064523+0638015	12.8	3.10	S	0.80	
2MASX J03534246+3714077	8.66	3.03	I	0.56	
2MASX J04440903+2813003	30.8	2.92	I	0.91	
2MASX J05054575-2351139	7.14	3.37	I	0.87	
2MASX J06411806+3249313	9.11	2.93	M	0.82	
2MASX J07595347+2323241	15.7	2.80	S	0.49	
2MASX J09112999+4528060	9.22	2.90	I	0.70	
2MASX J12005792+0648226	17.9	3.30	I	0.55	
2MASX J16174158+0607100	9.53	2.83	S	0.25	
2MFGC 02280	15.4	2.99	S	0.21	
ARK 347	11.2	3.26	I	0.60	
ARP 102B	12.1	3.55	E	0.79	
CGCG 102-048	10.5	3.04	S	0.36	

Continued on Next Page. . .

Galaxy	R_P [1]	C [2]	Class [3]	b/a [4]	Broad [5]
	″	R_{90}/R_{50}			
CGCG 300-062	14.0	2.73	S	0.77	
CGCG 312-012	8.52	3.04	E	0.95	
CGCG 420-015	13.7	3.27	E	0.77	
CGCG 427-028	14.6	2.58	I	0.22	
ESO 506-G027	44.9	3.74	S	0.31	
FAIRALL 272	18.6	3.21	M	0.61	
IC 0486	17.5	3.04	S	0.65	
IC 0751	16.9	2.85	S	0.28	
IC 2461	29.2	3.00	S	0.22	
IC 2515	16.6	3.42	S	0.22	
LEDA 170194	16.7	2.66	S	0.90	
LEDA 214543	10.6	3.13	I	0.87	
M106	216.	3.01	S	0.38	
MCG -01-05-047	66.1	2.87	S	0.13	
MCG -01-24-012	27.9	2.75	S	0.56	
MCG -01-40-001	39.6	2.65	S	0.34	
MCG -02-08-014	11.9	3.09	S	0.16	
MCG -02-12-050	24.1	2.88	M/S	0.89	
MCG -05-14-012	15.6	3.39	M/I	0.86	
MCG -05-23-016	15.4	3.26	I	0.45	
MCG +02-21-013	22.0	2.65	I	0.43	
MCG +04-48-002	20.8	2.73	M/S	0.36	
MCG +05-28-032	12.9	2.88	S	0.51	
MCG +06-24-008	17	2.44	S	0.26	
MCG +06-49-019	18.4	3.18	S	0.64	
MCG +11-11-032	11.8	3.02	S	0.45	
MCG+10-17-061	8.52	2.67	I	0.92	
Mrk 1210	15.6	2.93	E	0.86	
Mrk 18	8.5	3.15	I	0.15	
Mrk 198	7.71	3.31	S	0.86	
Mrk 268	12.8	3.31	I	0.45	
Mrk 348	55.0	3.19	S	0.97	
Mrk 417	9.1	3.18	E	0.77	
Mrk 463E	12.6	2.24	M	0.41	
Mrk 477	6.19	2.56	M	0.71	

Continued on Next Page. . .

Table A.6 – Continued

Galaxy	R_P [1]	C [2]	Class [3]	b/a [4]	Broad [5]
	″	R_{90}/R_{50}			
Mrk 732	16.5	3.17	I	0.87	
Mrk 78	$\cdots$	$\cdots$	I	0.61	
NGC 0835	24.3	2.99	M/S	0.45	
NGC 1012	47.8	2.57	S	0.51	
NGC 1052	44.0	3.06	E	0.56	
NGC 1142	28.0	2.87	M	0.48	
NGC 1194	35.8	3.22	I	0.47	
NGC 1275	52.1	3.02	M	0.74	
NGC 2110	53.9	3.35	E	0.74	
NGC 235A	11.5	3.09	M	0.52	
NGC 2992	41.4	3.09	M	0.30	
NGC 3079	119.	3.12	S	0.15	
NGC 3081	41.8	2.69	S	0.77	
NGC 3281	70.4	2.21	S	0.50	
NGC 3718	106.	2.65	S	0.42	
NGC 4102	51.8	2.60	S	0.41	
NGC 4388	81.7	3.13	S	0.18	
NGC 452	23.6	2.94	S	0.28	
NGC 4686	21.4	3.47	I	0.29	
NGC 4992	19.8	2.62	I	0.57	
NGC 5106	14.2	2.87	M/S	0.69	
NGC 513	13.9	2.27	M/S	0.51	
NGC 5231	26.0	2.44	S	0.51	
NGC 5252	25.1	3.20	I	0.56	
NGC 5290	53.4	2.86	S	0.27	
NGC 5506	56.2	2.30	I	0.23	
NGC 5610	26.5	2.32	S	0.33	
NGC 5728	82.3	2.58	S	0.57	
NGC 5899	57.0	2.60	S	0.43	
NGC 5995	21.1	3.43	I	0.32	
NGC 6240	36.5	2.95	M	0.51	
NGC 7319	$\cdots$	$\cdots$	M/S	0.55	
NGC 7682	37.1	2.78	S	0.89	
NGC 788	31.7	3.01	S	0.75	
NGC 973	$\cdots$	$\cdots$	S	0.14	

Continued on Next Page. . .

Table A.6 – Continued

Galaxy	R_P [1]	C [2]	Class [3]	b/a [4]	Broad [5]
	″	R_{90}/R_{50}			
UGC 02724	40.8	1.87	S	0.65	
UGC 03995A	45.2	2.37	S	0.44	
UGC 05881	10.6	3.19	S	0.38	
UGC 06527 NED03	7	3.65	M/S	0.32	
UGC 07064	20.7	2.56	S	0.88	
UGC 08327 NED02	18.0	3.94	M/S	0.62	
UGC 11185 NED02	$\cdots$	$\cdots$	M/S	0.96	
UGC 12741	13.6	3.18	S	0.28	
2MASX J09043699+5536025	4.74	3.56	M	0.61	Y
2MASX J21355399+4728217	$\cdots$	$\cdots$	S	0.18	Y
ARP 151	4.94	3.15	M	0.16	Y
CGCG 031-072	10.5	3.04	I	0.59	Y
CGCG 046-033	11.3	2.50	S	0.75	Y
CGCG 122-055	12.9	2.97	I	0.75	Y
CGCG 198-020	20.6	2.45	I	0.71	Y
CGCG 319-007	12.2	2.68	I	0.61	Y
ESO 490-IG026	28.9	3.59	M	0.68	Y
ESO 511-G030	75.0	3.34	S	0.70	Y
IC 4329A	$\cdots$	$\cdots$	S	0.27	Y
KAZ 320	2.68	2.76	I	0.79	Y
KUG 1141+371	12.2	2.67	I	0.87	Y
KUG 1208+386	11.9	3.26	E	0.94	Y
MCG -01-13-025	16.8	3.19	E	0.61	Y
MCG -03-34-064	11.2	3.37	E	0.81	Y
MCG +01-57-016	7.12	3.78	S	0.86	Y
MCG +04-06-043	13.9	2.91	S	0.92	Y
MCG +04-22-042	15.2	2.92	S	0.56	Y
MCG +08-11-011	1.36	2.47	S	0.70	Y
Mrk 10	31.8	2.64	S	0.41	Y
Mrk 1018	11.1	3.72	M	0.52	Y
Mrk 110	4.64	3.68	M	0.62	Y
Mrk 1392	18.4	3.04	S	0.51	Y
Mrk 1469	8.82	3.26	I	0.35	Y
Mrk 279	19.0	2.73	M/S	0.58	Y
Mrk 352	$\cdots$	$\cdots$	I	0.83	Y

Continued on Next Page. . .

Galaxy	R_P [1]	C [2]	Class [3]	b/a [4]	Broad [5]
	"	R_{90}/R_{50}			
Mrk 464	2.6	3.23	I	0.76	Y
Mrk 50	8.03	2.94	E	0.60	Y
Mrk 520	15.0	3.63	S	0.62	Y
Mrk 590	29.3	2.92	M/S	0.97	Y
Mrk 595	7.2	3.24	M/E	0.62	Y
Mrk 705	5.14	3.50	I	0.88	Y
Mrk 728	7.08	3.08	E	0.64	Y
Mrk 739E	14.2	2.18	M/S	0.87	Y
Mrk 766	20.4	2.78	S	0.78	Y
Mrk 79	39.4	2.49	S	0.90	Y
Mrk 817	9.04	3.42	S	0.87	Y
Mrk 915	14.7	2.97	S	0.35	Y
Mrk 926	18.8	2.87	S	0.82	Y
NGC 2885	13.1	3	S	0.69	Y
NGC 3227	81	2.52	M/S	0.56	Y
NGC 3516	$\cdots$	$\cdots$	E	0.77	Y
NGC 3786	38.4	2.68	M/S	0.59	Y
NGC 4051	$\cdots$	$\cdots$	S	0.68	Y
NGC 4138	41.3	2.59	S	0.65	Y
NGC 4235	48.2	3.29	S	0.22	Y
NGC 4395	$\cdots$	$\cdots$	S	0.83	Y
NGC 4593	92.1	2.38	S	0.74	Y
NGC 5273	58.2	2.26	I	0.92	Y
NGC 5548	36.0	3.25	S	0.87	Y
NGC 5674	31.1	1.70	S	0.92	Y
NGC 5683	8.35	3.23	I	0.52	Y
NGC 5940	22.0	2.11	S	0.98	Y
NGC 6814	76.2	2.31	S	0.93	Y
NGC 7314	92.1	2.38	S	0.45	Y
NGC 7469	17.0	3.29	M/S	0.72	Y
NGC 7603	2.21	2.78	M/S	0.65	Y
NGC 7679	17.0	3.29	S	0.64	Y
NGC 931	48.6	3.45	M/S	0.21	Y
NGC 985	22.1	3.20	M	0.71	Y
SBS 1301+540	5.93	3.11	S	0.42	Y

Continued on Next Page. . .

Galaxy	R_P [1]	C [2]	Class [3]	b/a [4]	Broad [5]
	"	R_{90}/R_{50}			
UGC 03142	28.8	2.00	S	0.78	Y
UGC 03601	13.4	3.02	I	0.74	Y
UGC 12282	34.3	3.08	I	0.27	Y
UM 614	4.9	3.44	I	0.51	Y
VII Zw 073	7.36	2.58	S	0.91	Y

[1]The Petrosian radius was determined as the point when the Petrosian Ratio= $\int_{0.8r}^{1.25r} dr' \ 2\pi r' I(r')/\pi(1.25^2 - 0.8^2)r^2)/(\int_0^{r'} dr' \ 2\pi r I(r')/\pi r^2 = 0.2$.

[2]The concentration index is defined as the ratio of the radii containing 90 and 50 per cent of the Petrosian r-band galaxy light $C = R_{90}/R_{50}$.

[3]Galaxy Zoo Class where E stands for ellipticals, I, for intermediates, S, for spirals, and M for mergers/peculiars. For the Kitt Peak data, which has no Galaxy Zoo data, we use the Hubble Types from the RC3 with T = -6 to -4 corresponding to ellipticals, T = -3 to 0 to intermediates, T > 0 to spirals.

[4]We use the observed axial ratio (a/b) as a proxy for inclination. An a/b=1 corresponds to a face-on galaxy. We use the g band and fit to the 25th mag arcsecond^{-2} isophote.

[5]Whether the galaxy has a broad-line AGN based on SDSS galaxy class or the available optical spectra. While we excluded these broad-line measurements from the morphological analysis, we have provided them for completeness. We subtracted the AGN model for these galaxies before determining the Petrosian radius and concentration index. However, the difficulty of perfectly subtracting the AGN light distribution makes these values more uncertain.

[6]The Petrosian radius and concentration failed to converge. This happened more often for close mergers or in a broad-line AGN where the AGN was imperfectly subtracted.

Appendix B

Glossary

B.1 Abbreviations

2MASS: Two-micron all sky survey

A_V**:** total extinction in the optical V band

ASCA: the Advanced Satellite for Cosmology and Astrophysics, a Japanese X-ray satellite launched in 1993

AGN: active galactic nuclei

BAT: Burst Alert Telescope onboard SWIFT, sensitive in the 14–195 keV band

CO: Carbon monoxide; molecular hydrogen is difficult to detect by infrared and radio observations, so the molecule most often used to determine the presence of H_2 is CO.

CCD: charge coupled device

CXB: cosmic X-ray background

Dec: declination

dof: degrees of freedom

E: energy; measured in keV for the X-ray band

$E(B-V)$**:** selective extinction between the optical B and V bands ($A_B - A_V$)

EPIC: European photon-imaging camera; instrument onboard *XMM-Newton*

F: flux; measured in $\mathrm{ergs\,s^{-1}\,cm^{-2}}$

FIR: Far-infrared; roughly 40 μm to 250 μm

FITS: Flexible Image Transport System; standard astronomical data format endorsed by NASA and the IAU

FWHM: full-width half maximum

H I:

GALFIT: data analysis algorithm that fits 2-D analytic functions to galaxies and point sources directly to digital images

GRB: gamma ray burst

HEAO-1: High Energy Astronomical Observatory

HEASARC: NASA's High Energy Astrophysics Science Archive Research Center

HST: Hubble Space Telescope

InFOCμS: International Balloon Focusing Optics Collaboration for μCrab Sensitivity

IR: infrared

ISM: interstellar medium; the gas and dust between stars

kT: measurement of the accretion disk temperature in units of energy; the Boltzmann constant times the accretion disk temperature

L: luminosity; measured in $\mathrm{ergs\,s^{-1}}$

L$_{Edd}$: Eddington luminosity

M: mass

$\dot{M}$**:** mass accretion rate

NASA: National Aeronautics and Space Administration

NED: NASA/IPAC Extragalactic Database

NIR: Near-infrared; roughly 1 μm to 5 μm.

n$_H$: column density of neutral hydrogen; measured in $\mathrm{atoms\,cm^{-2}}$

OM: Optical monitor; optical/UV telescope onboard *XMM-Newton*

PSF: point spread function

QSO: Quasi-stellar object; designation for a type of AGN

RA: right ascension

RC3: third reference catalogue of bright galaxies

SDSS: Sloan digital sky survey; a major multi-filter imaging and spectro-scopic redshift survey

SExtractor: Source-Extractor; program that builds a catalogue of objects from an astronomical image

SFR: star formation rate

SMBH: supermassive black hole

Sy: Seyfert type; an optical classification scheme for AGN

  Sy1: shows optical broad emission lines and narrow emission lines

  Sy1.5: intermediary between a Sy1 and Sy2 source

  Sy2: shows only narrow optical emission lines

ULX: ultra-luminous X-ray source

UV: Ultraviolet light. Roughly 100 to 4000 Å.

UVOT: Ultraviolet/optical telescope; onboard SWIFT

VLA: Very Large Array; an array of radio telescopes located near Socorro, NM

XMM: X-ray Multi-mirror Mission

XRT: X-ray telescope; onboard SWIFT

XSPEC: A data analysis and spectral fitting program used in X-ray astronomy

z: redshift

B.2   Symbols

χ^2**:** a statistic used to compute goodness of fit for a model
η**:** efficiency factor for mass to energy conversion
Γ**:** photon spectral index measured from a power law model
μ**:** mean/average value
ν**:** degrees of freedom
σ**:** signal to noise; alternatively, the measured error/standard deviation or
   a cross section
τ**:** optical depth

B.3   Units

Å: Angstrom; a unit of length
      : $1\text{Å} = 10^{-10}\,\text{m}$
Crab: a unit of intensity corresponding to the flux density of a bright
  X-ray source, the Crab nebula
      : $1\,\text{Crab} = 1060\mu\text{J}$
      : $1\,\text{Crab} = 2.5652 \times 10^{-9}\text{erg s}^{-1}\text{ cm}^2\,\text{keV}^{-1}$
erg: a unit of energy
      : $1\,\text{erg} = 10^{-7}\,\text{J}$
eV: electron volt, a unit of energy
      : $1\text{ eV} = 1.60217653(14) \times 10^{-19}\,\text{J}$
Jy: Jansky; a unit of flux density
      : $1\,\text{Jy} = 10^{-23}\text{erg s}^{-1}\text{ cm}^2\,\text{Hz}^{-1}$
      : $1\,\text{Jy} = 2.42 \times 10^{-18}\text{erg s}^{-1}\text{ cm}^2\,\text{keV}^{-1}$
M$_\odot$: solar mass
      : $1M_\odot = 1.9891 \times 10^{30}\,\text{kg}$
Mpc: Mega parsec; a unit of distance
      : $1\,\text{Mpc} = 3.08568025 \times 10^{24}\,\text{cm}$ or $1.91735281 \times 10^{19}\,\text{miles}$
sr: steradian; SI unit of solid angle

B.4   Constants

c: speed of light in a vacuum; $2.99792458 \times 10^8\,\text{m s}^{-1}$
G: Gravitational constant; $G = 6.67300 \times 10^{-11}\,\text{m}^3\,\text{kg}^{-1}\,\text{s}^{-2}$
H$_0$: Hubble's constant; we adopt $\text{H}_0 = 70\,\text{km s}^{-1}\,\text{Mpc}^{-1}$
h: Planck's constant; $h = 6.626068 \times 10^{-34}\,\text{m}^2\,\text{kg s}^{-1}$
k: Boltzmann's constant; $8.617343(15) \times 10^{-5}\,\text{eV K}^{-1}$
σ_T**:** Thomson cross section; $6.652 \times 10^{25}\,\text{cm}^{-2}$

Bibliography

Abazajian, K., Adelman-McCarthy, J. K., Agüeros, M. A., Allam, S. S., Anderson, S. F., Annis, J., Bahcall, N. A., Baldry, I. K., Bastian, S., Berlind, A., Bernardi, M., Blanton, M. R., Blythe, N., Bochanski, J. J., Boroski, W. N., Brewington, H., Briggs, J. W., Brinkmann, J., Brunner, R. J., Budavári, T., Carey, L. N., Carr, M. A., Castander, F. J., Chiu, K., Collinge, M. J., Connolly, A. J., Covey, K. R., Csabai, I., Dalcanton, J. J., Dodelson, S., Doi, M., Dong, F., Eisenstein, D. J., Evans, M. L., Fan, X., Feldman, P. D., Finkbeiner, D. P., Friedman, S. D., Frieman, J. A., Fukugita, M., Gal, R. R., Gillespie, B., Glazebrook, K., Gonzalez, C. F., Gray, J., Grebel, E. K., Grodnicki, L., Gunn, J. E., Gurbani, V. K., Hall, P. B., Hao, L., Harbeck, D., Harris, F. H., Harris, H. C., Harvanek, M., Hawley, S. L., Heckman, T. M., Helmboldt, J. F., Hendry, J. S., Hennessy, G. S., Hindsley, R. B., Hogg, D. W., Holmgren, D. J., Holtzman, J. A., Homer, L., Hui, L., ichi Ichikawa, S., Ichikawa, T., Inkmann, J. P., Ivezić, Ž., Jester, S., Johnston, D. E., Jordan, B., Jordan, W. P., Jorgensen, A. M., Jurić, M., Kauffmann, G., Kent, S. M., Kleinman, S. J., Knapp, G. R., Kniazev, A. Y., Kron, R. G., Krzesiński, J., Kunszt, P. Z., Kuropatkin, N., Lamb, D. Q., Lampeitl, H., Laubscher, B. E., Lee, B. C., Leger, R. F., Li, N., Lidz, A., Lin, H., Loh, Y.-S., Long, D. C., Loveday, J., Lupton, R. H., Malik, T., Margon, B., McGehee, P. M., McKay, T. A., Meiksin, A., Miknaitis, G. A., Moorthy, B. K., Munn, J. A., Murphy, T., Nakajima, R.,

Narayanan, V. K., Nash, T., Neilsen, E. H., Newberg, H. J., Newman, P. R., Nichol, R. C., Nicinski, T., Nieto-Santisteban, M., Nitta, A., Odenkirchen, M., Okamura, S., Ostriker, J. P., Owen, R., Padmanabhan, N., Peoples, J., Pier, J. R., Pindor, B., Pope, A. C., Quinn, T. R., Rafikov, R. R., Raymond, S. N., Richards, G. T., Richmond, M. W., Rix, H.-W., Rockosi, C. M., Schaye, J., Schlegel, D. J., Schneider, D. P., Schroeder, J., Scranton, R., Sekiguchi, M., Seljak, U., Sergey, G., Sesar, B., Sheldon, E., Shimasaku, K., Siegmund, W. A., Silvestri, N. M., Sinisgalli, A. J., Sirko, E., Smith, J. A., Smolčić, V., Snedden, S. A., Stebbins, A., Steinhardt, C., Stinson, G., Stoughton, C., Strateva, I. V., Strauss, M. A., SubbaRao, M., Szalay, A. S., Szapudi, I., Szkody, P., Tasca, L., Tegmark, M., Thakar, A. R., Tremonti, C., Tucker, D. L., Uomoto, A., Berk, D. E. V., Vandenberg, J., Vogeley, M. S., Voges, W., Vogt, N. P., Walkowicz, L. M., Weinberg, D. H., West, A. A., White, S. D. M., Wilhite, B. C., Willman, B., Xu, Y., Yanny, B., Yarger, J., Yasuda, N., Yip, C.-W., Yocum, D. R., York, D. G., Zakamska, N. L., Zehavi, I., Zheng, W., Zibetti, S., & Zucker, D. B. 2003, AJ, 126, 2081

Abraham, R. G. 1997, The ultraviolet universe at low and high redshift. AIP Conference Proceedings, 408, 195

Ajello, M., Rau, A., Greiner, J., Kanbach, G., Salvato, M., Strong, A. W., Barthelmy, S. D., Gehrels, N., Markwardt, C. B., & Tueller, J. 2008, ApJ, 673, 96

Antonucci, R. 1993, ARA&A, 31, 473

Antonucci, R. R. J. & Miller, J. S. 1985, ApJ, 297, 621

Baade, W. & Minkowski, R. 1954, ApJ, 119, 215

Baldwin, J. A., Phillips, M. M., & Terlevich, R. 1981, Astronomical Society of the Pacific, 93, 5

Barden, M., Jahnke, K., & Haubler, B. 2008, ApJSS, 175, 105

Bassani, L., Dadina, M., Maiolino, R., Salvati, M., Risaliti, G., della Ceca, R., Matt, G., & Zamorani, G. 1999, ApJSS, 121, 473

Beckmann, V., Soldi, S., Ricci, C., Alfonso-Garzón, J., Courvoisier, T. J.-L., Domingo, A., Gehrels, N., Lubiński, P., Mas-Hesse, J. M., & Zdziarski, A. A. 2009, A&A, 505, 417

Bell, E. F., Phleps, S., Somerville, R. S., Wolf, C., Borch, A., & Meisenheimer, K. 2006, ApJ, 652, 270

Bentz, M. C., Peterson, B., Pogge, R., Vestergaard, M., & Onken, C. 2006, ApJ, 644, 133

Bernardi, M., Sheth, R. K., Annis, J., Burles, S., Eisenstein, D. J., Finkbeiner, D. P., Hogg, D. W., Lupton, R. H., Schlegel, D. J., SubbaRao, M., Bahcall, N. A., Blakeslee, J. P., Brinkmann, J., Castander, F. J., Connolly, A. J., Csabai, I., Doi, M., Fukugita, M., Frieman, J., Heckman, T., Hennessy, G. S., Ivezić, Ž., Knapp, G. R., Lamb, D. Q., McKay, T., Munn, J. A., Nichol, R., Okamura, S., Schneider, D. P., Thakar, A. R., & York, D. G. 2003, AJ, 125, 1849

Bertin, E. & Arnouts, S. 1996, A&AS, 117, 393

Bertram, T., Eckart, A., Fischer, S., Zuther, J., Straubmeier, C., Wisotzki, L., & Krips, M. 2007, A&A, 470, 571

Blandford, R. D. & Rees, M. J. 1978, In: Pittsburgh Conference on BL Lac Objects, 328

Blanton, M. R., Dalcanton, J., Eisenstein, D., Loveday, J., Strauss, M. A., SubbaRao, M., Weinberg, D. H., Anderson, J. E., Annis, J., Bahcall, N. A., Bernardi, M., Brinkmann, J., Brunner, R. J., Burles, S., Carey, L., Castander, F. J., Connolly, A. J., Csabai, I., Doi, M., Finkbeiner, D., Friedman, S., Frieman, J. A., Fukugita, M., Gunn, J. E., Hennessy, G. S., Hindsley, R. B., Hogg, D. W.,

Ichikawa, T., Ivezić, Ž., Kent, S., Knapp, G. R., Lamb, D. Q., Leger, R. F., Long, D. C., Lupton, R. H., McKay, T. A., Meiksin, A., Merelli, A., Munn, J. A., Narayanan, V., Newcomb, M., Nichol, R. C., Okamura, S., Owen, R., Pier, J. R., Pope, A., Postman, M., Quinn, T., Rockosi, C. M., Schlegel, D. J., Schneider, D. P., Shimasaku, K., Siegmund, W. A., Smee, S., Snir, Y., Stoughton, C., Stubbs, C., Szalay, A. S., Szokoly, G. P., Thakar, A. R., Tremonti, C., Tucker, D. L., Uomoto, A., Berk, D. V., Vogeley, M. S., Waddell, P., Yanny, B., Yasuda, N., & York, D. G. 2001, AJ, 121, 2358

Blanton, M. R. & Roweis, S. 2007, AJ, 133, 734

Bruzual, G. & Charlot, S. 2003, MNRAS, 344, 1000

Calzetti, D., Armus, L., Bohlin, R., Kinney, A., Koornneef, J., & Storchi-Bergmann, T. 2000, ApJ, 533, 682

Cardelli, J. A., Clayton, G. C., & Mathis, J. S. 1989, ApJ, 345, 245

Chabrier, G. 2003, PASJ, 115, 763

Colless, M., Dalton, G., Maddox, S., Sutherland, W., Norberg, P., Cole, S., Bland-Hawthorn, J., Bridges, T., Cannon, R., Collins, C., Couch, W., Cross, N., Deeley, K., de Propris, R., Driver, S. P., Efstathiou, G., Ellis, R. S., Frenk, C. S., Glazebrook, K., Jackson, C., Lahav, O., Lewis, I., Lumsden, S., Madgwick, D., Peacock, J. A., Peterson, B. A., Price, I., Seaborne, M., & Taylor, K. 2001, MNRAS, 328, 1039

Dekel, A., Birnboim, Y., Engel, G., Freundlich, J., Goerdt, T., Mumcuoglu, M., Neistein, E., Pichon, C., Teyssier, R., & Zinger, E. 2009, Nature, 457, 451

di Matteo, T., Springel, V., & Hernquist, L. 2005, Nature, 433, 604

Domingue, D., Sulentic, J., & Durbala, A. 2005, AJ, 129, 2579

Dopita, M. A. & Sutherland, R. S. 1995, Astrophysical Journal v.455, 455, 468

Elvis, M., Wilkes, B. J., McDowell, J. C., Green, R. F., Bechtold, J., Willner, S. P.,

Oey, M. S., Polomski, E., & Cutri, R. 1994, ApJSS, 95, 1

Fanidakis, N., Baugh, C. M., Benson, A. J., Bower, R. G., Cole, S., Done, C., & Frenk, C. S. 2011, MNRAS, 410, 53

Farrell, S. A., Webb, N. A., Barret, D., Godet, O., & Rodrigues, J. M. 2009, Nature, 460, 73

Filippenko, A. V., Ho, L. C., & Sargent, W. L. W. 1993, ApJ, 410, L75

Fischer, T. C., Crenshaw, D. M., Kraemer, S. B., Schmitt, H. R., Mushotsky, R. F., & Dunn, J. P. 2011, ApJ, 727, 71

Gabor, J. M., Impey, C. D., Jahnke, K., Simmons, B. D., Trump, J. R., Koekemoer, A. M., Brusa, M., Cappelluti, N., Schinnerer, E., Smolčić, V., Salvato, M., Rhodes, J. D., Mobasher, B., Capak, P., Massey, R., Leauthaud, A., & Scoville, N. 2009, ApJ, 691, 705

Garcet, O., Gandhi, P., Gosset, E., Sprimont, P. G., Surdej, J., Borkowski, V., Tajer, M., Pacaud, F., Pierre, M., Chiappetti, L., Maccagni, D., Page, M. J., Carrera, F. J., Tedds, J. A., Mateos, S., Krumpe, M., Contini, T., Corral, A., Ebrero, J., Gavignaud, I., Schwope, A., Fèvre, O. L., Polletta, M., Rosen, S., Lonsdale, C., Watson, M., Borczyk, W., & Vaisanen, P. 2007, A&A, 474, 473

Gavazzi, G., Franzetti, P., Scodeggio, M., Boselli, A., & Pierini, D. 2000, A&A, 361, 863

Gehrels, N., Chincarini, G., Giommi, P., Mason, K. O., Nousek, J. A., Wells, A. A., White, N. E., Barthelmy, S. D., Burrows, D. N., Cominsky, L. R., Hurley, K. C., Marshall, F. E., Mészáros, P., Roming, P. W. A., Angelini, L., Barbier, L. M., Belloni, T., Campana, S., Caraveo, P. A., Chester, M. M., Citterio, O., Cline, T. L., Cropper, M. S., Cummings, J. R., Dean, A. J., Feigelson, E. D., Fenimore, E. E., Frail, D. A., Fruchter, A. S., Garmire, G. P., Gendreau, K., Ghisellini, G., Greiner, J., Hill, J. E., Hunsberger, S. D., Krimm, H. A., Kulkarni, S. R.,

Kumar, P., Lebrun, F., Lloyd-Ronning, N. M., Markwardt, C. B., Mattson, B. J., Mushotzky, R. F., Norris, J. P., Osborne, J., Paczynski, B., Palmer, D. M., Park, H.-S., Parsons, A. M., Paul, J., Rees, M. J., Reynolds, C. S., Rhoads, J. E., Sasseen, T. P., Schaefer, B. E., Short, A. T., Smale, A. P., Smith, I. A., Stella, L., Tagliaferri, G., Takahashi, T., Tashiro, M., Townsley, L. K., Tueller, J., Turner, M. J. L., Vietri, M., Voges, W., Ward, M. J., Willingale, R., Zerbi, F. M., & Zhang, W. W. 2004, ApJ, 611, 1005

Geller, M. J., Kenyon, S. J., Barton, E. J., Jarrett, T. H., & Kewley, L. J. 2006, AJ, 132, 2243

Georgakakis, A., Nandra, K., Yan, R., Willner, S. P., Lotz, J. M., Pierce, C. M., Cooper, M. C., Laird, E. S., Koo, D. C., Barmby, P., Newman, J. A., Primack, J. R., & Coil, A. L. 2008, MNRAS, 385, 2049

Giacconi, R., Gursky, H., Paolini, F. R., & Rossi, B. B. 1962, Physical Review Letters, 9, 439

Gladstone, J. C. 2010, AIPC, 1314, 353

Goulding, A. D. & Alexander, D. M. 2009, MNRAS, 398, 1165

Greve, T. R., Papadopoulos, P. P., Gao, Y., & Radford, S. J. E. 2009, ApJ, 692, 1432

Grogin, N. A., Conselice, C. J., Chatzichristou, E., Alexander, D. M., Bauer, F. E., Hornschemeier, A. E., Jogee, S., Koekemoer, A. M., Laidler, V. G., Livio, M., Lucas, R. A., Paolillo, M., Ravindranath, S., Schreier, E. J., Simmons, B. D., & Urry, C. M. 2005, ApJ, 627, L97

Haubler, B., Barden, M., & McIntosh, D. H. 2008, AIPC, 1082, 137

Hickox, R. C., Jones, C., Forman, W. R., Murray, S. S., Kochanek, C. S., Eisenstein, D., Jannuzi, B. T., Dey, A., Brown, M. J. I., Stern, D., Eisenhardt, P. R., Gorjian, V., Brodwin, M., Narayan, R., Cool, R. J., Kenter, A., Caldwell, N., & Anderson,

M. E. 2009, eprint arXiv, 0901, 4121

Ho, L. C., Darling, J., & Greene, J. E. 2008, ApJSS, 177, 103

Ho, L. C., Filippenko, A. V., & Sargent, W. L. W. 1997a, ApJS, 112, 315

Ho, L. C., Filippenko, A. V., Sargent, W. L. W., & Peng, C. Y. 1997b, ApJS, 112, 391

Hopkins, P. F. & Hernquist, L. 2006, ApJSS, 166, 1

—. 2009, ApJ, 694, 599

Jones, D. H., Saunders, W., Colless, M., Read, M. A., Parker, Q. A., Watson, F. G., Campbell, L. A., Burkey, D., Mauch, T., Moore, L., Hartley, M., Cass, P., James, D., Russell, K., Fiegert, K., Dawe, J., Huchra, J., Jarrett, T., Lahav, O., Lucey, J., Mamon, G. A., Proust, D., Sadler, E. M., & ichi Wakamatsu, K. 2004, MNRAS, 355, 747

Kalberla, P. M. W., Burton, W. B., Hartmann, D., Arnal, E. M., Bajaja, E., Morras, R., & Pöppel, W. G. L. 2005, A&A, 440, 775

Kauffmann, G., Heckman, T. M., Tremonti, C., Brinchmann, J., Charlot, S., White, S. D. M., Ridgway, S. E., Brinkmann, J., Fukugita, M., Hall, P. B., Ivezić, Ž., Richards, G. T., & Schneider, D. P. 2003a, MNRAS, 346, 1055

Kauffmann, G., Heckman, T. M., White, S. D. M., Charlot, S., Tremonti, C., Brinchmann, J., Bruzual, G., Peng, E. W., Seibert, M., Bernardi, M., Blanton, M., Brinkmann, J., Castander, F., Csábai, I., Fukugita, M., Ivezic, Z., Munn, J. A., Nichol, R. C., Padmanabhan, N., Thakar, A. R., Weinberg, D. H., & York, D. 2003b, MNRAS, 341, 33

Kennicutt, R. C. 1998, Astrophysical Journal v.498, 498, 541

Kewley, L. J., Groves, B., Kauffmann, G., & Heckman, T. 2006, MNRAS, 372, 961

Kewley, L. J., Heisler, C. A., Dopita, M. A., & Lumsden, S. 2001, ApJSS, 132, 37

Kim, M., Ho, L. C., Peng, C. Y., Barth, A. J., Im, M., Martini, P., & Nelson, C. H.

2008, ApJ, 687, 767

Kirhakos, S. D. & Steiner, J. E. 1990, AJ, 99, 1435

Komossa, S., Burwitz, V., Hasinger, G., Predehl, P., Kaastra, J. S., & Ikebe, Y.
2003, ApJ, 582, L15

Koss, M., Mushotzky, R., Treister, E., Veilleux, S., Vasudevan, R., Miller, N.,
Sanders, D. B., Schawinski, K., & Trippe, M. 2011, ApJL, 735, L42

Koss, M., Mushotzky, R., Veilleux, S., & Winter, L. 2010, ApJL, 716, L125

Kriek, M., van Dokkum, P. G., Labbé, I., Franx, M., Illingworth, G. D., Marchesini,
D., & Quadri, R. F. 2009, ApJ, 700, 221

Levine, A. M., Lang, F. L., Lewin, W. H. G., Primini, F. A., Dobson, C. A., Doty,
J. P., Hoffman, J. A., Howe, S. K., Scheepmaker, A., Wheaton, W. A., Matteson,
J. L., Baity, W. A., Gruber, D. E., Knight, F. K., Nolan, P. L., Pelling, R. M.,
Rothschild, R. E., & Peterson, L. E. 1984, ApJSS, 54, 581

Li, C., Kauffmann, G., Wang, L., White, S. D. M., Heckman, T. M., & Jing, Y. P.
2006, MNRAS, 373, 457

Lintott, C. J., Schawinski, K., Slosar, A., Land, K., Bamford, S., Thomas, D., Rad-
dick, M. J., Nichol, R. C., Szalay, A., Andreescu, D., Murray, P., & Vandenberg,
J. 2008, MNRAS, 389, 1179

Liu, X., Greene, J. E., Shen, Y., & Strauss, M. A. 2010, ApJL, 715, L30

Lupton, R., Blanton, M. R., Fekete, G., Hogg, D. W., O'Mullane, W., Szalay, A.,
& Wherry, N. 2004, PASJ, 116, 133

Lynden-Bell, D. 1969, Nature, 223, 690

Magorrian, J., Tremaine, S., Richstone, D., Bender, R., Bower, G., Dressler, A.,
Faber, S. M., Gebhardt, K., Green, R., Grillmair, C., Kormendy, J., & Lauer, T.
1998, AJ, 115, 2285

Malizia, A., Stephen, J. B., Bassani, L., Bird, A. J., Panessa, F., & Ubertini, P.

2009, MNRAS, 399, 944

Maller, A. H., Berlind, A. A., Blanton, M. R., & Hogg, D. W. 2009, ApJ, 691, 394

Marshall, F. E., Boldt, E. A., Holt, S. S., Miller, R. B., Mushotzky, R. F., Rose, L. A., Rothschild, R. E., & Serlemitsos, P. J. 1980, ApJ, 235, 4

Masters, K. L., Nichol, R., Bamford, S., Mosleh, M., Lintott, C. J., Andreescu, D., Edmondson, E. M., Keel, W. C., Murray, P., Raddick, M. J., Schawinski, K., Slosar, A., Szalay, A. S., Thomas, D., & Vandenberg, J. 2010, MNRAS, 404, 792

Meléndez, M., Kraemer, S. B., Armentrout, B. K., Deo, R. P., Crenshaw, D. M., Schmitt, H. R., Mushotzky, R. F., Tueller, J., Markwardt, C. B., & Winter, L. 2008, ApJ, 682, 94

Metzger, A. E. 1964, Nature, 204, 766

Miller, C. J., Nichol, R. C., Gómez, P. L., Hopkins, A. M., & Bernardi, M. 2003, ApJ, 597, 142

Mink, D. J. 1996, Astronomical Data Analysis Software and Systems V, 101, 96

Mulchaey, J. S. & Regan, M. W. 1997, ApJL, 482, L135

Mullaney, J. R., Alexander, D. M., Goulding, A. D., & Hickox, R. C. 2011, MNRAS, 414, 1082

Mushotzky, R. 2004, Supermassive Black Holes in the Distant Universe. Edited by Amy J. Barger, 308, 53

Netzer, H., Kollatschny, W., & Fricke, K. J. 1987, A&A, 171, 41

Netzer, H., Lutz, D., Schweitzer, M., Contursi, A., Sturm, E., Tacconi, L. J., Veilleux, S., Kim, D.-C., Rupke, D., Baker, A. J., Dasyra, K., Mazzarella, J., & Lord, S. 2007, ApJ, 666, 806

Noguchi, K., Terashima, Y., Ishino, Y., Hashimoto, Y., Koss, M., Ueda, Y., & Awaki, H. 2010, ApJ, 711, 144

Osterbrock, D. E. 1978, In: Astronomical papers dedicated to Bengt Stromgren;

Proceedings of the Symposium, 299

Pascale, E., Ade, P. A. R., Bock, J. J., Chapin, E. L., Chung, J., Devlin, M. J., Dicker, S., Griffin, M., Gundersen, J. O., Halpern, M., Hargrave, P. C., Hughes, D. H., Klein, J., MacTavish, C. J., Marsden, G., Martin, P. G., Martin, T. G., Mauskopf, P., Netterfield, C. B., Olmi, L., Patanchon, G., Rex, M., Scott, D., Semisch, C., Thomas, N., Truch, M. D. P., Tucker, C., Tucker, G. S., Viero, M. P., & Wiebe, D. V. 2008, ApJ, 681, 400

Patton, D. R. & Atfield, J. E. 2008, ApJ, 685, 235

Peng, C. Y., Ho, L. C., Impey, C. D., & Rix, H.-W. 2002, AJ, 124, 266

Petrosian, A. R. 1982, (Astrofizika, 18, 548

Pierce, C. M., Lotz, J. M., Primack, J. R., Rosario, D. J. V., Griffith, R. L., Conselice, C. J., Faber, S. M., Koo, D. C., Coil, A. L., Salim, S., Koekemoer, A. M., Laird, E. S., Ivison, R. J., & Yan, R. 2010, MNRAS, 405, 718

Ranalli, P., Comastri, A., & Setti, G. 2003, A&A, 399, 39

Remillard, R. A., Bradt, H. V. D., Brissenden, R. J. V., Buckley, D. A. H., Roberts, W., Schwartz, D. A., Stroozas, B. A., & Tuohy, I. R. 1993, AJ, 105, 2079

Rex, M., Chapin, E., Devlin, M. J., Gundersen, J., Klein, J., Pascale, E., & Wiebe, D. 2006, Ground-based and Airborne Instrumentation for Astronomy. Edited by McLean, 6269, 109

Richards, G. T., Lacy, M., Storrie-Lombardi, L. J., Hall, P. B., Gallagher, S. C., Hines, D. C., Fan, X., Papovich, C., Berk, D. E. V., Trammell, G. B., Schneider, D. P., Vestergaard, M., York, D. G., Jester, S., Anderson, S. F., Budavári, T., & Szalay, A. S. 2006, ApJSS, 166, 470

Risaliti, G., Maiolino, R., & Salvati, M. 1999, ApJ, 522, 157

Sandage, A. R. 1971, Pontificiae Academiae Scientiarum Scripta Varia, 271

Sanders, D. B., Solomon, P. M., & Scoville, N. Z. 1984, ApJ, 276, 182

Satyapal, S., Vega, D., Dudik, R. P., Abel, N. P., & Heckman, T. 2008, ApJ, 677, 926

Sazonov, S. Y. & Revnivtsev, M. G. 2004, A&A, 423, 469

Schawinski, K., Lintott, C. J., Thomas, D., Kaviraj, S., Viti, S., Silk, J., Maraston, C., Sarzi, M., Yi, S. K., Joo, S.-J., Daddi, E., Bayet, E., Bell, T., & Zuntz, J. 2009a, ApJ, 690, 1672

Schawinski, K., Urry, C. M., Virani, S., Coppi, P., Bamford, S. P., Treister, E., Lintott, C. J., Sarzi, M., Keel, W. C., Kaviraj, S., Cardamone, C. N., Masters, K. L., Ross, N. P., Andreescu, D., Murray, P., Nichol, R. C., Raddick, M. J., Slosar, A., Szalay, A. S., Thomas, D., & Vandenberg, J. 2010, ApJ, 711, 284

Schawinski, K., Virani, S., Simmons, B., Urry, C. M., Treister, E., Kaviraj, S., & Kushkuley, B. 2009b, ApJL, 692, L19

Schlegel, D. J., Finkbeiner, D. P., & Davis, M. 1998, ApJ, 500, 525

Serber, W., Bahcall, N., Ménard, B., & Richards, G. 2006, ApJ, 643, 68

Seyfert, C. K. 1943, ApJ, 97, 28

Silverman, J. D., Mainieri, V., Lehmer, B. D., Alexander, D. M., Bauer, F. E., Bergeron, J., Brandt, W. N., Gilli, R., Hasinger, G., Schneider, D. P., Tozzi, P., Vignali, C., Koekemoer, A. M., Miyaji, T., Popesso, P., Rosati, P., & Szokoly, G. 2008, ApJ, 675, 1025

Simcoe, R., McLeod, K. K., Schachter, J., & Elvis, M. 1997, ApJ, 489, 615

Simmons, B. & Urry, C. 2008, ApJ, 683, 644

Smith, J. A., Tucker, D. L., Kent, S., Richmond, M. W., Fukugita, M., Ichikawa, T., ichi Ichikawa, S., Jorgensen, A. M., Uomoto, A., Gunn, J. E., Hamabe, M., Watanabe, M., Tolea, A., Henden, A., Annis, J., Pier, J. R., McKay, T. A., Brinkmann, J., Chen, B., Holtzman, J., Shimasaku, K., & York, D. G. 2002, AJ, 123, 2121

Smith, K. L., Shields, G. A., Bonning, E. W., McMullen, C. C., Rosario, D. J., & Salviander, S. 2010, ApJ, 716, 866

Solomon, P. M., Downes, D., & Radford, S. J. E. 1992, ApJ, 398, L29

Steffen, A. T., Strateva, I., Brandt, W. N., Alexander, D. M., Koekemoer, A. M., Lehmer, B. D., Schneider, D. P., & Vignali, C. 2006, AJ, 131, 2826

Stern, D., Eisenhardt, P., Gorjian, V., Kochanek, C. S., Caldwell, N., Eisenstein, D., Brodwin, M., Brown, M. J. I., Cool, R., Dey, A., Green, P., Jannuzi, B. T., Murray, S. S., Pahre, M. A., & Willner, S. P. 2005, ApJ, 631, 163

Tueller, J., Baumgartner, W. H., Markwardt, C. B., Skinner, G. K., Mushotzky, R. F., Ajello, M., Barthelmy, S., Beardmore, A., Brandt, W. N., Burrows, D., Chincarini, G., Campana, S., Cummings, J., Cusumano, G., Evans, P., Fenimore, E., Gehrels, N., Godet, O., Grupe, D., Holland, S., Kennea, J., Krimm, H. A., Koss, M., Moretti, A., Mukai, K., Osborne, J. P., Okajima, T., Pagani, C., Page, K., Palmer, D., Parsons, A., Schneider, D. P., Sakamoto, T., Sambruna, R., Sato, G., Stamatikos, M., Stroh, M., Ukwata, T., & Winter, L. 2010, ApJS, 186, 378

Tueller, J., Mushotzky, R. F., Barthelmy, S., Cannizzo, J. K., Gehrels, N., Markwardt, C. B., Skinner, G. K., & Winter, L. M. 2008, ApJ, 681, 113

Ueda, Y., Eguchi, S., Terashima, Y., Mushotzky, R., Tueller, J., Markwardt, C., Gehrels, N., Hashimoto, Y., & Potter, S. 2007, ApJ, 664, L79

Urry, C. M. & Padovani, P. 1995, PASP, 107, 803

Vasudevan, R. V., Fabian, A. C., Gandhi, P., Winter, L. M., & Mushotzky, R. F. 2010, MNRAS, 402, 1081

Vasudevan, R. V., Mushotzky, R. F., Winter, L. M., & Fabian, A. C. 2009, MNRAS, 399, 1553

Veilleux, S. 1988, AJ, 95, 1695

—. 1999, Astrophysics and Space Science, 266, 67

Veilleux, S., Kim, D.-C., Peng, C. Y., Ho, L. C., Tacconi, L. J., Dasyra, K. M., Genzel, R., Lutz, D., & Sanders, D. B. 2006, ApJ, 643, 707

Veilleux, S., Kim, D.-C., Rupke, D. S. N., Peng, C. Y., Tacconi, L. J., Genzel, R., Lutz, D., Sturm, E., Contursi, A., Schweitzer, M., Dasyra, K. M., Ho, L. C., Sanders, D. B., & Burkert, A. 2009a, ApJ, 701, 587

Veilleux, S. & Osterbrock, D. E. 1987, ApJSS, 63, 295

Veilleux, S., Rupke, D. S. N., Kim, D.-C., Genzel, R., Sturm, E., Lutz, D., Contursi, A., Schweitzer, M., Tacconi, L. J., Netzer, H., Sternberg, A., Mihos, J. C., Baker, A. J., Mazzarella, J. M., Lord, S., Sanders, D. B., Stockton, A., Joseph, R. D., & Barnes, J. E. 2009b, ApJS, 182, 628

Vestergaard, M. & Peterson, B. 2006, ApJ, 641, 689

Westoby, P. B., Mundell, C. G., & Baldry, I. K. 2007, MNRAS, 382, 1541

Winter, L., Mushotzky, R., Tueller, J., & Markwardt, C. 2008, ApJ, 674, 686

Winter, L. M., Lewis, K. T., Koss, M., Veilleux, S., Keeney, B., & Mushotzky, R. F. 2010, ApJ, 710, 503

Winter, L. M., Mushotzky, R. F., Reynolds, C. S., & Tueller, J. 2009, ApJ, 690, 1322

Yun, M. S., Reddy, N. A., & Condon, J. J. 2001, ApJ, 554, 803